

Aus dem Institut für Mineralogie und Petrographie
Universität Freiburg (Schweiz)

Sources and Characteristics of Fine and Ultrafine Particles in Ambient Air

INAUGURAL-DISSERTATION

zur Erlangung der Würde eines *Doctor rerum naturalium* der Mathematisch-
Naturwissenschaftlichen Fakultät der Universität Freiburg in der Schweiz

vorgelegt von

Ronny Lorenzo

aus

Kriens (LU)



Dissertation Nr. 1556
Empa Druckerei
2007

Von der Mathematisch-Naturwissenschaftlichen Fakultät der Universität Freiburg in der Schweiz
angenommen, auf Antrag von Prof. Dr. Bernard Grob  y, Prof. Dr. Heinz Burtscher, Dr. Reto Gier   und
Dr. Ralf K  gi.

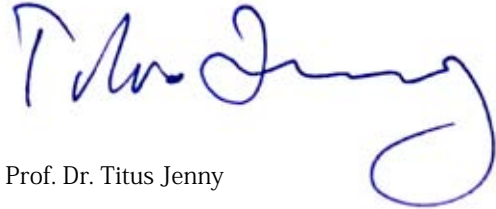
Freiburg, 20. April 2007

Der Leiter der Dissertation

A handwritten signature in blue ink, appearing to read 'B. Grob  y', enclosed in a light grey rectangular box.

Prof. Dr. Bernard Grob  y

Der Dekan

A handwritten signature in blue ink, appearing to read 'Titus Jenny', with a large, stylized flourish at the end.

Prof. Dr. Titus Jenny

Table of Contents

Abstract	7
Résumé	8
Zusammenfassung	9
Chapter 1	
Introduction	13
1.1 <i>Fine and ultrafine particles</i>	15
1.1.1 <i>Introduction</i>	15
1.1.2 <i>Health concerns</i>	16
1.2 <i>Instrumentation</i>	18
1.2.1 <i>Selected online measurement devices</i>	18
1.2.2 <i>Particle sampling</i>	20
1.3 <i>Thesis outline</i>	21
Chapter 2	
Particle Emissions of a Railway Line	25
2.1 <i>Introduction</i>	27
2.1.1 <i>PhD Thesis: Introductory project</i>	27
2.1.2 <i>Broader context</i>	27
2.2 <i>Particle emissions of a railway line determined by detailed single particle analysis</i>	28
2.3 <i>Technical details</i>	35
2.3.1 <i>Instrumentation</i>	35
2.3.2 <i>Railway study</i>	36
Chapter 3	
Thermophoretic Sampling Device	39
3.1 <i>Introduction</i>	41
3.1.1 <i>Thermophoresis</i>	41
3.1.2 <i>Advantages of thermophoretic sampling</i>	41
3.1.3 <i>Drawbacks and limitations</i>	42
3.1.4 <i>Calibrated sampling devices</i>	42
3.2 <i>A thermophoretic precipitator for the representative collection of atmospheric ultrafine particles for microscopic analysis</i>	43
3.3 <i>Technical details</i>	52
3.3.1 <i>Development</i>	52
3.3.2 <i>Experiments</i>	53
3.3.3 <i>Outlook</i>	54
Chapter 4	
Welding Fumes	57
4.1 <i>Introduction</i>	59
4.1.1 <i>Occupational health</i>	59
4.1.2 <i>Analytical methods</i>	59
4.2 <i>Extending the assessment procedures for exposure situations at working environments to ultrafine particles</i>	61
4.3 <i>Technical Details</i>	68
4.3.1 <i>Pilot study</i>	68
4.3.2 <i>Bag sampling device</i>	69
4.3.3 <i>Additional information</i>	70
Chapter 5	
Outlook	73

Appendix A

A.1 Abbreviations and definitions	77
A.2 Additional information on Chapter 2	80
A.2.1 Matlab sheets	80
A.2.2 Poster presented at the European Aerosol Conference 2005	85
A.3 Additional information on Chapter 3	86
A.3.1 Matlab sheet	86
A.3.2 LabView VI	88
A.3.3 Preliminary results of the CLACE 4 campaign (Jungfraujoch)	94
A.3.4 Poster presented at the AAAR Annual Meeting 2005	96
A.4 Additional information on Chapter 4	97
A.4.1 MathCAD sheet	97
A.4.2 Schematic of the bag sampler's frame	98
A.4.3 Schematic of the bag sampler's top cover	99
A.4.4 Schematic of the multi purpose inlet	100
A.4.5 Poster presented at the 10 th ETH Conference on combustion generated particles 2006	101
A.4.6 Poster presented at the International Aerosol Conference 2006	102

Appendix B

Acknowledgments	105
Curriculum Vitae	109
List of Publications	111

Abstract

The topic of this PhD thesis covers a variety of aspects of aerosol science. Accordingly, the projects contributing to the accomplishments of this work are manifold and connected only by the enveloping topic of ambient aerosols.

The goal of one of the studies was to identify and quantify particles emitted from railway traffic (chapter 2). For that purpose PM₁₀ samples were collected near a busy railway line using a wind direction and speed controlled sampling equipment consisting of five devices. Measurements taken perpendicular to the railway lines at 10 m, 36 m and 120 m distance enable an identification and separation of particles caused by the railway traffic from background particles. Morphology and chemistry of more than 11'000 individual particles were analysed by computer controlled scanning electron microscopy (CCSEM).

Based on chemical composition five particle classes are defined and assigned to their sources. The mass of the individual particles is determined by multiplying their volumes, calculated based on their morphology with a density assigned specifically to each particle class. The density of the particle classes is derived from their chemical composition. To estimate the PM₁₀ contributions of the railway lines, the mass of PM₁₀ at 120 m (background, not influenced by the railway lines) is subtracted from the mass of PM₁₀ at 10 m.

The emissions of the railway lines are dominated by 'iron' particles, which contribute 2.9 $\mu\text{g m}^{-3}$ or 67% of the railway related PM₁₀. In addition, 'aluminium' and 'calcium' particles contribute also to the railway related PM₁₀ (0.4 $\mu\text{g m}^{-3}$ or 23% for the 'aluminium' and 0.4 $\mu\text{g m}^{-3}$ for the 'calcium' particles). These particles are associated with the re-suspension of the gravel bed and re-suspension of

Long-term gravimetric results of the coarse fraction of iron to the mass of railway related PM₁₀ performed earlier at the same site are in good agreement with the data gained from this study.

In a project to explore the potential of thermophoretic sampling devices to derive quantitative particle size distributions and number concentrations of aerosols based on microscopic single particle analysis, the focus moved from PM₁₀ to PM_{0.5} (chapter 3). For that purpose a plate-to-plate thermophoretic precipitator to collect ultrafine atmospheric particles for TEM (transmission electron

microscopy) analysis has been calibrated and characterised. The representativeness of the samples has been verified in a series of experiments. Results show that for particles with diameter of 15 nm to 300 nm the precipitator works independent of size, shape and composition of the particles and, therefore, its samples accurately represent the original aerosol.

A numerical model of the thermophoretic deposition properties has been developed and tailored to the specifications of the precipitator. The model has been used to derive the particle number density and size distribution of several calibration aerosols using the TEM analysis of the samples taken with the thermophoretic precipitator as input parameters. The results agree very well with the online measurements of the calibration aerosols. This project demonstrates that a thermophoretic sampling device can be used to derive quantitative particle size distributions and number concentrations of ultrafine particles based on microscopic single particle analysis.

In a third study the emphasis was set on occupational health and working environments. A combination of online instruments and sampling devices for the subsequent offline analysis of fine (<600 nm) and ultrafine (<100 nm) aerosols for a complete assessment of a working environment is proposed and tested at a welding shop (chapter 4). Online measurements show highly variable particle production rates during welding and a considerable increase in background number concentrations of fine particles the day. The comparison of two work places within the same facility reveals comparable particle number concentrations but significantly differing size distributions. With single particle analysis on a TEM three different types of primary particles are defined. While they can be distinguished by their morphology, energy dispersive analysis and crystallographic methods (selected area electron diffraction, SAED) indicate that the different types of primary particles all consist of the same base material.

The measurement strategy suggested in this study allows a complete evaluation of the exposure conditions met by the employees. The data on number concentrations, particle characteristics and surface composition should be used as guidelines for toxicological studies to gain further insight on the consequences of relevant exposure doses for occupational health.

Table of Contents

Résumé

Le sujet de cette thèse de doctorat couvre de nombreux aspects de la science des aérosols. Ainsi les différentes études de ce travail abordent des domaines variés dont le point commun est le thème global des aérosols de l'environnement.

Une de ces études a été consacrée à l'identification et la quantification des particules émises par le trafic ferroviaire (chapitre 2). Pour cela, des échantillons de PM10 ont été récoltés à proximité d'une ligne de chemin de fer à fort trafic au moyen d'un équipement d'échantillonnage avec enregistrement de la direction et de la vitesse du vent comportant au total cinq unités de prélèvement. Les prélèvements effectués à des distances 10 m, 36 m et 120 m perpendiculairement à la voie de chemin de fer ont permis une identification et une distinction des particules émises par le trafic ferroviaire de celles provenant de la pollution de fond. La morphologie et la composition chimique de plus de 11'000 particules individuelles ont été analysées par microscopie électronique à balayage contrôlée par ordinateur (Computer Controlled Scanning Electron Microscopy CCSEM)

Sur la base de leur composition chimique, les particules ont été distribuées en cinq classes et attribuées à leurs sources. La masse des particules individuelles a été déterminée en multipliant leur volume, calculé sur la base de leur morphologie, par une densité attribuée spécifiquement à chaque classe de particules. La densité des différentes classes de particules a été dérivée de leur composition chimique. Pour estimer la contribution du trafic ferroviaire aux émissions de PM10, la masse des PM10 à 120 m des voies (pollution de fond non influencée par les voies de chemin de fer) a été soustraite de la masse des PM10 à 10 m des voies.

Les émissions de particules des chemins de fer sont dominées par les particules de 'fer' qui contribuent pour $2.9 \mu\text{g m}^{-3}$ ou 67% aux PM10 émises par ceux-ci. Par ailleurs, les particules d'aluminium et de calcium contribuent elles aussi aux PM10 émises par les chemins de fer ($1.0 \mu\text{g m}^{-3}$ ou 23% pour les particules d' 'aluminium' et $0.4 \mu\text{g m}^{-3}$ ou 10% pour celles de 'calcium'). Ces particules sont attribuables à l'abrasion du ballast et à la remise en suspension de poussières minérales

Les résultats de mesures gravimétriques à long terme sur la contribution du fer à la masse totale des particules émises par les chemins de fer d'une étude précédente sur le même site sont en bonne concordance avec les données recueillies dans cette étude.

Dans un projet destiné à étudier l'adéquation des dispositifs d'échantillonnage thermophorétiques à la détermination des distributions quantitatives de la taille des particules et de leurs concentrations numériques basées sur l'analyse microscopique de particules isolées, l'intérêt s'est reportés des particules PM10 aux particules PM0.5

(chapitre 3). Pour cela, un précipitateur thermophorétique à plaques parallèles a été étalonné et caractérisé pour la collecte des particules atmosphériques ultrafines. La représentativité des échantillons a été vérifiée dans une série d'expériences. Les résultats montrent que pour les particules d'un diamètre de 15 nm à 300 nm le précipitateur fonctionne indépendamment de la taille, de la forme et de la composition des particules et qu'ainsi ses échantillons sont parfaitement représentatifs de l'aérosol original

Un modèle numérique de la déposition thermophorétique a été développé et adapté aux spécifications du précipitateur. Ce modèle a été utilisé pour déterminer la densité numérique et la distribution de la taille des particules de plusieurs aérosols d'étalonnage en utilisant l'analyse au microscope électronique à transmission (TEM) des échantillons prélevés par échantillonnage thermophorétique comme paramètres d'entrée. Les résultats concordent fort bien avec les mesures en ligne des aérosols d'étalonnage. Ce projet démontre que le dispositif d'échantillonnage thermophorétique peut être utilisé pour déterminer la distribution quantitative de la taille et la concentration numérique de particules ultrafines basée sur l'analyse microscopique de particules isolées.

L'accent de la troisième étude porte sur l'hygiène et l'environnement du travail. Une combinaison d'instruments de mesure en ligne et de dispositifs d'échantillonnage pour l'analyse subséquente hors ligne d'aérosols fins (<600 nm) et ultrafins (<100 nm) pour l'évaluation complète d'un environnement de travail est proposée et a été testée dans un atelier de soudage (chapitre 4). Les mesures en ligne mettent en évidence une variation importante des taux de production de particules au cours du soudage et une augmentation considérable des concentrations numériques de fond des particules fines au cours de la journée. La comparaison de deux postes de travail situés dans le même atelier révèle des concentrations numériques comparables mais des différences significatives dans la distribution de la taille des particules. L'analyse de particules isolées sur le microscope électronique à transmission (TEM) permet de définir trois types de particules différents. Alors qu'elles diffèrent par leur morphologie, l'analyse aux rayons X dispersive en énergie et par des méthodes cristallographiques montre que les particules de ces deux types sont toutes formées du même matériau de base.

La stratégie de mesure proposée dans cette étude permet une évaluation complète des conditions d'exposition auxquelles sont soumis les employés. Les données sur les concentrations numériques, les caractéristiques des particules et la composition de leur surface devraient être utilisées dans des études toxicologiques pour arriver à une meilleure compréhension des conséquences sur le plan de l'hygiène du travail des doses d'exposition importantes.

Zusammenfassung

Das Thema dieser Doktorarbeit umfasst diverse Aspekte der Aerosol Wissenschaften. Entsprechend weitgestreut sind die Erkenntnisse, die aus den Projekten gewonnen werden konnten, die im Verlaufe der letzten drei Jahre unter dem Mantel der Aerosole in der Aussenluft durchgeführt wurden.

Das Ziel einer der Studien war die Identifizierung und Quantifizierung der Partikel die durch den Eisenbahnverkehr erzeugt werden (Kapitel 2). Zu diesem Zweck wurden PM10 Proben entlang einer stark frequentierten Eisenbahnlinie gesammelt. Die fünf dazu verwendeten Sammler wurden simultan mittels einer Windsteuerung kontrolliert. Messstandorte senkrecht zum Verlauf der Eisenbahnlinie in Abständen von 10 m, 36 m und 120 m zu den Geleisen, ermöglichten eine Differenzierung zwischen partikulärer Hintergrundbelastung und durch die Eisenbahn erzeugten Partikeln. Morphologie und chemische Zusammensetzung von 11'000 individuellen Partikeln wurde mittels Computer gesteuerter Raster-Elektronenmikroskopie analysiert.

Basierend auf chemischer Zusammensetzung werden fünf Partikelklassen definiert und Quellen zugeordnet. Die Masse der individuellen Partikel wird durch Multiplikation ihres Volumens - berechnet auf Basis ihrer Morphologie - mit der klassenspezifischen Dichte ermittelt. Die Dichte der Klassen ist von der ihnen zugrundeliegenden chemischen Definition abgeleitet. Um den Beitrag der Eisenbahnlinien an die lokale PM10 Belastung abzuschätzen, wird die für den 120 m Standort ermittelte Masse von Wert des 10 m Standortes abgezogen. Dies geschieht unter der Annahme, dass der 120 m Standort nicht mehr von der Eisenbahn beeinflusst wird und somit einer Hintergrundstation entspricht.

Die Emissionen der Eisenbahnlinien werden durch Eisenpartikel dominiert welche einen Beitrag von $2.9 \mu\text{g m}^{-3}$ an die eisenbahnbezogene PM10 Masse leisten, was 67% entspricht. Zusätzliche Beiträge leisten Partikel der 'Aluminium' ($1.0 \mu\text{g m}^{-3}$ oder 23%) und der 'Calcium' Klasse ($0.4 \mu\text{g m}^{-3}$ oder 10%). Beide Partikelklassen werden der Abnützung des Kiesbettes und der Resuspendierung von mineralischem Feinstaub zugeschrieben.

Gravimetrisch ermittelte Resultate des Eisengehaltes der eisenbahnbezogenen PM10 Belastung, die im Rahmen einer vorgängig an den selben Messstandorten durchgeführten langzeit Studie erarbeitet wurden, stehen in guter Übereinstimmung mit den Werten der hier vorgestellten Studie.

In einem Projekt zur Erforschung des Potentials von thermophoretischen Sammelgeräten zur quantitativen Bestimmung von Partikel Grössenverteilungen und Anzahlkonzentrationen, verschob sich der Fokus der Arbeiten von PM10 zu PM0.5 (Kapitel 3). Zu diesem Zweck wurde ein thermophoretischer Sammler mit zwei parallelen Platten

zum Sammeln von atmosphärischen Partikeln für die Analyse mittels Transmissions-Elektronenmikroskopie (TEM) kalibriert und charakterisiert. Die Repräsentativität der Proben wurde anhand einer Reihe von Experimenten verifiziert. Die Resultate zeigen, dass der Sammler für Partikel mit Durchmesser zwischen 15 nm und 300 nm unabhängig von Partikelgrösse, -form und -zusammensetzung arbeitet. Dies bedeutet, dass die Proben eine getreue Wiedergabe des originalen Aerosols darstellen.

Es wurde ein numerisches Modell zur Beschreibung der Thermophorese entwickelt und auf die Spezifikationen des Sammlers angepasst. Das Modell wurde dazu verwendet, um aus den Resultaten der TEM Analyse von mit dem Sammler gezogenen Proben die Partikel Anzahlkonzentrationen und Grössenverteilungen der verwendeten kalibrations Aerosole zu berechnen. Die so ermittelten Resultate stimmen sehr gut mit den gleichzeitig durchgeführten online Messungen der kalibrations Aerosole überein. Dieses Projekt demonstriert somit, dass thermophoretische Sammler dazu verwendet werden können um quantitative Grössenverteilungen und Anzahlkonzentrationen von ultrafeinen Aerosolen mittels mikroskopischer Einzelpartikelanalyse zu ermitteln.

In einer dritten Studie wurde das Augenmerk auf arbeitsmedizinische Aspekte und Arbeitsplätze gerichtet. Es wurde eine Kombination von online Geräten und Probensammlern für feine (<600 nm) und ultrafeine (<100 nm) Aerosole für eine vollständige Einschätzung einer Arbeitsumgebung vorgeschlagen und bei Schweissarbeiten getestet (Kapitel 4). Die online Messungen zeigen, dass die Produktionsraten für Partikel während des Schweissens stark variieren können. Ausserdem ist ein signifikanter Anstieg der Konzentration von feinen Partikeln im Verlaufe eines Tages festzustellen. Messungen an zwei verschiedenen Arbeitsplätzen förderten vergleichbare Anzahlkonzentrationen bei deutlich unterschiedlichen Grössenverteilungen zutage. Durch Einzelpartikelanalysen mit einem TEM konnten drei unterschiedliche Typen von Primärpartikeln nachgewiesen werden. Obwohl die Typen aufgrund ihrer Morphologie unterschieden werden können, deuten energiedispersive Röntgenanalysen und kristallographische Untersuchungsmethoden darauf hin, dass alle aus dem selben Grundmaterial bestehen.

Die in dieser Studie vorgeschlagene Messstrategie ermöglicht eine vollständige Evaluation der Exposition der Arbeiter zu feinen und ultrafeinen Aerosolen. Die hierin ermittelten Anzahlkonzentrationen, Partikelcharakteristika und Oberflächenbeschaffenheiten sollten in künftigen toxikologischen Studien als Rahmenbedingungen genutzt werden. Denn nur so können zusätzliche Erkenntnisse bezüglich der arbeitsmedizinischen Konsequenzen von relevanten Expositionsdosen gewonnen werden.

«To boldly go where no man has gone before.»

Star Trek

Introduction

- Literature
- Instrumentation
- Thesis Outline

«Logic is the beginning of wisdom, not the end.»

Spock, Star Trek VI

1 Introduction

1.1 Fine and ultrafine particles

1.1.1 Introduction

Aerosols have been a topic of scientific investigations for decades and a wealth of literature is available. In the last couple of years several exceptional reviews have been published and these introductory pages are loosely based on a selection of them (e.g., Baron and Willeke 2001; Spurny 1999). The first issue that needs clarification is the nomenclature. There are almost as many definitions for particle types and size ranges as there are scientific disciplines involved in aerosol research.

An assembly of liquid or solid (or mixed) particles suspended in a gaseous medium long enough to be measured or observed, is referred to as aerosol. In this definition, no distinction between engineered or naturally produced particles is being made because both types are governed by the same physical laws as long as they are in a comparable size range (exemplary sources are listed in Table 1.1).

Compared to an average air molecule with a diameter of 0.37 nm, even the smallest aerosol particles are large. Although the boundary between airborne molecules and very small aerosol particles is blurry, the latter are generally 1 nm or larger in diameter. Fume particles of 1 nm in size for example, can be seen only immediately after condensation from the vapour stage. Shortly afterwards they have usually grown or coagulated into larger entities.

The upper size limit for particles, which stay suspended long enough to be measured and observed, is generally considered to be 100 μm (diameter). In contrast to the small particles, dust particles result from size reduction of larger materials. This process is fuelled by mechanical forces, natural or induced by human action, and is limited to a size range where the externally applied forces are greater than the internal cohesion forces. Thus, particles smaller than ~ 500 nm are relatively rare in dust distributions.

There is a variety of different nomenclatures for distinct particle size ranges. Figure 1.1 gives a definition based on an idealised size distribution of traffic-related particulate matter (PM) and its production processes. Four size classes are distinguished.

Frequently the two smallest size ranges, the nucleation mode and Aitken mode, are summarised as “ultrafine particles” (UFP) or PM_{0.1} (particulate matter < 0.1 μm). In analogy to the definition of UFP, particulate matter smaller than 1 μm (PM_{1.0}) is also known as “fine particles” (FP).

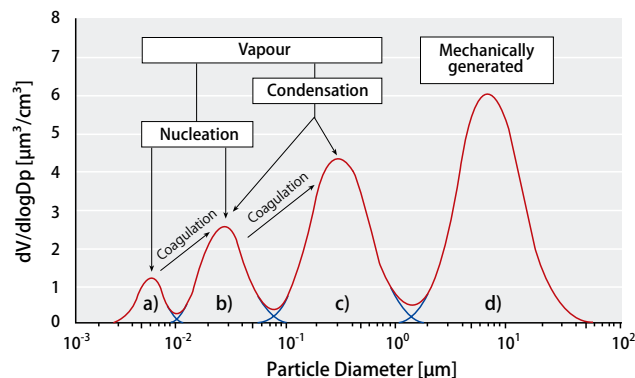


Fig. 1.1: Idealised size distribution of traffic-related particulate matter (U.S. EPA 2004). a: Nucleation mode; b: Aitken mode; c: Accumulation mode; d: Coarse mode. Nucleation and Aitken mode particles are defined as ultrafine particles (UFP).

A more technical distinction of particle size ranges is based on the Knudsen number Kn (eq. 1; Baron and Willeke 2001), which relates the molecular mean free path l_m to the physical dimensions of the particle, usually the particle radius r . The molecular mean free path is the average distance a molecule travels before colliding with another molecule. In air and standard conditions (1'013 mbar, 20°C) this distance is 66.4 nm. Particles, which are much smaller than the mean free path ($Kn \gg 1$), travel freely through the fluid. Accordingly, this particle size range is called “free molecular regime” and particle motions are determined by gas kinetics. The motion of particles with $Kn \ll 1$ is mainly influenced by the bombardment from all directions by a great number of molecules. They travel, therefore, along the flow lines, which are described by continuum flow considerations. This size range is, thus, called “continuum flow regime”.

$$Kn = \frac{l_m}{r} = \frac{2l_m}{d_p} \quad (1)$$

The intermediate range, $Kn \approx 0.25$ to 20 (~ 6.6 nm to ~ 530 nm), is usually referred to as the “transition regime” or “slip flow regime”. The motion of particles in this size regime is still determined by the continuum gas flow, but corrections for the slip at the particle - gas interface have to be applied. This slip correction factor, C_c , also referred to as the “Cunningham slip correction factor”, is introduced

Table 1.1
Sources for ultrafine particles (<100nm) (Oberdorster *et al.* 2005)

Natural	Anthropogenic	
	Unintentional	Intentional
Gas-to-particle conversion	Internal combustion engines	Controlled size and shape, designed for functionality
Forest fires	Power plants	Metals, semiconductors, metal oxides, carbon, polymers
Volcanoes (hot lava)	Incinerators	Nanospheres, -wires, -needles, -tubes, -shells, -rings, -platelets
Viruses	Jet engines	Untreated, coated (nanotechnology applied to many products: cosmetics, medical, fabrics, electronics, optics, displays, etc.)
Biogenic magnetite: magnetotactic bacteria protactists, mollusks, anthropods, fish, birds, human brain, meteorite (?)	Metal fumes (e.g. smelting, welding)	
Ferritin (12.5 nm)	Polymer fumes	
Microparticles (<100 nm; activated cells)	Other fumes	
	Heated surfaces	
	Frying, broiling, grilling	
	Electric motors	

into the equations. For solid particles equation 2 (Hinds 1999) may be used where P is the absolute pressure in kPa and d_p the particle diameter in μm .

$$C_c = 1 + \frac{1}{Pd_p} \left(15.60 + 7.00 e^{-0.059Pd_p} \right) \quad (2)$$

In the continuum regime C_c is one and becomes greater than one for decreasing particle diameter. For instance, for particles with a diameter of $10 \mu\text{m}$ $C_c = 1.02$, for $1 \mu\text{m}$ particles C_c is still 1.16 and for $0.1 \mu\text{m}$ particles $C_c = 2.9$.

The transition character of the slip flow regime is best illustrated on the particle settling speeds due to diffusion. While diffusion is no issue for particles in the continuum regime, it is a dominating factor for the behaviour of molecules. To determine the behaviour of the particles in the transition regime, C_c is added to the equation for the diffusion coefficient resulting in an exponential increase of the particle velocity due to diffusion with decreasing particle diameter (Fig. 1.2, blue curve). Accordingly, particle losses due to diffusion are a major issue for collecting UFPs.

For particles of the coarse mode, diffusion is of minor importance. The red curve in Figure 1.2 indicates the particle settling speed due to gravitation. While the plot ends at $1 \mu\text{m}$, it is still obvious that the influence of gravitation, and thus, of the particle inertia as well, is steadily increasing towards larger diameters.

1.1.2 Health concerns

The potential of particulate matter to evoke adverse health effects has long been known. The diverse types of particles and the wide range of sizes (spanning five orders of magnitude) found in natural and anthropogenic aerosols, however, make it difficult to identify the mechanisms by which particles influence biological systems. The following brief overview on health concerns is based on recent comprehensive reviews summarising presently known effects and mechanisms (e.g., Maynard and Kuempel 2005; Oberdorster *et al.* 2005; Wiesner *et al.* 2006).

General considerations

With decreasing particle size the ratio of surface to total atoms or molecules increases exponentially (Fig. 1.3). This delivers special properties to the UFPs such as making them desirable as catalysts for chemical reactions. Increased surface reactivity predicts that UFPs have a greater biological activity per given mass compared with larger particles. This can either be positive and desirable (e.g., antioxidant activity, carrier capacity for therapeutic

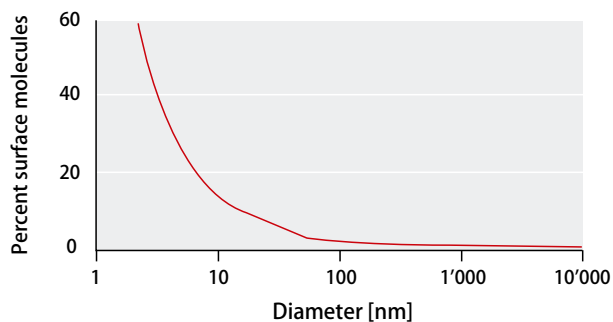


Fig. 1.3: Surface molecules as a function of particle size. The comparably large surface makes UFPs desirable as catalysts for chemical reactions. (Oberdorster *et al.* 2005)

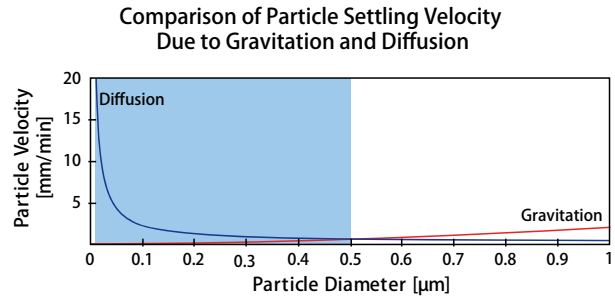


Fig. 1.2: Comparison of particle settling velocities due to gravitation and diffusion. Particle motion in the slip flow regime (blue area) is dominated by diffusion. For UFP losses due to diffusion are a major concern in instrument development.

tics, penetration of cellular barriers for drug delivery) or negative and undesirable (e.g., toxicity, induction of oxidative stress or of cellular dysfunction), or a mix of both (Oberdorster 2005). The positive aspects triggered many efforts aiming at exploiting the desirable properties of (specifically engineered) nano-sized particles for improving human health. However, this is in stark contrast to the limited attempts to evaluate potential undesirable effects of the same particles when administered intentionally for medicinal purposes, or after unintentional exposure during manufacture or processing.

Since the characteristic biokinetic behaviour of engineered nano-sized particles are a mixed blessing, evaluating the safety of these particles should be of highest priority. Given that production and worldwide distribution of manufactured UFPs for industrial applications is gaining speed, human exposure - directly or through release into the environment (air, water, soil) - is getting increasingly probable.

Toxicology of airborne UFP

Several epidemiological studies have found associations of ambient UFPs with adverse respiratory and cardiovascular effects resulting in morbidity and mortality in susceptible parts of the population (Pekkanen *et al.* 1997; Penttinen *et al.* 2001; Peters *et al.* 1997a, 1997b; von Klot *et al.* 2002; Wichmann *et al.* 2002).

In addition, after controlled exposure to carbonaceous UFPs effects on the cardiovascular system, including coagulation blood markers and pulmonary diffusion capacity as well as an increase in systemic inflammations, were observed (Anderson *et al.* 1990; Brown *et al.* 2002; Chalupa *et al.* 2004; Heinrich 2004; Henneberger *et al.* 2005; Jaques and Kim 2000; Wichmann *et al.* 2000).

In vitro studies have shown that UFP induced oxidative stress and the presence of transition metals as well as certain organic compounds on combustion generated UFPs are responsible for changes of gene expression and of cell signalling pathways. (Brown *et al.* 2000, 2001; Donaldson *et al.* 2002; Donaldson and Stone 2003; Li *et al.* 2003).

Laboratory rodent studies (*in vivo*) fill in where exposure experiments on humans would be unethical or when *in vitro* studies are not appropriate. While the results of the numerous *in vivo* studies published so far can differ quite significantly, most agree on three findings. As mentioned earlier, many of the characteristic properties of UFPs are due to the favourable surface to mass ratio. Several studies with fine and ultrafine (e.g., TiO_2) particles suggest that for particles of different sizes but of the same chemistry, particle surface area is a better dosimetric than particle mass or number (Brown *et al.* 2001; Donaldson *et al.* 1998, 2002;

Driscoll 1996; Oberdorster and Yu 1990; Oberdorster *et al.* 1992; Oberdorster 2000; Tran *et al.* 1998, 2000). Further, experiments with PTFE (Teflon) fumes showed that particle chemistry, and specifically surface chemistry, plays a decisive role in the pulmonary toxicity of UFPs (Coleman *et al.* 1968; Griffith *et al.* 1973; Oberdorster *et al.* 1995). Analysis of these fumes revealed the nano-sized nature of the particulates (mode at 18 nm) generated by heating PTFE to -480°C . And finally, morphology may also play a role in the toxicity of UFPs. It's well established that it is the fibrous habit of natural (e.g., asbestos) and man-made (e.g., biopersistent vitreous) fibres that are responsible for the increased risks of pulmonary fibrosis and cancer after prolonged exposures (Greim *et al.* 2001; International Agency for Research on Cancer (IARC) 2002). The "three Ds" were identified as the critical parameters: dose, dimension, and durability of the fibres.

However, as Paracelsus used to say almost 500 years ago: «All things are poison and nothing without poison; only the dose decides that a thing is not a poison.» (German: «All Ding' sind Gift und nichts ohn' Gift; allein die Dosis macht, dass ein Ding kein Gift ist.») Up to now, most studies applied very high doses raising the question whether the effects observed would be identical if low more realistic doses would have been administered. A careful evaluation of exposure-dose-response relationships is, therefore, critical to the toxicological assessment of UFPs, including the choice of an appropriate dosimetric - mass, number, or surface of the particles (Maynard and Kuempel 2005; Oberdorster *et al.* 2005; Vincent 2005; Wiesner *et al.* 2006). A critical gap that urgently needs to be filled is the complete lack of data on human exposure levels of UFPs.

Portals of entry

Most research on health effects of UFPs is done with the focus on the respiratory system as portal of entry for the particles. The respiratory system, however, is not the only uptake route for nano-sized particles. Skin and gastrointestinal (GI) tract need to be considered as portals of entry as well.

Figure 1.4 shows the predicted fractional deposition of inhaled particles in the human respiratory tract during nose breathing (at rest). Particles in the continuum regime are preferably deposited in the nose due to inertial impaction. Particles of the free molecular regime, e.g., on the

opposite side of the size distribution, have similar fate. As a consequence of their high mobility (see also Fig. 1.2) they are deposited primarily in the nose or the tracheobronchial region by diffusion. Particles of the transition regime, e.g. from the intermediate range of the size distribution, have the highest deposition efficiency in the Alveolar region with a maximum for 20 nm particles (50%). The Alveolar region has a high density of blood vessels, which seem to be ideal entry portals for UFPs into the blood circulation. In contrast to larger particles, UFPs appear to translocate readily to extrapulmonary sites and reach other target organs (Berry *et al.* 1977; Heckel *et al.* 2004; Mehta *et al.* 2004; Rejman *et al.* 2004). Once they have translocated to the blood circulation, they can be distributed throughout the body. The liver is the major final destination, followed by the spleen, but deposition in the heart, brain and kidney are reported as well.

A number of studies point out that the olfactory nerve pathway should also be considered as a portal of entry to the central nervous system (CNS) for humans exposed to airborne UFPs (Feikert *et al.* 2004; Hunter and Dey 1998; Hunter and Udem 1999; Oberdorster *et al.* 2004). Given that 40-90% of the particles of the free molecular regime are deposited in this area of the respiratory system (see Fig. 1.4) more information on the transfer mechanisms and particle selectivity are needed.

Concerning skin as a portal of entry for particulate matter, there are indications that unscarred and flat skin is virtually impermeable for particles. However, broken skin represents a readily available portal of entry even for larger (0.5 - 7 μm) particles (Blundell *et al.* 1989; Corachan *et al.* 1988). Tinkle *et al.* (2003) hypothesised that flexed skin - as in wrist movements - would make the epidermis permeable for UFPs. In a proof-of-concept experiment they showed that flexing the skin resulted in penetration of even 1 μm fluorescent beads to the dermis. The same experiment on unflexed, flat skin showed no penetration.

And finally, only few studies have investigated the uptake and disposition of nano-sized particles by the gastrointestinal (GI) tract, and most have shown that UFPs pass through the GI tract and are eliminated rapidly (Kreyling *et al.* 2002; Semmler *et al.* 2004; Yamago *et al.* 1995).

Risk assessment

Many regulatory agencies do not consider a nanotechnology manufactured substance different from the conventional substance. Hence, the production and use of nanotechnology products are currently not specifically regulated. As a consequence, exposure limits - if existing - are mass-based and fall short of taking the special characteristics of the UFPs into account. While the underlying mechanisms of toxicity are still relatively poorly understood, it is quite certain that size and surface area play a key role. An exception is asbestos for which strict regulations exist.

Based on the scarce data on exposure levels during production and handling of UFPs in related industries, approaches to safe nanotechnology are being developed (NIOSH 2006). However, methods for characterising and quantifying nanoparticles in occupational environments, including determination of relevant exposure levels, remain largely undeveloped. Studies as described in chapter 4 or as performed by Brouwer *et al.* (2004) remain the exception.

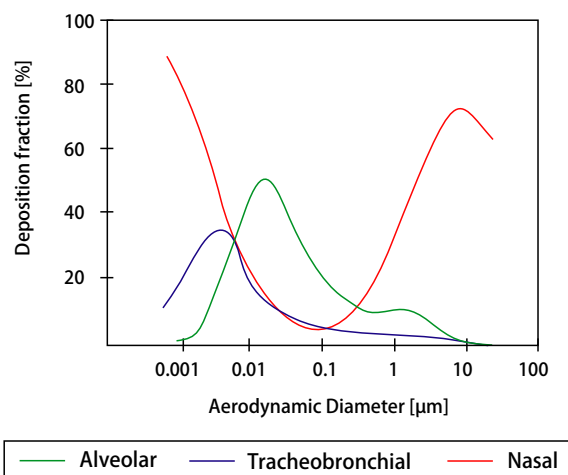


Fig. 1.4: Predicted fractional deposition of inhaled particles in the respiratory tract during nasal breathing. (Oberdorster *et al.* 2004)

1.2 Instrumentation

In 1847 H. Becquerel hypothesised that cloud formation might have something to do with fine particles suspended in air - now called "condensation nuclei". Roughly 30 years later their existence was confirmed in experiments by Coulier (1875). Coulier built a device to expand air adiabatically in controlled conditions. He repeated the experiment with filtered and unfiltered air and observed that condensation occurred more readily with unfiltered air. In principle, Coulier's apparatus was the first condensation nuclei detector.

Since Coulier's days, a variety of different instruments to collect, count, measure and analyse particles has been developed. Nowadays virtually for every aspect of aerosol science at least one highly specialised instrument is in existence. A comprehensive summary of current aerosol measurement and analysis principles is given in the standard references books edited by Baron and Willeke (2001) and Spurny (1999).

To set the stage for the chapters on the different projects of this thesis, the instruments used during the measurement campaigns and experiments are briefly described in the remainder of this section (1.2.1 and 1.2.2).

1.2.1 Selected online measurement devices

Electrical diffusion battery, EDB

The EDB (Fierz *et al.* 2002) is a device to measure size distributions with a high time resolution (<1 s) at the cost of low size resolution (Fig. 1.5). After entering the instrument particles are charged in a unipolar diffusion charger by a positive corona discharge. To keep ions from entering the diffusion battery, an ion filter is located between the charger and the diffusion stages of the instrument.

Four diffusion stages, each consisting of several fine wire-mesh screens, are mounted electrically insulated from each other, and equipped with sensitive current amplifiers to measure the deposition of the charged particles (E1-4). The number of screens in each stage is chosen such that the four stages have 50% penetration at 10, 20, 40 and 80 nm diameter, respectively. The final stage (E5) is equipped with a backup filter to detect the remaining particles.

The EDB is capable of deriving fairly accurate size distributions for log-normal distributions between approximately 10 nm and 300 nm. Through clever data inversion algorithms, also bi-modal size distributions may be reproduced, though the precision is limited. Particle number concentrations, however, are accurately measured for aerosol concentrations between 10^4 - 10^6 particles cm^{-3} at the inlet.

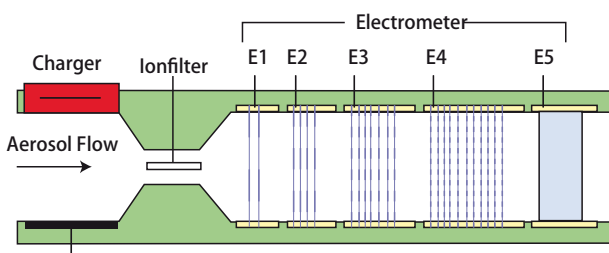


Fig. 1.5: Schematic of an EDB (Fierz *et al.* 2002). Particles are charged in a unipolar diffusion charger. After passing an ion filter, the particles pass through four diffusion stages (E1-4) with increasing cut points (10, 20, 40 and 80 nm). Remaining particles are collected on a backup filter.

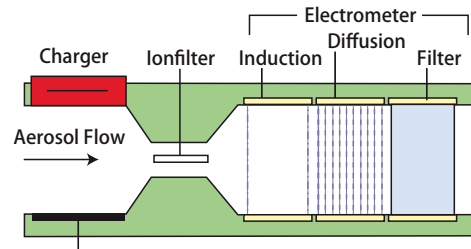


Fig. 1.6: Schematic of a DiSC (Fierz and Burtscher 2005). In contrast to the EDB (Fig. 1.5), the DiSC has only one diffusion stage. To correct for errors due to fast changes in particle number concentrations, the charged aerosol passes an induction stage prior to the diffusion stage.

The advantages of the EDB are its small size, robust build and easy handling compared to other devices capable of fast determination of particle size distribution. On the other hand, its resolution and precision are limited.

Diffusion size classifier, DiSC

The DiSC is basically a small and highly mobile EDB with a time resolution as high as 1 s (Fierz and Burtscher 2005). The Diffusion charger and ion filter are comparable to the one in the EDB (Fig. 1.5). Instead of the four diffusion stages the DiSC has only one, preceded by an induction stage, which is simply a Faraday cage. During a fast concentration change, a current is induced in both the induction stage and the following diffusion stage. The signal from the induction stage is then used to correct the signal from the diffusion stage. The third stage is - similar to the EDB - a filter stage, where all remaining particles are collected on a filter mounted in a Faraday cup.

The instrument delivers data on the mean particle diameter (size range: 10 - 300 nm) and number concentration (range: $3 \cdot 10^3$ - 10^6 particle cm^{-3}) with an accuracy of $\pm 30\%$.

The recorded analog signals are digitised and transmitted via Bluetooth to either a PDA or a PC. This feature, in combination with the DiSC's small size (approximately two lap-top computers stacked on each other), comparably light weight (5.5 kg) and capability of battery powered operation for about eight hours, make it a valuable candidate for an on-site monitoring device.

Condensation particle counter, CPC

The CPC (Fig. 1.7, according TSI), a conductive cooling instrument, consists of a saturator, condenser and a particle detector. The principle of the method is to deposit a liquid layer onto the primary particles by condensation which facilitates the detection and size determination by light scattering. The aerosol passes above a reservoir with a liquid kept at an elevated temperature (for butanol: 35°C). The residence time above the reservoir is such that the aerosol stream will be saturated with the vapour of the working fluid at the set temperature. Then the aerosol enters a condenser tube, which is kept at a lower temperature (for instruments using butanol: 10°C) by cooling the wall. In the condenser, gas cooling takes place by conduction and convection, which leads to supersaturation in the cooled aerosol stream. The vapour will condensate on the primary aerosol and form droplets (Baron and Willeke 2001).

Continuous flow CPCs use light-scattering techniques to detect the droplets. Standard CPCs operate in the size range of 10 to 500 nm and up to 10^7 particles cm^{-3} .

Scanning mobility particle sizer, SMPS

The SMPS is basically a combination of two instruments: a differential mobility analyser (DMA) followed by a CPC. A cylindrical DMA is basically a coaxial flow condenser (Fig. 1.8, according TSI). Charged aerosol particles enter the condenser through a narrow slot in the outer electrode. A HEPA (high efficiency particulate air) filtered, particle free sheath flow separates the aerosol particles from the inner high voltage electrode. Downstream from the aerosol injection slot, a classified aerosol sample is extracted.

Due to the charge that the particles carry, they migrate towards the inner electrode. The velocity with which they travel towards the electrode depends on their electrical mobility. Thus, for a given voltage only particles having a mobility within a narrow range are extracted through the slot at the base of the electrode. Particles with a higher mobility impact on the electrode before they reach the slot and particles with a lower mobility are discarded with the excess air.

The particles passing through the slot at the base of the inner electrode are then led to the CPC where they are counted. To get a complete particle size distribution the high tension on the inner electrode is varied in steps - corresponding to discrete size bins. The SMPS used during the different projects (TSI, Model 3034) uses 54 bins to scan the size range from 10 to 500 nm. A complete scan is done in 3 min.

Fast mobility particle sizer, FMPS

The FMPS is, in principle, a combination of an EDB and a DMA (Fig. 1.9, according TSI). After entering the instrument, the particles are positively charged in a corona charger. The aerosol then enters the measurement region near the centre of a high tension electrode column (similar to a DMA column but with inversed polarity). A flow of HEPA filtered sheath air separates the aerosol from the electrometers. The positively charged particles are repelled by the positive voltage applied to the high tension electrode and migrate outward to the electrometers. Particles with a high electrical mobility impact on one of the electrometers located near the top of the stack whereas particles with a low electrical mobility impact on one of the electrometers further down the stack.

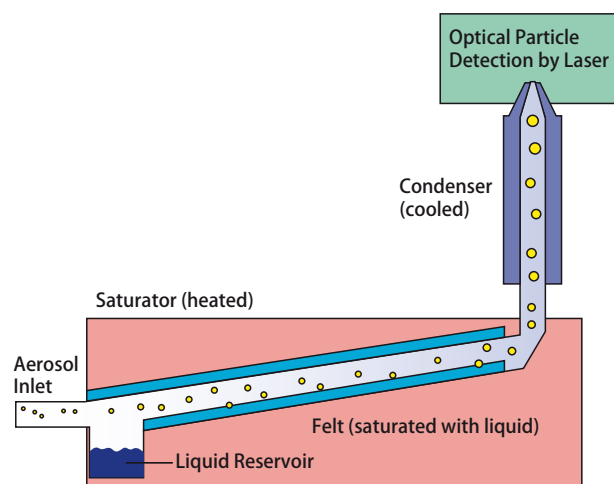


Fig. 1.7: Schematic of a condensation particle counter (CPC) (schematic according TSI). The instrument used for the thesis projects uses butanol like most CPCs. Few instruments use water to condensate on particles.

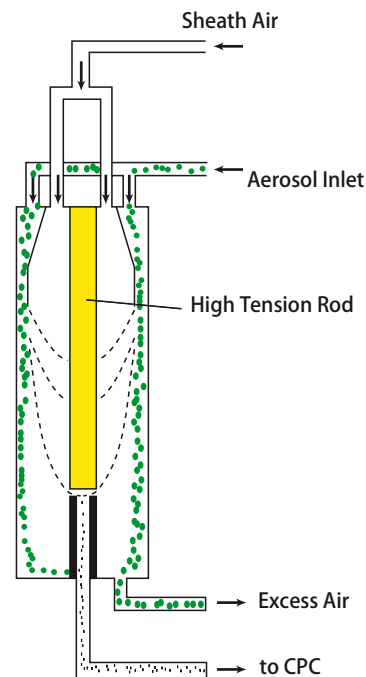


Fig. 1.8: Schematic of a differential mobility analyser (DMA) (schematic according TSI). In a SMPS the DMA is followed by a CPC (Fig. 1.7). The sheath air passes a HEPA (high efficiency particulate air) filter before entering the DMA column.

Instead of varying the voltage and extracting the charged particles at a constant position in the column (as in a DMA), the FMPS keeps the voltage constant and measures the deposited particles with a stack of electrometers all the way along the column. In analogy to the voltage bins of the DMA the electrometers represent size bins for the classification of the particles. The FMPS used for our projects (TSI, Model 3091) is equipped with a stack of 32 electrometers, the positions of which correspond to particle diameters from 5.6 nm to 560 nm, and has a time resolution of 1 s.

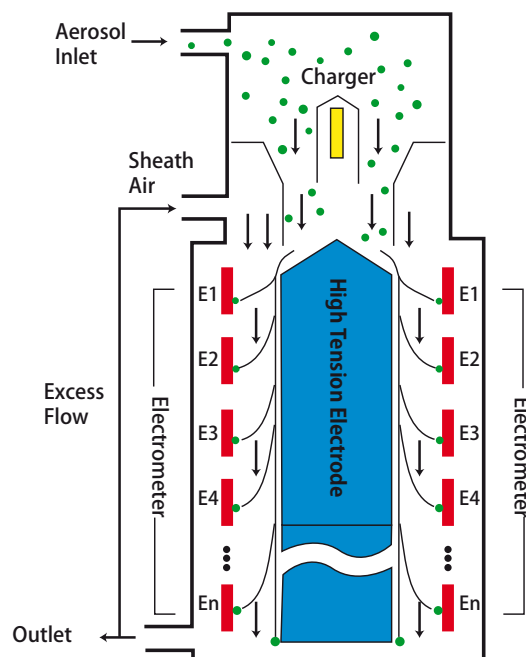


Fig. 1.9: Schematic of a FMPS (according TSI). As the EDB, the FMPS uses electrometers to register particles, thus, realising a high time resolution (1 s). Through the "inverse DMA" principle, complete size distributions can be recorded simultaneously.

1.2.2 Particle sampling

Online instruments deliver valuable data on the evolution of particle size distributions and number concentrations. However, to get information on particle morphology, crystallography and chemistry, offline analysis is required.

For the projects of this thesis electron microscopy was to be used for the particle analysis. To get as much information from the particle samples as possible, sampling devices need to fulfil a series of requirements. They have to allow the collection of particles directly onto substrates feasible for subsequent microscopic analysis, without further sample preparation (except coating). The devices need to be calibrated to get quantitative (composition dependent) particle size distributions from single particle analysis. And finally, particles need to be well separated on the substrates without size fractionation occurring.

To provide a base for the following chapters, the sampling devices used for the project are briefly described.

Impaction and filtration

To collect particles of the continuum regime, comparably simple impaction/filtration devices suffice. Figure 1.10 shows a schematic of the collection device designed for the study described in chapter 2.

To avoid additional sample preparation prior to the analysis in a environmental scanning electron microscope (ESEM), only filters with a flat surface (e.g., Nuclepore®) have to be selected. Sampling efficiency is 100% for particles larger than the pore size of the filters used.

More critical is the particle deposition characteristic on the filter. To ensure a homogeneous particle distribution without size fractionation, any changes in the profile of the aerosol flow prior to the filter need to be avoided. If a pre-impactor is to be used to allow only particles smaller than a certain size to reach the filter, the connecting tube between the impactor and the filter holder needs to be long enough to guarantee of a stable flow profile. More detailed information on the device can be found in section 2.3.

Thermophoresis

The collection of transition regime particles for direct subsequent analysis in a TEM cannot be done by impaction. One of the precipitation mechanism applicable is thermophoresis. Chapter 3 is dedicated to the development of a sampling device operating by this principle. Accordingly, only a short introduction will be given at this point.

Figure 1.11 shows a diagram of the basic principle of the device. Particles flying through a temperature gradient are deflected towards the cooler side, where the sampling grid is positioned. An advantage of the method is that the depo-

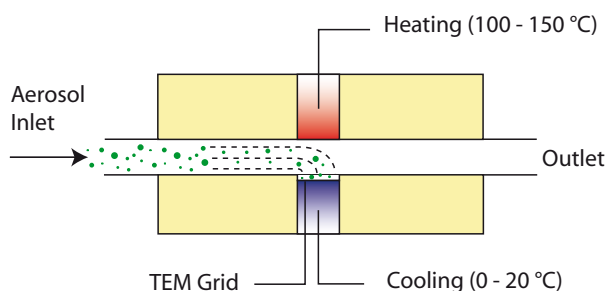


Fig. 1.11: Schematic of the basic principle of thermophoretic sampling devices. Due to the difference in kinetic energy carried by the molecules from the cold resp. hot side of the flow channel, particles get gradually deflected towards the cooler side. (s. ch. 3)

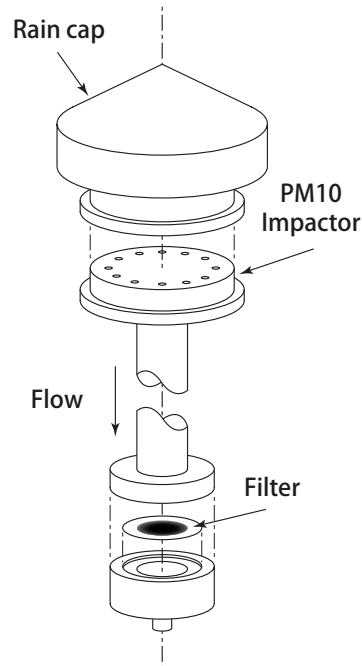


Fig. 1.10: Schematic of the impactor/filter holder assembly developed for the study on the emissions of a railway line. For details on the study see chapter 2 and for specific information on the sampling device section 2.3.

sition efficiency is independent of particle size for the free molecular and the transition regime. For larger particles, corrections have to be applied.

Electrophoresis

The high electrical mobility of transition regime particles is utilised in precipitators operating by the principle of electrophoresis. Figure 1.12 shows a diagram of the principle components of electrostatic sampling devices.

Particles first enter a corona charger. They are then guided head-on to a high tension electrode with a TEM grid sitting on top. With the high tension switched off, particles follow the flow lines and pass the electrode without settling on the grid. After the electrode, a backup filter mounted in a Faraday cup collects the particles. The current measured in the filter gives a first, rough estimate of the particle number concentration in the aerosol.

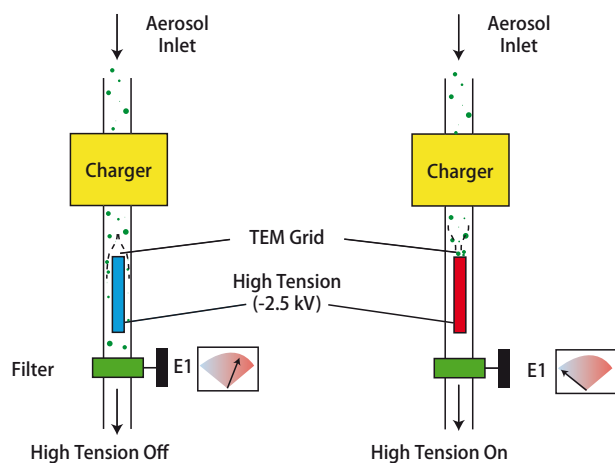


Fig. 1.12: Schematic of an electrostatic sampling device. Without the high tension all charged particles are collected on the backup filter. The current measured on the filter gives an estimate on the particle number concentration. (Fierz *et al.* 2007)

With the high tension turned on particles will settle on the grid and on the electrode. Accordingly, if the device functions properly, the current measured on the backup filter should drop considerably.

Since the electrical mobility is dependent on the particle size, electrostatic precipitators need to be calibrated. A detailed description of the device used for the projects of this thesis and the calibration process applied can be found in Fierz *et al.* (2007).

1.3 Thesis outline

The focus of this thesis lies in the construction and application of sampling devices for fine and ultrafine particles, the development of sampling and analysis strategies for characterisation and apportionment of particle sources in general and in the context of occupational health.

As an introduction into the world of aerosols, a project investigating the emissions of a railway line was performed (chapter 2). In this study single particle analysis was used to quantify the contribution of railway traffic to ambient PM10 concentrations. Based on a detailed single particle analysis of samples collected at different distances from the railway lines, an emission profile of the railway was derived. The railway induced PM10 concentrations were obtained by calculating the individual particle volumes (based on their morphological parameters) and multiplying them with a density derived from the analysed chemical composition. The obtained PM10 concentrations are

compared to gravimetrically determined PM10 concentrations from another study performed at the same sampling site.

To level the ground for studies on sources of ultrafine particles, a thermophoretic sampling device was developed (chapter 3). In the respective study a combination of a thermophoretic precipitator and a numerical model is described that allows the quantification of number concentrations and particle size distributions of ultrafine aerosols based exclusively on single particle analysis with electron microscopes.

The final project selected for publication focuses on occupational health (chapter 4). Therein we propose a measurement strategy suitable for the periodic assessment of the exposure to ultrafine particles at a work place and we evaluate online instruments for the continuous monitoring of the exposure situation. The proposed combination of online monitoring of the emission and offline chemical and morphological analysis of the emitted ultrafine particles with analytical electron microscopy (AEM) allows a complete characterisation of the specific working area. The time resolved particle number concentration measurements as well as the detailed analysis of the chemical composition, the morphology and the surface properties of individual particles results in a comprehensive data set required to design toxicological studies related specifically to occupational health.

The concluding chapter (ch. 5) of this thesis gives a short outlook on possible courses of action, based on the knowledge gained during the projects executed.

References

- Anderson, P.J., Wilson, J.D. and Hiller, F.C. (1990). Respiratory tract deposition of ultrafine particles in subjects with obstructive or restrictive lung disease. *Chest*. 97:1115-1120.
- Baron, P. A. and Willeke, K., eds. (2001). *Aerosol Measurements: Principals, Techniques, and Applications*. John Wiley & Sons, New York.
- Berry, J.P., Arnoux, B., Stanislas, G., Galle, P. and Chretien, J. (1977). A microanalytic study of particle transport across the alveoli: role of blood platelets. *Biomedicine*. 27:354-357.
- Blundell, G., Henderson, W.J. and Price, E.W. (1989). Soil particles in the tissues of the foot in endemic elephantiasis of the lower legs. *Ann. Trop. Med. Parasitol.* 83(4):381-385.
- Brouwer, D. H., Gijssbers, J. H. J. and Lurvink, M. W. M. (2004). Personal exposure to ultrafine particles in the workplace: Exploring sampling techniques and strategies. *Ann. Occup. Hyg.* 48:439-453.
- Brown, D.M., Stone, V., Findlay, P., MacNee, W. and Donaldson, K. (2000). Increased inflammation and intracellular calcium caused by ultrafine carbon black is dependent of transition metals or other soluble components. *Occup. Environ. Med.* 57:685-691.
- Brown, D.M., Wilson, M.R., MacNee, W., Stone, V. and Donaldson, K. (2001). Size-dependent proinflammatory effects of ultrafine polystyrene particles: a role of surface area and oxidative stress in the enhanced activity of ultrafines. *Toxicol. Appl. Pharmacol.* 175:191-199.
- Brown, J.S., Zeman, K.L. and Bennett, W.D. (2002). Ultrafine particle deposition and clearance in the healthy and obstructed lung. *Am. J. Respir. Crit. Care Med.* 166:1240-1247.
- Chalupa, D.C., Morrow, P.E., Oberdorster, G., Utell, M.J. and Framp-ton, M.W. (2004). Ultrafine particle deposition in subjects with asthma. *Environ. Health Perspect.* 112:879-882.
- Coleman, W.E., Scheel, L.D. and Gorski, C.H. (1968). The particle resulting from polytetrafluorethylene (PTFE) pyrolysis in air. *AHIA J.* 29:54-60.
- Corachan, M., Tura, J.M., Campo, E., Soley, M. and Traveria, A. (1988). Poedoconiosis in Aequatorial Guinea. Report of two cases from different geological environments. *Trop. Geogr. Med.* 40:359-364.
- Coulier, P.J. (1875). Note sure une nouvelle proprieté de l'air. *J. Pharm. Chim. Paris Ser. 4*. 22(1):165-172.
- Donaldson, K., Li, X.Y. and MacNee, W. (1998). Ultrafine (nanometre) particle mediated lung injury. *J. Aerosol Sci.*29:553-560.
- Donaldson, K. and Tran, C.-L. (2002). Inflammation caused by particles and fibres. *Inhal. Toxicol.* 14:5-27.
- Donaldson, K., Brown, D., Clouter, A., Duffin, R., MacNee, W., Renwick, L., *et al.* (2002). The pulmonary toxicology of ultrafine particles. *J. Aerosol Med.* 15:213-220.
- Donaldson, K. and Stone, V. (2003). Current hypotheses on the mechanisms of toxicity of ultrafine particles. *Ann. Ist. Super Sanita.* 39:405-410.
- Driscoll, K.E. (1996). Role of inflammation in the development of rat lung tumors in respons to chronic particle exposure. *Inhal. Toxicol.* 8(suppl):139-153.
- Feikert, T., Mercer, P., Corson, N., Gelein, R., Opanashuk, L., Elder, A., *et al.* (2004). Inhaled solid ultrafine particles (UFP) are efficiently translocated via neuronal naso-olfactory pathways [Abstract]. *Toxicologist.* 78(suppl 1):435-436.
- Fierz, M., Scherrer, L. and Burtscher, H. (2002). Real-time measurement of aerosol size distributions with an electrical diffusion battery. *J. Aerosol. Sci.* 33:1049-1060.
- Fierz, M. and Burtscher, H. (2005). A portable diffusion size classifier, in *European Aerosol Conference*. W. Maenhaut, ed. Gent, Belgium, 423.
- Fierz, M., Kaegi, R. and Burtscher, H. (2007). Theoretical and experimental evaluation of a portable electrostatic TEM sampler. *Aerosol Science and Technology* 41:520-528.

- Greim, H., Borm, P., Schins, R., Donaldson, K., Driscoll, K., Hartwig, A., *et al.* (2001). Toxicity of fibres and particles - report of the workshop held in Munich, Germany, 26 - 27 October 2000. *Inhal. Toxicol.* 13:737-754.
- Griffith, F.D., Stephens, S.S. and Tayfun, F.O. (1973). Exposure of Japanese quail and parakeets to the pyrolysis products of fry pans coated with teflon and common cooking oils. *Am. Ind. Hyg. Assoc. J.* 34:176-178.
- Heckel, K., Kiefmann, R., Dorger, M., Stoeckelhuber, M. and Goetz, A.E. (2004). Colloidal gold particles as a new *in vivo* marker of early acute lung injury. *Am. J. Physiol. Lung Cell Mol. Physiol.* 287:L867-L878.
- Heinrich, U. (2004). *Effects of Air Contaminants on the Respiratory Tract - Interpretations from Molecular to Meta Analysis*. p.181-194. Fraunhofer IRB Verlag, Stuttgart, Germany.
- Hinds, W.D. (1999). *Aerosol Technology*. John Wiley & Sons, New York.
- Hunter, D.D. and Dey, R.D. (1998). Identification and neuropeptide content of trigeminal neurons innervating the rat nasal epithelium. *Neuroscience*. 83:591-599.
- Hunter, D.D. and Udem, B.J. (1999). Identification and substance P content of vagal afferent neurons innervating the epithelium of the genuine pig trachea. *Am. J. Respir. Crit. Care Med.* 159:1943-1948.
- IARC (International Agency for Research on Cancer). (2002). Man-made vitreous fibres. *IARC Monogr. Eval. Carcinog. Risks Hum.* 81:1-418.
- Jaques, P.A. and Kim, C.S. (2000). Measurement of total lung deposition of inhaled ultrafine particles in healthy men and women. *Inhal. Toxicol.* 12:715-731.
- Kreyling, W., Semmler, M., Erbe, F., Mayer, P., Takenaka, S., Schulz, H., *et al.* (2002). Translocation of ultrafine insoluble iridium particles from lung epithelium to extrapulmonary organs is size dependent but very low. *J. Toxicol. Environ. Health.* 65A:1513-1530.
- Li, N., Sioutas, C., Cho, A., Schmitz, D., Misra, C., Sempf, J., *et al.* (2003). Ultrafine particulate pollutants induce oxidative stress and mitochondrial damage. *Environ. Health Perspect.* 111:455-460.
- Lorenzo, R., Kaegi, R., Gehrig, R., Scherrer, L. and Grobety, B. (2006). A thermophoretic precipitator for the representative collection of atmospheric ultrafine particles for microscopic analysis. *Aerosol Science and Technology* : submitted.
- Maynard, A. D. and Kuempel, E. D. (2005). Airborne nanostructured particles and occupational health. *J. Nanopart. Res.* 7:587-614.
- Mehta, D., Bhattacharya, J., Matthay, M.A. and Malik, A.B. (2004). Integrated control of lung fluid balance. *Am. J. Physiol. Lung Cell Mol. Physiol.* 287:L1081:1090.
- NIOSH (National Institute for Occupational Safety and Health). (2006). Approaches to Safe Nanotechnology: An Information Exchange with NIOSH. Approaches to Safe Nanotechnology: An Information Exchange with NIOSH *on-line resource* : <http://www.cdc.gov/niosh/topics/nanotech/safenano/>.
- Oberdorster, G. and Yu, C.P. (1990). The carcinogenic potential of inhaled diesel exhaust: a particle effect? *J. Aerosol Sci.* 21(suppl 1):S397-S401.
- Oberdorster, G., Ferin, J., Gelein, R., Sonderholm, S.C. and Finkelstein, J. (1992). Role of the alveolar macrophage in lung injury: studies with ultrafine particles. *Environ. Health Perspect.* 97:193-197.
- Oberdorster, G., Gelein, R.M., Ferin, J. and Weiss, B. (1995). Association of particulate air pollution and acute mortality: involvement of ultrafine particles? *Inhal. Toxicol.* 7:111-124.
- Oberdorster, G., Finkelstein, J.N., Johnston, C., Gelein, R., Cox, C., Baggs, R., *et al.* (2000). Acute pulmonary effects of ultrafine particles in rats and mice. *Res. Rep. Health Eff. Inst.* 96:5-74.
- Oberdorster, G., Sharp, Z., Atudorei, V., Elder, A., Gelein, R., Kreyling, W. and Cox, C. (2004). Translocation of inhaled ultrafine particles to the brain. *Inhal. Toxicol.* 16:437-445.
- Oberdorster, G., Oberdorster, E. and Oberdorster, J. (2005). Nanotoxicology: An emerging discipline evolving from studies of ultrafine particles. *Environ. Health Perspect.* 113:823-839.
- Pekkanen, J., Timonen, K.L., Ruuskanen, J., Reponen, A. and Mirme, A. (1997). Effects of ultrafine and fine particles in urban air on peak expiratory flow among children with asthmatic symptoms. *Environ. Res.* 74:24-33.
- Penttinen, P., Timonen, K.L., Tiittanen, P., Mirme, A., Ruuskanen, J. and Pekkanen, J. (2001). Ultrafine particles in urban air and respiratory health among adult asthmatics. *Eur. Resp. J.* 17:428-435.
- Peters, A., Doring, A., Wichmann, H.-E. and Koenig, W. (1997a). Increased plasma viscosity during an air pollution episode: a link to mortality? *Lancet.* 349:1582-1587.
- Peters, A., Wichmann, H.-E., Tuch, T., Heinrich, J. and Heyder, J. (1997b). Respiratory effects are associated with the number of ultrafine particles. *Am. Respir. Crit. Care Med.* 155:1376-1383.
- Rejman, J., Oberle, V., Zuhorn, I.S. and Hoekstra, D. (2004). Size-dependent internalisation of particles via the pathways of clathrin- and caveolae-mediated endocytosis. *Biochem. J.* 377:159-169.
- Semmler, M., Seitz, J., Erbe, F., Mayer, P., Heyder, J., Oberdorster, G., *et al.* (2004). Long-term clearance kinetics of inhaled ultrafine insoluble iridium particles from rat lung, including transient translocation into secondary organs. *Inhal. Toxicol.* 16:453-459.
- Spurny, K.R. (1999). *Analytical chemistry of aerosols*. Lewis Publishers, Boca Raton, USA.
- Tinkle, S.S., Antonini, J.M., Rich, B.A., Roberts, J.R., Salmen, R., DePree, K., *et al.* (2003). Skin as a route of exposure and sensitization in chronic beryllium disease. *Environ. Health Perspect.* 111:1202-1208.
- Tran, C.L., Jones, A.D., Cullen, R.T. and Donaldson, K. (1998). Influence of particle characteristics on the clearance of low toxicity dusts from lungs. *J. Aerosol Sci.* 29(suppl 1):S1269-S1270.
- Tran, C.L., Buchanan, D., Cullen, R.T., Searl, A., Jones, A.D. and Donaldson, K. (2000). Inhalation of poorly soluble particles. II. Influence of particle surface area on inflammation and clearance. *Inhal. Toxicol.* 12:1113-1126.
- U.S. EPA. (2004). Air Quality Criteria for Particulate Matter. Vol. 3. 600/P-95-001cF. Washington
- Vincent, J. H. (2005). Health-related aerosol measurement: a review of existing sampling criteria and proposals for new ones. *J. Environ. Monit.* 7:1037-1053.
- von Klot, S., Wolke, G., Tuch, T., Heinrich, J., Dockery, D.W., Schwartz, J. *et al.* (2002). Increased asthma medication use in association with ambient fine and ultrafine particles. *Eur. Respir. J.* 20:691-702.
- Wichmann, H.-E., Spix, C., Tuch, T., Wolke, G., Peters, A., Heinrich, J., *et al.* (2000). Daily Mortality and Fine and Ultrafine Particles in Erfurt, Germany. Part I: Role of Particle Number and Particle Mass. *Res. Rep. Health Eff. Inst.* 98:5-86.
- Wichmann, H.-E., Schlipkötter, H.W. and Fülgraff, G. (2002). *Wortschritte in der Umweltmedizin*. Ecomed Publishers, Erfurt, Germany.
- Wiesner, M. R., Lowry, G. V., Alvarez, P., Dionysiou, D. and Biswas, P. (2006). Assessing the risks of manufactured nanomaterials. *Environ. Sci. Technol.* 40:4336-4345.
- Yamago, S., Tokuyama, H., Nakamura, E., Kikuchi, K., Kananishi, S., Sueki, K., *et al.* (1995). In vivo biological behaviour of a water-miscible fullerene: ¹⁴C labeling, absorption, distribution, excretion and acute toxicity. *Chem. Biol.* 2:385-389.

Particle Emissions of a Railway Line

- Introduction
- Publication
- Technical Details

*«Guess Spock, your best guess.»
«Guessing is not in my nature doctor.»
«Well, nobody's perfect.»
McCoy and Spock, Star Trek IV*

2 Particle Emissions of a Railway Line

2.1 Introduction

2.1.1 PhD Thesis: Introductory project

One of the objectives of the thesis was the analysis of railway traffic as potential particle source and to establish the corresponding source apportionment. This project was also to be understood as a door opener into the experimental work with and the analysis of aerosols.

Collecting PM10 is considerably less critical than PM0.1 for losses due to diffusion, thermophoresis or electrophoresis can easily be avoided. The only sources for artefacts and systematic errors are sample preparation and/or inhomogeneous particle deposition on the filters, depending on the filter medium used and sampling process applied. For this project conventional PM10 samplers were used (for details see chapter 2.3)

Since the analysis of the filters was scheduled to be done by single particle analysis on a environmental scanning electron microscope (ESEM), Nuclepore® polycarbonate filters with 0.4 µm pore size were chosen as sampling substrate. Due to their flat surface no further sample preparation was required. The problem of inhomogeneous particle deposition was avoided by developing specialised filter holders (more details in chapter 2.3).

Chemical and morphological analysis of the individual particles were done by energy dispersive spectroscopy and image analysis respectively. Once the particle analysis was done, an appropriate data mining concept had to be developed. Since it was uncertain whether single particle analysis could deliver data comparable to traditional methods (such as gravimetry), considerable effort was put into interpreting the microscope data. Automation of the analysis allowed the determination of particle size distributions as function of particle chemistry.

2.1.2 Broader context

In 2001 the Federal Office for the Environment (FOEN, German: BUWAL) prepared a study on potential measures to reduce PM10 emissions, which has never been officially published. This study estimated the contribution of the railway to the total national PM10 emissions (28'220 t a⁻¹ to 2'800 t a⁻¹ (in a draft of the study from 2000 even 3'361 t a⁻¹) while the contribution of the on-road goods traffic was 3'246 t a⁻¹. The hauling contractors criticized the fact that this study was seemingly withheld (see: Curia Vista, Bulletin 00.5229). In contrast to the Swiss Federal Railways (SBB), hauling contractors have to pay for their PM10 emissions and felt wronged by the different treatment. This difference was rectified by the federal council with the argument that the railways' contribution to the PM10 emissions is negligible. If the emission estimates given by the FOEN study were correct, the federal council would have indeed some explaining to do.

At a closer look it turns out that the FOEN study from 2001 was based, in part, on an investigation done by Carbotec plc. in 2000 (BUWAL 2000). The problem with this study is that its estimate of the railway emissions is not based on actual measurements but on the abrasive mass losses of wheels, brakes and tracks. This is, of course, problematic at best. Accordingly, a more sound study was commissioned.

In 2003 and 2004 an extended and representative field study was performed by Gehrig *et al.* (2007). Part of the concept for this investigation included the measurement of a distance dependent profile at the Juchhof near Zurich (Switzerland). Samples were collected on quartz fibre filters with high volume samplers (Digitel DHA 80).

A revised report based on the findings of the study by Gehrig *et al.* (2007) estimated the PM10 emissions of the Swiss federal railway to 800 - 1'200 t a⁻¹ (BAFU 2006). Bad news for the hauling contractors...

References

- BAFU (2006). PM10-Emissionen des Verkehrs, 2. Statusbericht Teil Schienenverkehr. *Schriftenreihe Umwelt-Materialien*. in press. Bern, Swiss Federal Office for the Environment.
- BUWAL (2000). PM10-Emissionsfaktoren: Mechanischer Abrieb im Offroad-Bereich. Swiss Federal Office for Environment, Forest and Landscape, Bern. *Carbotec AG*, Basel.
- BUWAL (2001). Massnahmen zur Reduktion der PM10-Emissionen. Swiss Federal Office for Environment, Forest and Landscape, Bern. *Electrowatt Engineering AG*, R. Kropf:112.
- Gehrig, R., Hill, M., Lienemann, P., Zwicky, C. N., Bukowiecki, N., Weingartner, E., Baltensperger, U. and Buchmann, B. (2007). Railway traffic – a source of fine particles? Contribution of railway traffic to local PM10 concentrations in Switzerland. *Atmos. Environ.* 41:923-933.

Particle emissions of a railway line determined by detailed single particle analysis

R. Lorenzo^{a,b}, R. Kaegi^a, R. Gehrig^a, B. Grob ty^b

^aEmpa, Materials Science & Technology, Laboratory for Air Pollution & Environmental Technology,  berlandstrasse 129, CH-8600 D bendorf, Switzerland

^bUniversity of Fribourg, Institute for Mineralogy and Petrography, Ch. du Musee 6, CH-1700 Fribourg, Switzerland

Received 14 November 2005; received in revised form 24 July 2006; accepted 24 July 2006

Abstract

The goal of this study was to identify and quantify particles emitted from railway traffic. For that purpose PM10 samples were collected near a busy railway line using a wind direction and speed controlled sampling equipment consisting of five devices. Measurements taken perpendicular to the railway lines at 10 m, 36 m and 120 m distance enable an identification and separation of particles caused by the railway traffic from background particles. Morphology and chemistry of more than 11'000 particles were analyzed by computer controlled scanning electron microscopy (CCSEM). Based on chemical composition five particle classes are defined and assigned to their sources. The mass of the individual particles is determined by multiplying their volumes, calculated based on their morphology with a density assigned specifically to each particle class. The density of the particle classes is derived from their chemical composition. To estimate the PM10 contributions of the railway lines, the mass of PM10 at 120 m (background, not influenced by the railway lines) is subtracted from the mass of PM10 at 10 m. The emissions of the railway lines are dominated by 'iron' particles, which contribute $2.9 \mu\text{g m}^{-3}$ or 67% to the railway related PM10. In addition, 'aluminium' and 'calcium' particles contribute also to the railway related PM10 ($1.0 \mu\text{g m}^{-3}$ or 23% for the 'aluminium' and $0.4 \mu\text{g m}^{-3}$ or 10% for the 'calcium' particles). These particles are assigned to abrasion of the gravel bed and re-suspension of mineral dust.

Long-term gravimetric results of the contribution of iron to the mass of railway related PM10 from a study performed earlier at the same site are in good agreement with the data presented in this study.

  2006 Elsevier Ltd. All rights reserved.

Keywords: SEM/EDX; Particle analysis; Morphology; Railway; PM10

1. Introduction

Adverse health effects of airborne particulate matter are reviewed in numerous studies (Harrison and Yin 2000; Oberdorster 1995a; Oberdorster *et al.* 1995b; Pope 2000). Anthropogenic emissions of particulate matter largely result from industry, heating installations and traffic. A considerable fraction of the total human exposure to particulate matter results from traffic. The contribution of road traffic has been investigated in detail in the BAB II project (Rosenbohm *et al.* 2005).

Particulate emissions of railway traffic have only been addressed in a few studies which focus on subway systems. Adams *et al.* (2001) used gravimetric high flow personal samplers to study the PM2.5 personal exposure level during journeys in the subway system of London. A similar study in the Stockholm underground was performed by Johansson and Johansson (2003). They used a tapered element oscillating microbalance (TEOM) to measure the PM10 and PM2.5 concentrations on the platform. The personal exposure to airborne metals and total suspended particulate matter of commuters in the London underground was the subject of a study by Pfeifer *et al.* (1999). In addition to gravimetric methods they used inductively coupled plasma-mass spectroscopy (ICP-MS) to get information on the chemical composition of the bulk aerosol. The same methods were used by Chillrud *et al.* (2004) to investigate the exposure of teenagers to Mn, Cr and Fe in the New York subway.

In addition to gravimetry Aarnio *et al.* (2005) monitored the particle number concentrations with a differential mobility particle sizer (DMPS) and determined the elemental composition of the PM2.5 in the Helsinki subway system using energy dispersive X-ray fluorescence (EDXRF). However, no information on the level of the individual particles has been collected. Birenzvi e *et al.* (2003) used a single particle fluorescence analyser to count, size and distinguish between bio aerosols and other aerosols. In addition, a limited number of selected single particles were manually analyzed with a scanning electron microscope.

The use of single particle analysis to obtain more detailed information about size, morphology and chemical composition on the level of the individual particle has been documented in many papers (Katrinak *et al.* 1995; Paoletti *et al.* 1999; Sitzmann *et al.* 1999; VanBorm and Adams 1988; VanMalderen *et al.* 1996a, b; Xhoffer *et al.* 1991).

In this study single particle analysis was used to quantify the contribution of railway traffic to ambient PM10 concentrations. Based on a detailed single particle analysis of samples collected at different distances from the railway lines, an emission profile of the railway was derived. The railway induced PM10 concentrations were obtained by calculating the individual particle volumes (based on their morphological parameters) and multiplying them with a density derived from the analyzed chemical composition. The obtained PM10 concentrations are compared to gravimetrically determined PM10 concentrations from another study performed at the same sampling site.

2. Experimental

2.1 Sampling site

The sampling campaign was conducted at Juchhof near Zurich (Switzerland), a sport centre with several football grounds next to a busy railway line with more than 700 trains per day, all electricity powered. No other major particle source (e.g. power plants, heavy industry) can be found nearby. Since the campaign took place during December 2004 and the training fields were closed for winter, no activities and hardly any local road traffic disturbed the measurements. The closest busy roads are about 200 m to the south and about 250 m to the north, respectively; the bridge crossing the railway lines is frequented only by very few vehicles (Figure 2.1). Due to snowfall the week before the campaign, gravel from traction sanding was still present on public roads. However, the snow melted completely before the measurements and conditions were dry for the duration of the campaign.

Five PM10 sampling devices were deployed according to the layout given in Figure 2.1. To distinguish particle emissions of the railway from background, three sampling devices were positioned at 10 m, 36 m and 120 m from the railway lines. To estimate the reproducibility of the measurements two additional devices were placed at 10 m from the tracks 50 m to either side of the three devices just mentioned.

The five sampling devices were operated simultaneously and switched on and off by a wind direction and speed sensor (see Figure 2.1 and Table 2.1 for details) in order to ensure that the sampling only occurred with wind directions from railway influenced sectors. The wind parameters were measured at the central 10 m position, 4 m above ground level.

2.2 Sampling and analysis

To investigate single particles by electron microscopy it is essential to limit the sampling time and hence the filter load in a way to get well separated particles on the filter and to avoid multiple particle deposition on the same filter spot. Further, it is critical to have a homogeneous distribution of particles on the filter. This enables a quantification of the results which are based on the analysis of a small fraction of the filter area only.

We performed several experiments to check the homogeneity of the particle distribution on the filters of our PM10 samplers and to optimise the sampling time (filter load). Several areas (0.08 mm² each) of a filter were analyzed using computer controlled scanning electron microscopy (CCSEM). The relative standard deviation of the particle number on the filter between the different fields was

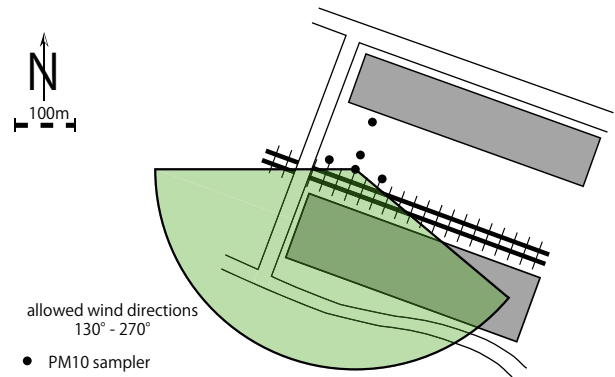


Fig. 2.1: Schematic representation of the sampling area.

about 10% and no size fractionation could be observed. The final parameters used for the measurements near the railway lines are derived from these results and are listed in Table 2.1.

Particles were sampled on Nuclepore filters (0.4 µm pore diameter). Five areas on each filter were analyzed. For that purpose, five concentric rings with equal areas were defined on each filter and one rectangular area out of every ring was selected and analyzed. In total an area of 0.4 mm² was investigated on each filter. The filters were analyzed with an environmental scanning electron microscope (ESEM, FEI XL 30 FEG) without any further treatment. Elemental analysis was performed with an energy dispersive X-ray spectrometer (EDX, EDAX), attached to the microscope. The experimental parameters for the analysis are given in Table 2.2.

Particles were detected based on their backscattered electron signal and individually analyzed using the EDX signal. Images and analytical data of all particles were stored automatically.

For further analysis a minimum particle diameter of 0.5 µm (projected area equivalent diameter) was chosen. Smaller particles were discarded as the resulting EDX signal was often too weak. To determine the detection limits of the elements of interest and to verify the spectra of specific particles, all EDX spectra were manually reviewed. In total approximately 11'000 particles were analyzed and of these more than 90% could be classified using our classification scheme (Figure 2.2). The main reason for non-classified particles was mechanical and/or electronic shifts of the sample or beam during data acquisition. Therefore, the corresponding EDX spectra resulted from the filter rather than from the particle. A small portion of particles (~1%) consisted of elements not considered by our classification algorithm, such as Ti or Cu.

Table 2.1
Table of parameters used for the final sampling run.

Sampling Parameter			
Filter	Setup		
Type	Nuclepore®	Number of Samplers used	5
Pore Diameter	0.4 µm	Flow	4 l min ⁻¹
Filter Diameter	2.5 cm	Sampling Period	6.-10. December 2004
		Sampling Time (wind conditions within specified ranges)	4 h
		Range of Wind Speeds	0.4 - 10 m s ⁻¹
		Range of Wind Directions	130 - 270 °

3. Results and discussion

3.1 Classification of the particles

The net intensities of the EDX spectra were used as a basis for the classification of the particles. The flow chart given in Figure 2.2 describes the algorithm used to distinguish five particle classes. Since particles were sampled on polycarbonate filters, the O-peak was not used for particle classification. The classification scheme is based on mineralogical criteria. Geological particles are essentially silicates (feldspars, quartz and clays) with minor amounts of carbonates (calcite) and sulphates (gypsum). The chemistry of these particles can be unambiguously distinguished from Fe particles (metals, oxides), which are caused by the local railway lines. Thus, the classification criteria as shown in Figure 2.2 are unequivocal.

$$I_p > 3\sqrt{\frac{I_B}{t}} + I_B \quad (1)$$

To calculate the detection limits for the individual elements the three-sigma criterion (1) was applied, where I_p is the intensity of the peak (counts per second), I_B the background intensity and t the acquisition time. In the following paragraphs, the different classes will be briefly described.

3.1.1 'Iron' class

Particles of this class consist almost entirely of iron. Occasionally, minor amounts of other elements were detected caused by smaller particles sitting on top of - or close to - the iron particles.

Most of the iron particles are spherical in shape and some of them were cracked and appeared to be hollow. The morphology indicates that these particles were generated by a high temperature process. Other particles looked like splinters and were most likely generated by mechanical abrasion.

3.1.2 'Aluminium' class

The particles of the 'aluminium' class consist mostly of aluminium and silica and were assigned to feldspars. This is, of course, a simplification due to the fact that our classification scheme does not distinguish between feldspars and clay minerals. However, the error in the calculated mass of the particles resulting from this simplification is rather small, as the densities of these minerals are similar.

Among the particles of the 'aluminium' class two different shapes were observed. About half of the particles appear as fragments and are probably the result of mechanical abrasion. The other half of the particles are spherical in shape, which indicates that they were generated by a high temperature process.

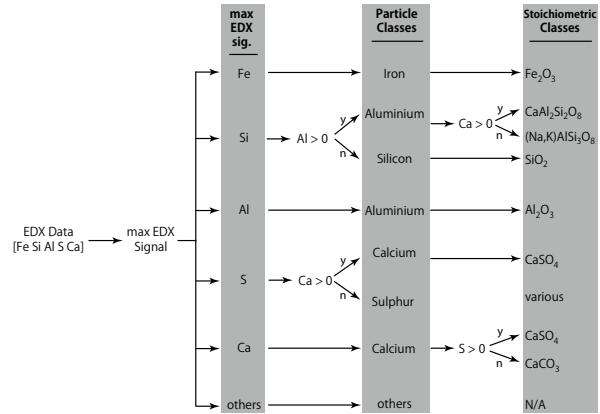


Fig. 2.2: Algorithm for particle classification.

Feldspar was found as component of the gravel underneath the railway tracks. During breaking enough heat is produced to melt iron particles. This temperature is also high enough to melt feldspar particles, which could explain the spherical shapes.

3.1.3 'Silicon' class

Most of the particles of the 'silicon' class (~99%) consist entirely of silicon and could therefore be identified as quartz. Particles of the 'silicon' class were dominantly fragments with sharp edges, a typical morphology of fractured quartz. Quartz was also found as component of the gravel underneath the railway tracks.

3.1.4 'Calcium' class

The 'calcium' class consists of particles dominated by calcium. In addition, sulphur dominated particles with calcium above the detection limit were also assigned to the 'calcium' class.

Particles of the 'calcium' class were angular fragments with a variety of shapes. Sharp edges indicate that these particles are abrasion products. Carbonate rocks were also found in the gravel beneath the railway tracks.

3.1.5 'Sulphur' class

For particles of the 'sulphur' class, sulphur had to be the strongest EDX signal and calcium had to be below the detection limit.

Images taken at higher magnifications revealed that 'sulphur' class particles are mostly chains and fractal-like structures consisting of spheres smaller than 40nm in diameter, commonly described as soot (Buseck *et al.* 2000; Chen *et al.* 2005; Li *et al.* 2003a; Li *et al.* 2003b; Posfai *et al.* 2003). These particles are most likely sulphur coated soot particles and were thus assigned to vehicular exhausts.

Table 2.2
Table of parameters used for the analysis of the five filters.

ESEM / EDX Parameters			
ESEM		EDX	
High Tension	15 kV	Image Resolution	512 x 400 px
Pressure	0.9 torr	Particle Sizes	0.5 - 15 μ m
Spot Size	3	Acquisition Time	15 s (live)
Magnification	4 kx	Particles Analyzed	>11'000 (all filters)
Area Analyzed (per filter)	0.4 mm ²		

Alternatively particles of this class appeared as smooth, irregularly shaped particles which might be fragments of biological particles.

3.1.6 'Other' particles

A small fraction of the analyzed particles (<10%) could not be classified based on our algorithm. This can be caused by one of the following reasons: The particle shifted during the image acquisition, the software combined two touching particles or the particle consisted entirely of elements not considered in our classification, such as Ti or Cu.

A manual review of the recorded EDX spectra showed that the majority of the not classified particles shifted during image acquisition and, thus, can be attributed to software errors. The remainder of the particles not classified consisted of elements not considered in our analysis.

3.2 Profiles perpendicular to the railway line

Figure 2.3 shows the change in particle number for each particle class with increasing distance from the railway lines. The average of the three measurements at 10 m distance is used for the 10 m site in Figure 2.3. The standard deviations were calculated from these three simultaneous measurements and are given as two sigma error bars. As the sampling and analysis method was identical, the same relative standard deviation has also been used to estimate the two sigma error margins for the measurements at 36 m and 120 m distance.

All particle types, except the 'silicon' class, show decreasing number concentrations with increasing distance from the railway. The decrease is in good agreement with the expected changes described by Sharan *et al.* (1996) who developed a mathematical model for atmospheric dispersion in low wind conditions.

The numbers of the 'iron' class particles (black line) drop much faster between 10 m and 36 m than between 36 m and 120 m which shows that the railway traffic is a strong source of particles of the 'iron' class. However, it also indicates that the background concentration for 'iron' particles is not yet reached at 120 m.

The number of 'aluminium' class particles (green line) decreases significantly between the 10 m and the 36 m site but stays constant afterwards. This indicates that the railway lines are a source for 'aluminium' class particles. However, at 36 m the particle numbers already reached the background level for 'aluminium' particles, indicating only a moderate contribution from the railway traffic to the 'aluminium' class particle number concentration of PM10 in general.

The evolution of the 'calcium' class particle concentration (red line) is similar to that of the 'aluminium' class particles. After a strong decrease in particle numbers from 10 m to 36 m, the curve gets considerably flatter from

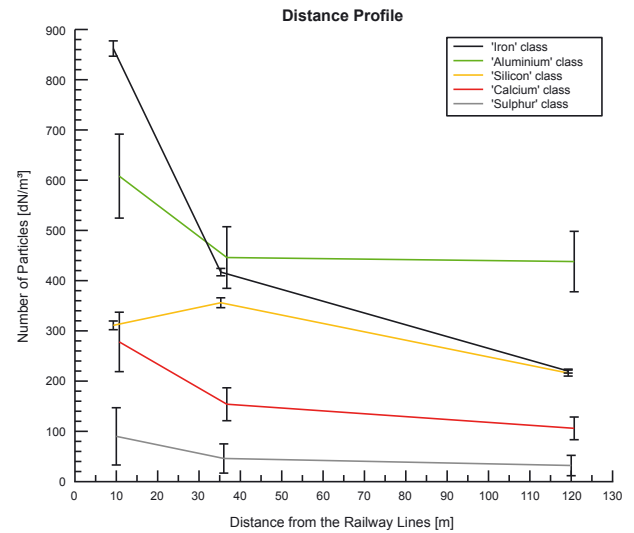


Fig. 2.3: Distance profile for the five particle classes. The error bars (two sigma) are calculated from the standard deviation of the three sampling sites at 10m distance from the railway lines. The values at 10m are average values from the three sampling sites at that distance. For better readability of the figure some plots are slightly shifted horizontally to prevent overlapping of data points and error bars.

36 m to 120 m. Thus, railway traffic is also a source for particles of the 'calcium' class.

A different behaviour can be observed for the change in particle number of 'silicon' particles (quartz) (yellow line) with increasing distance to the railway lines. The highest particle number is observed at 36 m and declines towards both sides (10 m and 120 m). This indicates an additional source located between the 10 m and the 36 m sampling site. Because the number concentrations of quartz particles are higher at 10 m than at 120 m and the sampling devices were only operated while the wind was blowing from the railway lines, it can be concluded that the railway's gravel bed, which contains granitoid rocks, is a source for the 'silicon' class particles. A second source is most likely a heap of quartz sand located at about 20 m distance from the railway lines, between the 10 m and 36 m sampling site. This sand is used on the nearby football grounds to reduce the formation of water pools after heavy rainfalls.

The number concentration of 'sulphur' particles (grey line) does not change with increasing distance from the railway lines. This indicates that the measured 'sulphur' particles are not related to the railway traffic but rather represent a background concentration. This agrees well with our previous assignment of the 'sulphur' class particles to combustion sources based on morphological criteria. It should be noted that the trains at the investigated site were exclusively electricity powered.

3.3 Mass calculations

The total mass of each particle class was calculated based on the individual particle morphology and the density of the respective classes which corresponded to the densities of the minerals listed in Table 2.3. The projected area of the particles is calculated by pixel counting (A_i [μm^2], i being the particle identification index). A second parameter which is directly derived from the particle image is the length of the longest particle axis (L_i [μm]) (see Figure 2.4 for details). Both parameters are determined by the particle analysis software.

Table 2.3
Densities used for the calculation of the mass contributions of the particle classes.

Densities (Particle Classes)	
Class	Density [g cm^{-3}]
Iron	5.5
Aluminium	2.6
Silicon	2.7
Calcium	2.35
Sulphur	1.3

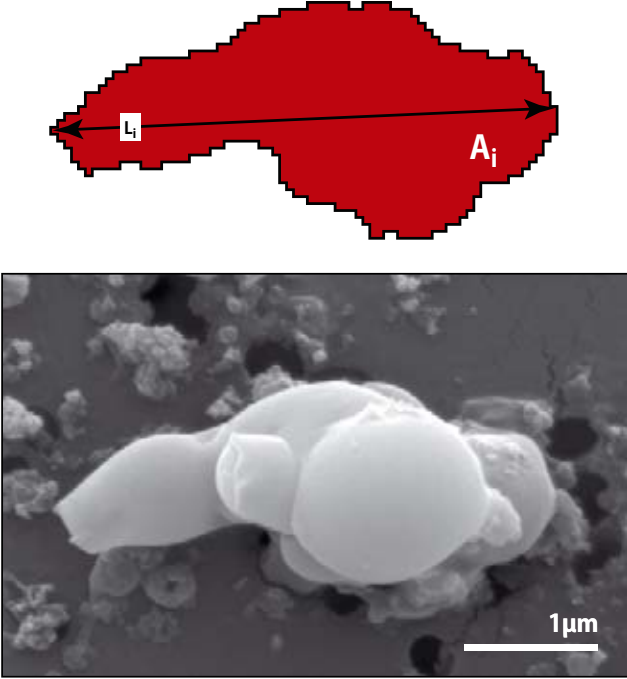


Fig. 2.4: Illustration of morphological parameters of the particles as determined by the particle software. A_i : optical projected area (determined by pixel count); L_i : longest particle axis (determined by pixel count).

Since most particles are not spherical, their volumes were approximated by prolate ellipsoids ($V_{E,i}$), according to (2).

$$V_{E,i} = \frac{4}{3} A_i^2 \frac{2}{L_i \pi} \quad (2)$$

Calculations were, therefore, based on directly measured parameters. It can be assumed that the particles will lie on their largest side rather than on the tip. Thus, cigars – prolate ellipsoids – are better approximations for cylindrical or cube like objects than spheres or oblate ellipsoids.

To determine the contribution of each class to the mass of PM10 (dM_{class}) equation 3 was applied with i spanning over all particles present in a specific class, ρ_{class} being the density for each class as listed in Table 2.3 and dV_{air} the total volume of air sampled.

$$dM_{class} = \frac{\sum_i V_{E,i} \rho_{class}}{dV_{air}} \quad (3)$$

In addition to the total mass of the particle classes, size resolved mass plots for each class were calculated. The volume of the prolate ellipsoid ($V_{E,i}$) was used to calculate equivalent spherical volume diameters (D_i) according to (4) and the equivalent aerodynamic diameters of the particles ($D_{i,air}$) according to (5) (Baron and Willeke 2001).

$$D_i = \sqrt[3]{\frac{6V_{E,i}}{\pi}} \quad (4)$$

$$D_{i,air} = D_i \sqrt{\rho_{class}} \quad (5)$$

This results in size resolved mass distributions of the different particle classes. Particle classes were arranged in 32 size bins – based on D_i – covering the range from 0.5 μm to 10.1 μm , the bin size being 0.3 μm . The resulting particle size distributions were then fitted with exponential functions (f_{class} , the R^2 values for the fits are all better than 0.9. The fits were used for illustration only; mass calculations were performed with the measured values).

3.4 Estimation of the railway contribution to local PM10 concentrations

Figure 2.5 shows the particle mass distribution at 10 m distance from the railway lines, calculated according to the method described above. Since ‘sulphur’ particles are not related to the railway lines, this class has been omitted in Fig. 2.5 and will not be considered in the further discussion.

The plots for the ‘iron’, ‘aluminium’ and ‘calcium’ class have their maximum between 2.5 μm and 4 μm (equivalent aerodynamic diameter) and contribute therefore mostly to the coarse mode. The ‘silicon’ class contributes almost exclusively to PM2.5, 80% of the quartz particles are smaller than 1.6 μm equivalent aerodynamic diameter.

To quantify the influence of the railway line on the local concentrations, it was assumed that the sampling site at 120 m distance represents the background concentration (meaning not influenced by the railway lines). This is supported by the fact that the particle number concentration at 120 m is only slightly smaller than at 36 m for all particle classes, except for the ‘iron’ class (see Figure 2.3). The concentration of ‘iron’ particles continues to decrease between the 36 m and the 120 m site, which indicates that background concentrations are probably not reached, yet, and, thus, our calculated mass contribution represents a lower limit for the emission of ‘iron’ particles. Figure 2.6 shows the difference of the mass distribution between 10 m and 120 m. The data points for quartz particles between 2.5 μm and 6.5 μm equivalent aerodynamic diameter are negative and therefore not shown on the plot.

As discussed before, there is a heap of quartz sand serving as a second source for quartz particles between 10 m

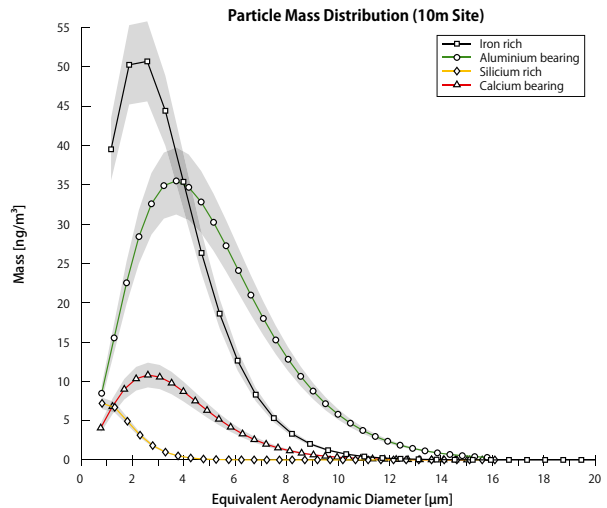


Fig. 2.5: Size resolved mass contributions of the particle classes for the sampling sites at 10 m distance from the railway lines. The error margins are represented by the grey areas.

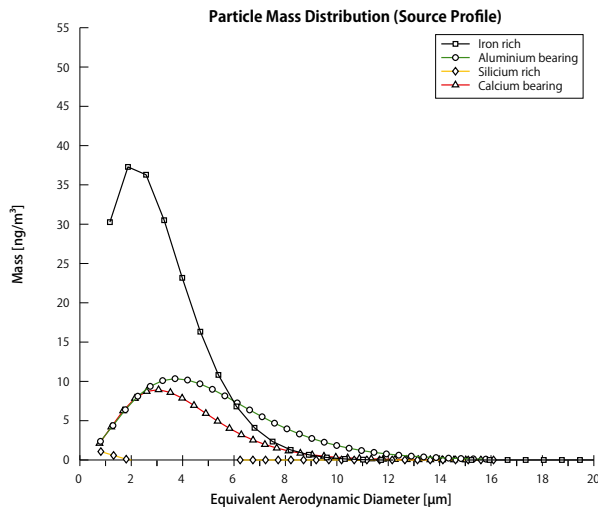


Fig. 2.6: Size resolved mass contribution of the particle classes resulting from the emissions of the railway lines at the 10 m site (difference between 10 m and 120 m sampling site).

and 36 m from the railway lines. The size distribution of particles resulting from this second source (quartz sand) is shifted towards coarser particles compared to the size distribution observed at 10 m distance, which explains the negative values. However, as can be seen on Figure 2.5, the contribution of quartz particles to the total PM₁₀ (railway related) is only of minor importance.

In Table 2.4 the mass and number concentrations of the major particle classes at the 10 m site and the 120 m site (assumed background) are given. The dominating particle class at 10 m is the 'iron' class with $3.9 \mu\text{g m}^{-3}$ followed by the 'aluminium' class with $2.4 \mu\text{g m}^{-3}$ and the 'calcium' class with $0.6 \mu\text{g m}^{-3}$. The source strength of the railway lines was calculated as the difference between the 10 m and the 120 m site. 'Iron' particles dominated the contribution to the additional PM₁₀ near railway lines ($2.9 \mu\text{g m}^{-3}$). Due to the high background concentration of 'aluminium' particles ($1.5 \mu\text{g m}^{-3}$) the contribution of the railway traffic to this class was only $1 \mu\text{g m}^{-3}$. There was light snowfall the week before the campaign and temperatures were often below freezing. The rather high background for 'aluminium' particles may therefore be explained by additional emissions caused by traction sanding on public roads, which leads to increased pavement wear (Kupiainen *et al.* 2005). The source strength for 'calcium' particles was $0.4 \mu\text{g m}^{-3}$.

Gehrig *et al.* (2007) performed an extended study between August 2003 and August 2004 at the same sampling site, using gravimetric methods and bulk chemical analysis with the goal to quantify long term average contributions of the railway to local PM₁₀ concentrations. Since they sampled continuously at all wind conditions and the sampling sites were exposed to winds from the railway sector only at about 50% of the time, their results are not directly comparable to those of our study. However, general trends should still be comparable.

As a reference for background concentrations of PM₁₀ Gehrig *et al.* (2007) used an urban background site in downtown Zurich, well separated from the railway lines. Based on the chemical analysis of the gravimetric samples at the 10 m site at Juchhof and the background station, they estimated the railway lines' contribution of iron (calculated as elemental Fe) to local PM₁₀ to be in the order of $1.0 \mu\text{g m}^{-3}$. According to this study, the mass of elemental iron in PM₁₀ generated by railway traffic is $2.0 \mu\text{g m}^{-3}$ (calculated as the difference between the 10 m and the 120 m sampling site at Juchhof). By applying the background concentration of elemental iron as determined by Gehrig *et al.* to our values of the 10 m site, the mass of elemental iron in PM₁₀ generated by railway traffic totals in $2.1 \mu\text{g m}^{-3}$. Therefore, the error caused by our assumption that the 120 m sampling site represents the local background for PM₁₀, is in the order of 10%. Considering that we measured exclusively during a period of direct wind influence from the railway, results from both studies are in excellent agreement.

4. Conclusions

In this study the method of detailed single particle analysis was used to characterize particulate emissions from a railway line. Five particle classes - 'iron', 'aluminium', 'silicon', 'calcium' and 'sulphur' - were distinguished. The 'iron' class particles were appointed to the wear of tracks, as well as wheels and breaks of the trains. Most of the 'aluminium' class particles are of geological origin (feldspar or clay minerals). The gravel bed of the railway lines is most likely the source for the elevated number concentration of 'aluminium' class particles close to the railway lines. Two different sources contribute to the 'silicon' - quartz - particles. The gravel bed of the railway lines and a heap of quartz sand located between the 10 m and 36 m sampling site. The 'calcium' class particles consisted mostly of calcium sulphate originating from re-suspension

Table 2.4

Calculated mass contributions of the three railway related particle classes. Particles were approximated as prolate ellipsoids with the long axis being L_i and projected area A_i (see Fig. 4 for details).

Calculated Weight (by Particle Class)		10 m (Average)		120 m (Background)		Source strength
Class	Minerals	Particles [#]	Mass [ng m ⁻³]	Particles [#]	Mass [ng m ⁻³]	Mass [ng m ⁻³]
Iron	Fe ₂ O ₃	862	3858.7	220	950.9	2907.8
Aluminium	Total	608	2442.9	438	1455.7	987.2
	(Na,K)AlSi ₃ O ₈	558	-	406	-	-
	CaAl ₂ Si ₂ O ₈	35	-	20	-	-
	Al ₂ O ₃	15	-	12	-	-
Calcium	Total	278	648.1	106	208.9	439.2
	CaSO ₄	263	-	101	-	-
	CaCO ₃	15	-	5	-	-
Total						
			6949.7		2615.5	4334.2

of mineral dust. The 'sulphur' class particles, assigned to vehicular exhausts, were of minor importance and were at background concentrations at all three sampling sites.

The detailed information on morphology and chemical composition of the particles obtained by CCSEM was used to quantify the railway induced particle concentrations of the railway lines. It has been shown that the 'iron' class particles contribute most to the railway related PM10 ($2.9 \mu\text{g m}^{-3}$), followed by the particles of the 'aluminium' ($1.0 \mu\text{g m}^{-3}$) and the 'calcium' ($0.4 \mu\text{g m}^{-3}$) class. The particles of the 'silicon' and 'sulphur' class are of minor importance. Results from CCSEM analysis are in good agreement

with gravimetric measurements of samples collected at the same sampling site in another study (Gehrig *et al.* 2007).

In the current study it was demonstrated that the automated analysis of small portions of filters by CCSEM combined with thorough data processing can produce results that are comparable with gravimetric methods. The results demonstrate that detailed single particle analysis not only provides comprehensive data of individual particles (morphology and chemistry) but can be used for a size, mass and chemistry resolved description of aerosols as well.

References

- Aarnio, P., Yli-Tuomi, T., Kousa, A., Mäkelä, T., Hirsikko, A., Hämeri, K., Räisänen, M., Hillamo, R., Koskentalo, T. and Jantunen, M. (2005). The concentrations and composition of and exposure to fine particles (PM_{2.5}) in the Helsinki subway system. *Atmos. Environ.* 39:5059-5066.
- Adams, H. S., Nieuwenhuijsen, M. J. and Colville, R. N. (2001). Determinants of fine particle (PM_{2.5}) personal exposure levels in transport microenvironments, London, UK. *Atmos. Environ.* 35:4557-4566.
- Baron, P. A. and Willeke, K., eds. (2001). *Aerosol Measurements: Principals, Techniques, and Applications*. John Wiley & Sons, New York.
- Birenzvige, A., Eversole, J., Seaver, M., Francesconi, S., Valdes, E. and Kulaga, H. (2003). Aerosol characteristics in a subway environment. *Aerosol Science And Technology* 37:210-220.
- Buseck, P. R., Jacob, D. J., Posfai, M., Li, J. and Anderson, J. R. (2000). Minerals in the air: An environmental perspective. *Int. Geol. Rev.* 42:577-593.
- Chen, Y. Z., Shah, N., Huggins, F. E. and Huffman, G. P. (2005). Transmission electron microscopy investigation of ultrafine coal fly ash particles. *Environ. Sci. Technol.* 39:1144-1151.
- Chillrud, S. N., Epstein, D., Ross, J. M., Sax, S. N., Pederson, D., Spengler, J. D. and Kinney, P. L. (2004). Elevated airborne exposures of teenagers to manganese, chromium, and iron from steel dust and New York City's subway system. *Environ. Sci. Technol.* 38:732-737.
- Gehrig, R., Hill, M., Lienemann, P., Zwicky, C. N., Bukowiecki, N., Weingartner, E., Baltensperger, U. and Buchmann, B. (2007). Railway traffic – a source of fine particles? Contribution of railway traffic to local PM₁₀ concentrations in Switzerland. *Atmos. Environ.* 41:923-933.
- Harrison, R. M. and Yin, J. X. (2000). Particulate matter in the atmosphere: which particle properties are important for its effects on health? *Sci. Total Environ.* 249:85-101.
- Johansson, C. and Johansson, P. A. (2003). Particulate matter in the underground of Stockholm. *Atmos. Environ.* 37:3-9.
- Katrinak, K. A., Anderson, J. R. and Buseck, P. R. (1995). Individual Particle Types In The Aerosol Of Phoenix, Arizona. *Environ. Sci. Technol.* 29:321-329.
- Kupiainen, K. J., Tervahattu, H., Raisanen, M., Makela, T., Aurela, M. and Hillamo, R. (2005). Size and composition of airborne particles from pavement wear, tires, and traction sanding. *Environ. Sci. Technol.* 39:699-706.
- Li, J., Anderson, J. R. and Buseck, P. R. (2003a). TEM study of aerosol particles from clean and polluted marine boundary layers over the North Atlantic. *J. Geophys. Res.-Atmos.* 108.
- Li, J., Posfai, M., Hobbs, P. V. and Buseck, P. R. (2003b). Individual aerosol particles from biomass burning in southern Africa: 2, Compositions and aging of inorganic particles. *J. Geophys. Res.-Atmos.* 108.
- Oberdorster, G. (1995). Lung Particle Overload - Implications for Occupational Exposures to Particles. *Regul. Toxicol. Pharmacol.* 21:123-135.
- Oberdorster, G., Gelein, R. M., Ferin, J. and Weiss, B. (1995). Association of Particulate Air-Pollution and Acute Mortality - Involvement of Ultrafine Particles. *Inhal. Toxicol.* 7:111-124.
- Paoletti, L., Diociaiuti, M., De Berardis, B., Santucci, S., Lozzi, L. and Picozzi, P. (1999). Characterisation of aerosol individual particles in a controlled underground area. *Atmos. Environ.* 33:3603-3611.
- Pfeifer, G. D., Harrison, R. M. and Lynam, D. R. (1999). Personal exposures to airborne metals in London taxi drivers and office workers in 1995 and 1996. *Sci. Total Environ.* 235:253-260.
- Pope, C. A. (2000). Review: Epidemiological Basis for Particulate Air Pollution Health Standards. *Aerosol Science and Technology* 32:4-14.
- Posfai, M., Simonics, R., Li, J., Hobbs, P. V. and Buseck, P. R. (2003). Individual aerosol particles from biomass burning in southern Africa: 1. Compositions and size distributions of carbonaceous particles. *J. Geophys. Res.-Atmos.* 108.
- Rosenbohm, E., Vogt, R., Scheer, V., Nielsen, O. J., Dreiseidler, A., Baumbach, G., Imhof, D., Baltensperger, U., Fuchs, J. and Jaeschke, W. (2005). Particulate size distributions and mass measured at a motorway during the BAB II campaign. *Atmos. Environ.* 39:5696-5709.
- Sharan, M., Singh, M. P. and Yadav, A. K. (1996). Mathematical model for atmospheric dispersion in low winds with eddy diffusivities as linear functions of downwind distance. *Atmos. Environ.* 30:1137-1145.
- Sitzmann, B., Kendall, M., Watt, J. and Williams, I. (1999). Characterisation of airborne particles in London by computer-controlled scanning electron microscopy. *Sci. Total Environ.* 241:63-73.
- VanBorm, W. A. and Adams, F. C. (1988). Cluster-Analysis Of Electron-Microprobe Analysis Data Of Individual Particles For Source Apportionment Of Air Particulate Matter. *Atmos. Environ.* 22:2297-2307.
- VanMalderen, H., VanGrieken, R., Bufetov, N. V. and Koutzenogii, K. P. (1996a). Chemical characterization of individual aerosol particles in central Siberia. *Environ. Sci. Technol.* 30:312-321.
- VanMalderen, H., VanGrieken, R., Khodzher, T., Obolkin, V. and Potemkin, V. (1996b). Composition of individual aerosol particles above Lake Baikal, Siberia. *Atmos. Environ.* 30:1453-1465.
- Xhoffer, C., Bernard, P., VanGrieken, R. and Vanderauwera, L. (1991). Chemical Characterization And Source Apportionment Of Individual Aerosol-Particles Over The North-Sea And The English-Channel Using Multivariate Techniques. *Environ. Sci. Technol.* 25:1470-1478.

2.3 Technical details

2.3.1 Instrumentation

Standard filter holders for PM10 sampling devices are built similar to the one shown in Figure 2.7. They have a simple design and are easy to handle, but they suffer from inhomogeneous particle load. Small particles follow the air flow better than large ones do. Accordingly, the widening of the air flow in front of the filter leads to a concentration of large particles in the centre of the flow while small particles are evenly distributed throughout the cross section of the flow. However, to be able to extract accurate chemistry resolved particle size distributions of the sampled aerosol, based exclusively on single particle analysis, homogeneous particle deposition on the filters is a prerequisite *sine qua non*.

Sampling device

New filter holders had to be designed to resolve the problem of size fractionation. Two solutions were taken into consideration: Either the necessary increase in tube diameter has to be spread over a long distance (effectively making it a cone) or the increase had to be avoided completely (cylinder). The solutions correspond to a replacement of the tube connecting the impactor with the filter holder unit by a cone with one end diameter corresponding to the filter diameter, or to replace it with a tube with approximately the same diameter as the filter.

The filter area needed for microscopic analysis is a few square millimetres at most. Therefore, small Nuclepore® filters with 2.5 cm diameter would provide enough area for a representative analysis. Thus, the inner diameter of the connection between impactor and filter holder had to be <2.5 cm at the wider end.

The impactors to be used were manufactured by MSP Corporation (personal environmental monitor, model 200) and the inner diameter of their impaction plates is 1.6 cm. A usable filter area with that diameter would still suffice for the analysis planned. Thus, the more practical approach was to use a cylindrical connection tube with the same inner diameter as the impactor plate (1.6 cm). The final assembly has been designed by L. Emmenegger (Fig. 2.8).

For the design of the pump assembly three parameters were decisive: Since the pumps were also used outdoors they have to be water proofed, the flow through the sampling device has to be constant (4 l min^{-1} , flow rate required by the impactor) and independent of filter load and the pump's performance has to be indifferent to long operation times and short on-off-on sequences.

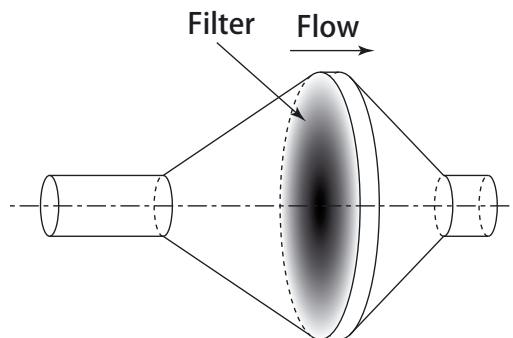


Fig. 2.7: Schematic of a standard filter holder. The cross section of the air flow is widened in front of the filter. As a consequence, filter load is not homogeneous across the filter surface.

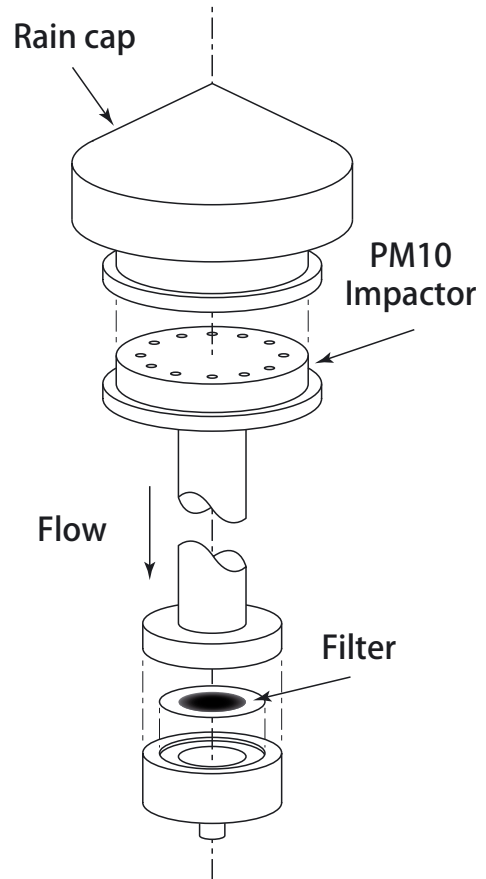


Fig. 2.8: Schematic of the filter holder / impactor assembly constructed for the railway study. The cross section of the air flow remains constant from the beginning of the tube (after the impactor) down to the filter.

Rather than looking for a commercial setup with a regulated pump, the less costly approach of a custom (self) built assembly was chosen (Fig. 2.9). As basis served a robust and high powered vacuum pump (KNF membrane pump, model N 828 KNE). To regulate the flow rate without electronics, a critical orifice with a diameter of 0.72 mm was integrated into the Swagelok® fitting at the inlet of the pump. To be able to verify the flow rate during operation, a rotameter (Vögtlin V100) was integrated into the water proofed plastic casing (Utz Poolbox) on the outlet of the pump. While the critical orifice ensures a constant air flow on the inlet side, the membrane mechanism produces a pulsing flow on the outlet side. Thus, a compensating reservoir (a finger of a rubber glove and a Y-shaped flow splitter) had to be inserted in front of the rotameter.

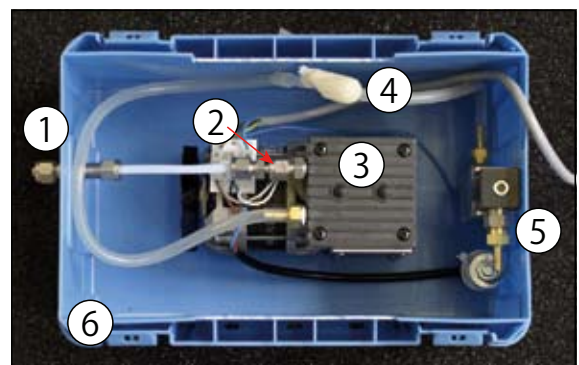


Fig. 2.9: Top view of the pump assembly of the PM10 samplers. (1) inlet, (2) critical orifice, (3) vacuum pump, (4) compensating reservoir, (5) rotameter, (6) water proofed housing (lid removed).

Control unit

The control unit for the sampling devices was built around a commercially available meteo station (Schiltknecht). For the study planned it was imperative to be able to sample as a function of wind direction i.e. to sample only air masses which came from the railway lines. Additionally, the wind speed was included into the control parameters. Because at very low wind speeds the vane will not adapt to the wind direction reliably a lower threshold of 0.4 m s^{-1} was set. At high wind speeds, dilution of the emission is very strong and, thus, representative sampling is not ensured any more. Accordingly, the upper threshold was set at 10 m s^{-1} .

Railroad traffic is strongly reduced between 01:00 and 05:00. Operation of the sampling devices during this time period would not significantly contribute to the particle load of the filters but would considerably increase the recording time. Sampling intervals during this virtually emission free time period would distort the resulting emission factors and were excluded from the allowed operation times.

The last parameter included in the control algorithm (Fig. 2.10) was the total operation time of the sampling devices. All parameters are continually logged for a subsequent assessment of the samples' quality.

2.3.2 Railway study

During the preliminary tests an overall sampling time of eight hours was determined to deliver an ideal filter load for the analysis by computer controlled scanning electron microscopy (CCSEM). This, however, was for sampling without taking the wind parameters into account. Records of wind direction and speed of the study area suggested that about 50% of the overall time the wind was blowing from allowed directions (see Table 2.1). This reduced the absolute sampling time needed to four hours.

In normal conditions one to two days would suffice to get the set collection time. However, during the measurement campaign stable high pressure conditions prevailed and the winds were blowing preferably from the east, along the railway tracks, and from northeast (Fig. 2.11). As a consequence, it took four days to get the four hours of favourable conditions needed.

Analysis

The filters collected during the on-site preliminary tests were investigated in order to check the homogeneity of the particle deposition. To make sure that the choice of sampling parameters is not biasing the data, samples from different sampling locations and with different collection times were compared.

Parameters for the CCSEM analysis were as listed in Table 2.2. Since the only information needed to perform the bias test was on the particle morphology, no EDX analyses were performed. Nevertheless, filters were not coated to ensure identical conditions as planned for the final analysis.

Five sampling fields (approx. 0.08 mm^2 each) on each filter were randomly selected for analysis. To ensure that the chosen fields are representative for the whole sample, boundary conditions for the coordinates of the individual fields were set (Fig. 2.12). To facilitate the process, polar coordinates were used. The boundary conditions were related to two different divisions of the sample: the whole

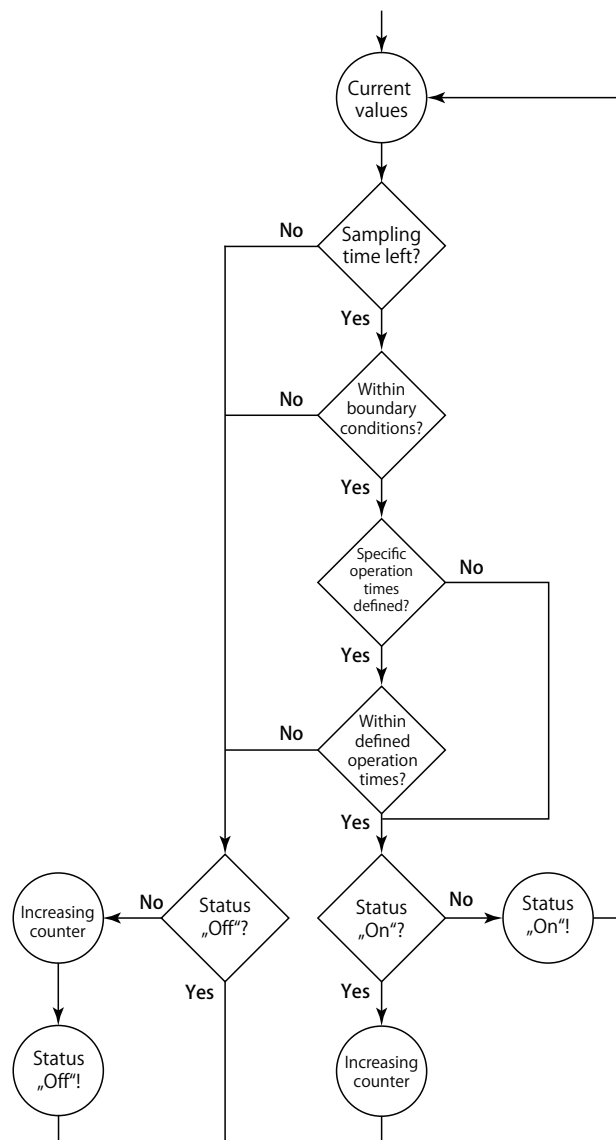


Fig. 2.10: Flow chart of the algorithm used to control the sampling devices. The input data are delivered by the meteo station.

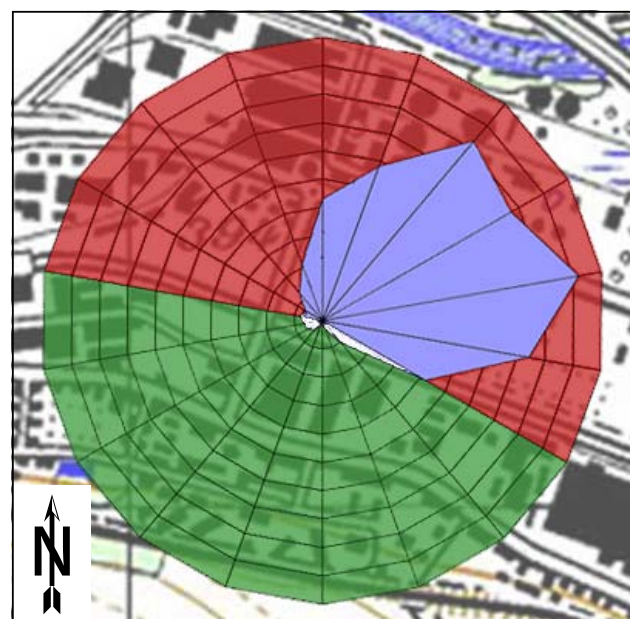


Fig. 2.11: Summary of wind directions recorded during the collection of the samples for the railway study. Green: allowed directions. Purple & white: directions registered, purple from the red sector and white from the green sector (the larger the radius, the more frequent the direction).

filter was divided by radial lines into five sectors each spanning 72° and by circles into five rings. The position of the first sector boundary was chosen randomly and the radii were chosen such that the resulting rings have equal area. The maximum radius was limited to 7 mm, excluding a zone 1 mm in width along the sample rim. This was necessary to ensure that the sampling fields did not cross the sample boundary.

The upper left corner given in polar coordinates (radius, azimuth) were determined by a random processor. The individual values were only accepted when none of the upper left corners of the previously selected fields were located in the same ring or the same sector. Azimuths were assigned to the radii in the order of their generation. Thus, no particular order would be favoured.

The transformed coordinates served as upper left corner for areas to be analysed (stubs). The software used for the analysis (EDAX Inc., Genesis) divided the fields into five columns with five images each, totalling in 125 images per filter.

Particle numbers in different fields of the same filter were not quite as homogeneous as hoped but relative standard deviations stayed within 10%. No size fractionation could be detected. Nevertheless, the field selection procedure for the fields was kept unchanged to stay on the safe side.

For the evaluation of the EDX spectra of the samples, background counts for the elements considered were determined for each filter separately. After initial values were set on the basis of the single particle spectra, sensibility tests were performed by varying background levels and monitoring the changes of the particle counts of the six

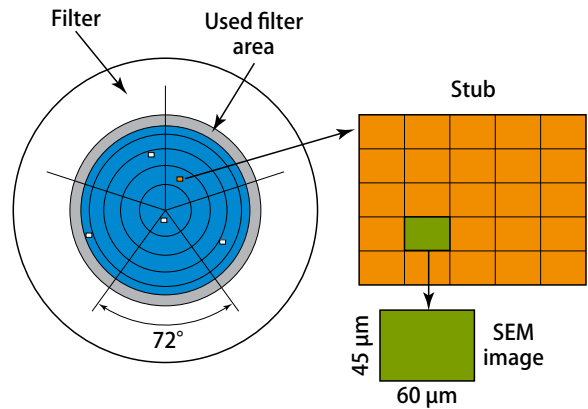


Fig. 2.12: Schematic of the areas of a filter used for analysis. Particles are deposited in the grey and blue concentric circles but only the blue ones (all of equal area) are considered.

classes. For a correct setting slight variations should only have a negligible impact on particle counts.

The Matlab routine programmed for the evaluation of the EDX data is structured in two blocks (see Appendix A.2.1). The first block (sbb.m) sets the boundary conditions for the analysis of the EDX data, executes the programs of the second block, normalises their output and calculates error margins. The second block (sbb_XX_El.m) consists of five programs, one for each filter. They normalise the EDX spectra, sort the particles according to the algorithm shown in Figure 2.2, calculate individual particle masses, build histograms and compile summaries.

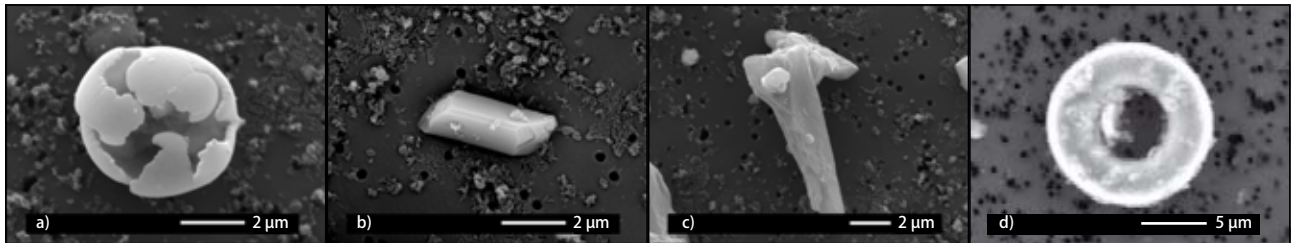


Fig. 2.13: Example SEM images taken from the filters of the preliminary tests. a: Iron particle; b: Particle of the calcium class; c: Quartz particle; d: A fairly unusual quartz ring. The filter used for images a, b and c was platinum coated for better image quality and the filter harbouring the quartz ring (d) was left uncoated.

Thermophoretic Sampling Device

- Introduction
- Publication
- Technical Details

«It had the virtue of never having been tried.»

Kirk, Star Trek II

3 Thermophoretic Sampling Device

3.1 Introduction

3.1.1 Thermophoresis

A thermal gradient in a gaseous or liquid fluid will cause a net force on suspended particles. Molecules from the warmer side of the gradient carry more energy than their counterparts from the cooler side and, therefore, may transmit more energy to a particle during collision. Thus, suspended particles get gradually pushed towards the cooler side (Fig. 3.1). This process has long been known and its strength was first estimated by Einstein (1924). A more thorough investigation of the forces acting on small particles suspended in inhomogeneous fluids has later been performed by Waldmann (1959). In his work he calculates the thermophoretic settling speed (v_t) with which a suspended particle passing through a temperature gradient moves towards the cold side to (1).

$$v_t \approx -\frac{1}{5 \cdot \left(1 + \frac{1}{8} \pi a\right)} \cdot \nabla T \cdot \frac{K}{p} \quad a \in [0..1] \quad (1)$$

The settling speed is influenced by the temperature gradient ∇T , the thermal conductivity K and the pressure p of the carrier gas, as well as the molecular accommodation coefficient a .

The parameter a gives a measure for the fraction of impinging molecules that undergo diffusive reflection and, accordingly, $(1-a)$ gives a measure for elastic reflection. In normal (meaning: most) conditions it can be expected that interactions of molecules and particles are in the majority of cases elastic and, thus, it is justified to assume that $a=0$, resulting in (2).

$$v_t = \frac{1}{5} \nabla T \frac{K}{p} \quad (2)$$

Thermophoresis is a very weak effect. For a temperature gradient of 10^6 K m^{-1} v_t is only $\sim 2.5 \text{ cm s}^{-1}$ (in air). Nevertheless, thermophoresis lends itself to representative particle sampling because v_t is independent of particle composition. Additionally, equations (1) & (2) suggest independence of particle size as well. This is true as long as particles move freely and unobstructed through the fluid. Therefore, above equations are limited to the free molecular regime (Knudsen number $Kn > 1$). However, experiments show that the size dependence for particles in the transition regime is negligible up to $\sim 300 \text{ nm}$ (e.g. Messerer 2003).

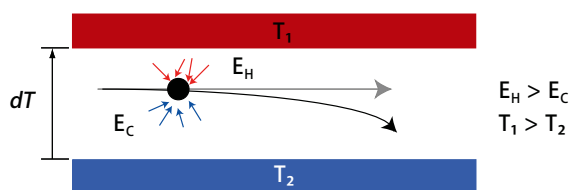


Fig. 3.1: Particles passing through a temperature gradient get gradually deflected towards the colder side. E_H , E_C : kinetic energy of the molecules impinging on the particle. Gray arrow: flight path of the particle without temperature gradient; black arrow: with temperature gradient (dT) present.

The use of thermophoresis for particle sampling is straightforward. Two basic designs have prevailed (Fig. 3.2): the wire-to-plate (a) and the plate-to-plate (b) configurations. In either type the substrate is placed on the cooled plate (collection surface). While thermophoretic sampling devices (TPS) for coarse particles have long been around their potential for the specific collection of ultrafine particles has not been tapped until lately (Maynard 1995). The need for specialized sampling devices is evident when considering the risk of altering particles and introducing artefacts in the process of sample preparation (Berube *et al.* 2004).

3.1.2 Advantages of thermophoretic sampling

Concerning the collection of ultrafine particles thermophoresis promotes itself through a number of points. Arguably the most important aspects are the - already mentioned - independence of particle size and composition. This facilitates sample analysis because no particle dependent effects have to be taken into consideration. Relations between particle classes that are observed on the substrates can be applied directly to the sampled air masses.

Similarly, the choice of sampling substrate is not limited to certain materials. Of course, preference should be given to substrates with constant thermal properties because this is a prerequisite for a homogeneous temperature gradient and, consequently, for reproducible sampling conditions. This being said, substrates can be chosen according to the needs of the analytical methods scheduled for sample analysis.

Due to the low thermophoretic settling speed long sampling times can be realized without the risk of overloading the substrates. Since the collection surface is cooled particles are conserved in their original state (given that condensing conditions are avoided). This is an advantage for exposure studies at working environments with (one) focus on the over all exposure. Samples collected with the TPS can represent an overview of the particle types an employee has been exposed to during a day's work. Hence, setting the exposure to work related ultrafine particles in relation to the "normal" every day particle load.

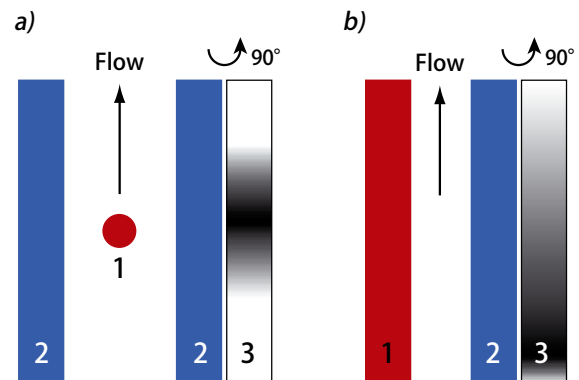


Fig. 3.2: Cross-sectional view of the most frequent designs for thermophoretic sampling devices. a: wire-to-plate; b: plate-to-plate. 1: heated wire/plate; 2: cooled plate; 3: schematic drawing of the deposition pattern on the cold plates (the darker an area the more particles get deposited)

3.1.3 Drawbacks and limitations

Due to the low thermophoretic settling speed flow conditions inside the sampling device are a major issue. Depending on sample flow speeds, the parabolic velocity profiles in the narrow channels can be very pronounced. For a low Mach number the aerosol density is uniform across the channel resulting in a particle flux similar to the velocity profile. Therefore, particle deposition cannot be uniform across the collection surface. However, by tweaking the geometry of the temperature field and the position of the substrate therein, the inhomogeneity can be used to maximize the deposition on the substrate.

The low deposition efficiency and the long sampling times are an advantage for situations with high aerosol concentrations where faster sampling techniques may not be appropriate. Thermophoretic sampling is also ideal to obtain long time average measurements, but is not adapted for spot testing.

3.1.4 Calibrated sampling devices

Sampling without calibration delivers information about the physicochemical properties of individual aerosol particles, but not about their relative abundance.

Quantitative analysis of aerosol samples based exclusively on single particle analysis is only possible if the sampling process is independent of particle properties, such as size, morphology, chemistry or density. No separation due to flow characteristics and particle interactions are allowed. If these requirements are not met the device cannot simply be calibrated for its collection efficiency but to compensate the interfering effects as well. For the calibration and simulation of thermophoretic devices deposition characteristics are an issue. While for wire-to-plate and plate-to-plate devices with rectangular plates only two dimensions have to be considered for the calibration procedure (perpendicular to the cold plate and along the flow, across the channel deposition rates are constant) for plate-to-plate devices with circular heating/cooling plates the problem remains three dimensional.

In either case, the calibration process is divided into two stages: modelling and verification. Ideally, the verification step includes control experiments to test the modelling results and to validate simplifying assumptions included in the model - such as the independence of the deposition efficiency from particle size. According to theory a deposition gradient has to be expected. Therefore, chords through the centre of the substrate have to be analysed to detect a possible dependence on the orientation of the substrate.

References

- Einstein, A. (1924). Theory of radiometer energy. *Z. Phys.* 27:1-6.
- Berube, K. A., Jones, T. P., Williamson, B. J., Winters, C., Morgan, A. J. and Richards, R. J. (1999). Physicochemical characterisation of diesel exhaust particles: Factors for assessing biological activity. *Atmos. Environ.* 33:1599-1614.
- Maynard, A. D. (1995). The Development of a New Thermophoretic Precipitator for Scanning-Transmission Electron-Microscope Analysis of Ultrafine Aerosol-Particles. *Aerosol Science and Technology* 23:521-533.
- Messerer, A., Niessner, R. and Poschl, U. (2003). Thermophoretic deposition of soot aerosol particles under experimental conditions relevant for modern diesel engine exhaust gas systems. *J. Aerosol. Sci.* 34:1009-1021.
- Waldmann, L. (1959). Über die Kraft eines inhomogenen Gases auf kleine suspendierte Kugeln. *Zeitschrift für Naturforschung Part A-Astrophysik Physik und Physikalische Chemie* 14:589-599.

A thermophoretic precipitator for the representative collection of atmospheric ultrafine particles for microscopic analysis

R. Lorenzo^{a,d}, R. Kaegi^b, R. Gehrig^a, L. Scherrer^c, B. Grob ty^d, H. Burtscher^e

^aEmpa, Materials Science & Technology, Laboratory for Air Pollution & Environmental Technology,  berlandstrasse 129, CH-8600 D bendorf, Switzerland

^bEawag, Swiss Federal Institute for Aquatic Science and Technology, Urban Water Management,  berlandstrasse 133, CH-8600 D bendorf, Switzerland

^cETH Z rich, Solid State Physics, CH-8093 Z rich, Switzerland

^dUniversity of Fribourg, Institute for Mineralogy and Petrography, Ch. du Musee 6, CH-1700 Fribourg, Switzerland

^eUniversity for Applied Sciences of Northwestern Switzerland, Institute for Aerosol and Sensor Technology, Klosterzelgstrasse, CH-5210 Windisch, Switzerland

Submitted 20 December 2006; received in revised form 26 March 2007; accepted 13 July 2007

Abstract

In this paper the potential of a thermophoretic sampling device to derive quantitative particle size distributions and number concentrations of aerosols based on microscopic single particle analysis is explored. For that purpose a plate-to-plate thermophoretic precipitator to collect ultrafine atmospheric particles for TEM (transmission electron microscopy) analysis has been calibrated and characterized. The representativeness of the samples has been verified in a series of experiments. Results show that, for particles with diameters of 15 nm to 300 nm, the precipitator's collection efficiency is independent of size, shape, and composition of the particles. Hence, its samples accurately represent the original aerosol.

A numerical model of thermophoretic deposition within the device has been developed and tailored to the specifications of the precipitator. The model has been used to derive the particle number density and size distribution of several calibration aerosols using the TEM analysis of the samples taken with the thermophoretic precipitator as input parameters. The results agree very well with the on-line measurements of the calibration aerosols. This work demonstrates that our thermophoretic sampling device can be used to derive quantitative particle size distributions and number concentrations of ultrafine particles based on microscopic single particle analysis.

  2007 American Association for Aerosol Research (AAAR)

Keywords: Atmospheric ultrafine particles; Quantitative Analysis; Thermophoresis; Nanoparticles; TEM;

1. Introduction

Ultrafine particles are one of the boon and bane of modern technology. On one hand, they play an important role in the development of nanotechnology; on the other hand, submicron particles originating from manufacturing and combustion processes significantly contribute to the pollution of the work place and ambient atmosphere. Several studies address the possible adverse health effects of nano-sized particles (Li *et al.* 2003; Oberdorster *et al.* 2004; Seaton and Donaldson 2005). However, the mechanisms responsible for these adverse effects are still poorly understood due to limited knowledge of the physical and chemical characteristics that are responsible for these effects, as Harrison and Yin (2000) point out highlighting the need for specialized sampling equipment.

Morphology, structure and composition of ultrafine aerosol particles (diameter smaller than 100 nm) are frequently analysed by means of transmission electron microscopy (TEM) (e.g. Mathis *et al.* 2004; Maynard *et al.* 2004; Chen *et al.* 2005; Ku and Maynard 2005). For this purpose, particles need to be deposited on TEM support grids. Representative and artefact free sampling of ultrafine particles is, however, by no means trivial. Preferably, particles are deposited directly from the atmosphere onto the support film of TEM grids, which reduces the risk of poten-

tial artefacts related to sample preparation (Berube *et al.* 1999).

The only viable deposition mechanisms for submicron particles are electrophoresis and thermophoresis, but only thermophoresis is virtually independent of particle size for particle diameters smaller than ~150 nm (Brock 1962). Electrophoresis can yield high sampling efficiencies, but the sampling substrata have to be electroconductive (Dixkens 1999). For thermophoresis, no such limitations apply, allowing the use of virtually any substrata that, thus, can be chosen according to analytical requirements.

A number of designs of thermophoretic samplers have been described in the literature (e.g., Mercer 1973). The two primary type are: (1) the hot-wire (e.g. Green and Watson 1935; Kasper 1982; Bang *et al.* 2003), and (2) plate-to-plate (e.g. Maynard 1995; Tsai and Lu 1995; Gonzalez *et al.* 2005) design.

Mercer (1973) points out that thermophoretic precipitation is prone to non-uniform particle deposition that depends on both size and deposition efficiency. However, Mercer focused mainly on coarse particles (> 0.5  m). For ultrafine particles size selectivity is expected to be rather small (Brock 1962). The non-uniform deposition efficiency (for ultrafine particles), on the other hand, is mainly due to

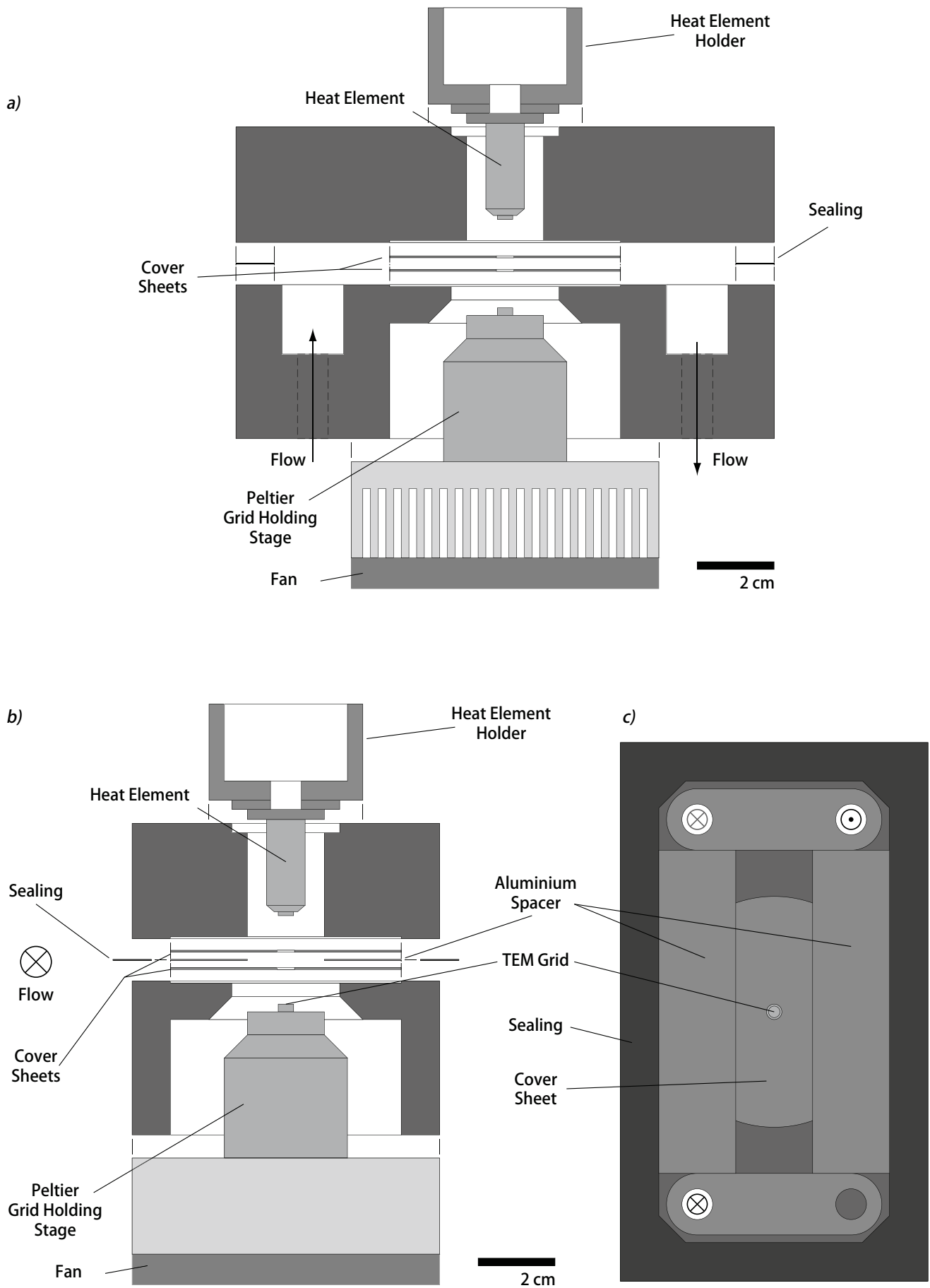


Fig. 3.3: Exploded schematic cross section of the precipitator. a: Along the centre of the precipitator, following the flow. b: Across the centre of the precipitator, perpendicular to the flow. c: Top view of the Peltier assembly with cover sheet, Al spacer and sealing.

fluid dynamics and non-ideal temperature fields and, therefore, cannot be avoided completely. For the quantitative evaluation (e.g., particle size distribution, number concentration) of thermophoretically collected aerosol samples by electron microscopy, it is imperative to be able to model (numerically) this non-uniformity. To our knowledge, no attempts have been made to date to calibrate sampling devices for ultrafine particles, or to calculate deposition patterns of such particles on TEM grids.

In this study a combination of a thermophoretic precipitator and a numerical model is described that allows the quantification of number concentrations and particle size distributions of ultrafine aerosols based exclusively on single particle analysis with electron microscopes.

2. Design

The most important element of the precipitator is the sampling channel (Fig. 3.3 & 3.4a). The width is 20 mm, and the length is 83 mm. The height can be adjusted using aluminium spacer sheets. For the present investigation, a channel height of 0.3 mm was chosen. The TEM grid is mounted in the middle of the floor of the sampling channel, using a weak cup magnet with 4 mm diameter which is flush with the channel base. To prevent the TEM grid from being lifted by the air flow, the magnet has a circular depression of 3.1 mm in diameter and of 0.1 mm in depth. To keep the TEM grid at a constant temperature, a Peltier element (thermoelectric cooler) (Rowe 2006) and a K-type thermocouple are incorporated into the grid holding stage directly below the magnet, as close to the TEM grid as possible. A heating element (4 mm in diameter) is placed in the middle, flush with the channel ceiling, and directly opposite to the sampling grid. To enable a stable temperature gradient the heating element is monitored with a K-type thermocouple and actively controlled.

Both the heating and the Peltier elements are built into cavities of the sampling device to minimize distortions of the temperature field. In order to produce a smooth channel, the cavities are covered by a thin circular aluminium sheet with a concentric hole of 4.1 mm in diameter. The tips of the heating and cooling elements are only 4 mm in diameter and fit into the holes of the cover sheets to level up with the channel.

Since the sampling device is designed to collect environmental particles, the temperature of the Peltier grid

holding stage is set to a standard temperature of 15°C to reduce the risk of condensation. To protect sensitive particles from damage, the standard temperature of the heating element is set to 135°C, resulting in a temperature gradient of $4 \cdot 10^5 \text{ K m}^{-1}$.

To keep particle losses due to diffusion in the sampling lines up to the precipitator low, high flow speeds are required. To add flexibility to the sampling parameters, separate regulation of the flow rate inside the lines up to the precipitator and the sampling channel is an advantage. Accordingly, after the sampling line enters the device, it provides two flow paths (Fig. 3.3 & 3.4b). Instead of forking the sampling line, the flow is led into a small chamber from which two exits exist. One leads to the sampling channel (having the same cross section) and the other is a bypass that goes directly to the pump. For standard operations, the flow rate in both the lines preceding the precipitator and in the sampling channel is set to 2 l min^{-1} . For aerosols with known size distributions or for measurements where information on the particle size distribution is of minor concern, the flow rate through the sampling channel can be reduced. Smaller flow rates do increase the sampling efficiency but at the cost of higher and size dependent losses. While the temperature gradient is being established, the flow through the sampling channel is stopped. Once the temperatures of the cooling and heating elements are stable, the sample flow is gradually diverted to the sampling channel according to the set flow speeds (keeping the total flow constant at 2 l min^{-1}).

The flexible structure of the sampling device presented in this study allows a variety of experimental setups. The sampler is controlled by a LabView® program that regulates and logs both the sample flow through the device and the temperature gradient, while still allowing manual corrections. The parameters are kept within 3% of the initially set points, even for long sampling runs (verified up to one week sampling time).

3. Numerical modelling of the deposition properties

Maynard (1995) used a thermophoretic precipitator to collect ultrafine particles, and observed a non-uniform particle deposition pattern on the TEM grids. To derive particle number concentrations from such samples, a quantitative understanding of the deposition pattern of the particles on the grids is required. To satisfy this need,

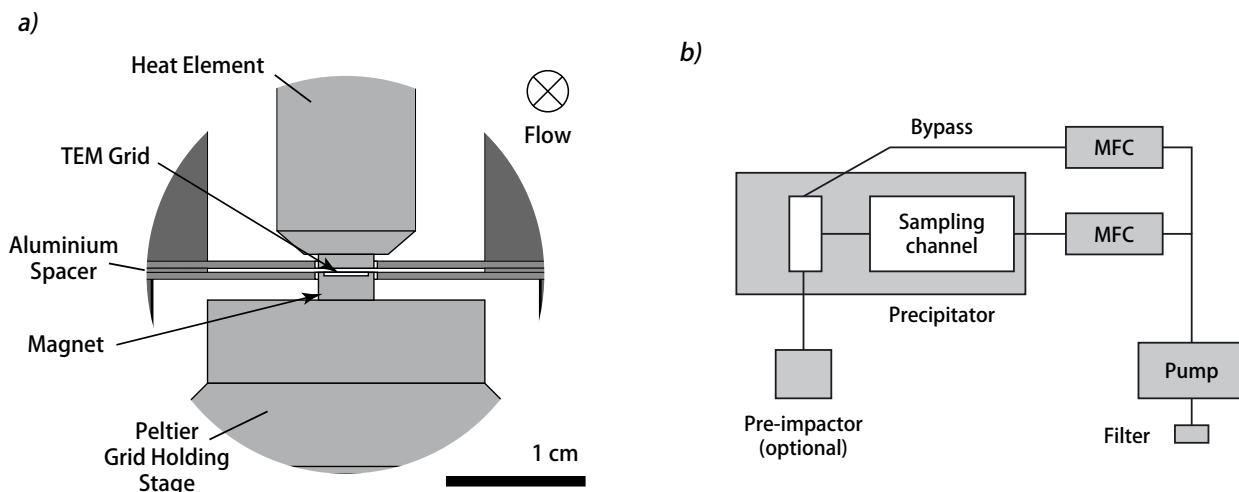


Fig. 3.4: Details of the precipitator's design. a: Enlargement of the sample channel. b: Schematic representation of the precipitator's periphery.

a model was developed to describe particle deposition on TEM grids. Because of the low Reynolds number of the present apparatus ($Re = 220$), the flow is expected to be laminar and incompressible (flow velocity in the channel at 2 l min^{-1} and standard temperature and pressure: $<10 \text{ m s}^{-1}$, Mach number <0.03). Therefore, a parabolic flow profile (Fig. 3.5a) can be assumed. To simplify the model a linear temperature gradient limited to the space between the cooling and heating elements are assumed, resulting in cylindrical boundary conditions for the effective temperature field.

The model calculates the trajectories of particles within the sample channel above the Peltier stage, and records their deposition positions. Diffusional losses between the leading and the trailing edges of the cooling and heating elements ($<0.01\%$) are neglected. The particles are released in a rectangular area perpendicular to the flow path (Fig. 3.5b). The starting coordinates for particles in the model are generated by a random function to produce a uniform distribution across the starting area. To account for the parabolic flow velocity profile that produces a non-uniform particle flow within the sample channel, each particle is weighted by a scaling factor scf (Eq. 1). The scf sets the starting parameters of the model particle in relation to the average flow speed and the channel height and is, therefore, a measure for the non-uniform particle flux through the sampling channel due to the flow profile. The scf is a function of the initial height of the particle above the bottom of the sampling channel z_0 , its initial velocity $v(z_0)$ – according Eq. (2) – the total flow through the sampling channel Q ($2000 \text{ cm}^3 \text{ min}^{-1}$), the width w_c (2 cm) and the total height h_c (0.03 cm) of the channel.

$$scf = \frac{v(z_0)z_0w_0}{Q} \quad (1)$$

The particle velocity $v(z)$ parallel to the sample flow, at any given point, is calculated according to Eq. (2) (Panton 2005).

$$v(z) = v_c \left[1 - \frac{(h_c - 2z)^2}{h_c^2} \right] \quad (2)$$

The maximum velocity in the sampling channel (v_c) is calculated by solving the integral from 0 to h_c of Eq. (2) for v_c which results in Eq. (3).

$$w_c \int_0^{h_c} v(z) dz = Q \Rightarrow v_c = \frac{3}{2} \frac{Q}{h_c w_c} \quad (3)$$

The vertical velocity of the particles is initially set to zero. Once they enter the temperature field it is set to the thermophoretic deposition velocity v_t , which is calculated according to Eq. (4) (Talbot 1980) with the thermal conductivity of the carrier gas K (for air: 0.024), its pressure p and the temperature gradient ∇T .

$$v_t = \frac{1}{5} \nabla T \frac{K}{p} \quad (4)$$

Since the thermophoretic migration velocity (1 cm s^{-1} at a gradient of $4 \cdot 10^5 \text{ K m}^{-1}$) is rather small compared to the flow velocity, only particles from a limited height (referred to as sampling height in the following) are collected (Fig. 3.5a). The resulting aerosol sample is still representative, because the flow inside the sampling channel is completely laminar and, therefore, particles are homogeneously distributed throughout the channel. Nevertheless, the sampling times required to obtain adequate coverage of the TEM grids are affected by the sampling height. Lower flow velocities and higher temperature gradients increase the sampling height, but at the cost of increased (and size selective) diffusion losses and the risk of damaging temperature sensitive particles. Moreover, for the device described, larger temperature gradients proved to be less stable (i.e. temperature variations at the heating and cooling elements of more than 3%).

The results of the model calculations shown in Figure 3.6, indicate that, on the trailing edge of the TEM grids, more particles are deposited than on the leading edge (for conditions where the height of the “collected layer” is less than, or equal to half the channel height). This is a consequence of the parabolic flow profile that produces an increasing particle flux towards the middle of the sampling channel. Because the thermophoretic migration velocity is constant, particles deposited at the trailing edge of the grid originate from higher above the base of the sampling channel and, therefore, from a region with higher particle flux than particles deposited at the leading edge. However, in the central section of the grid, which is used for TEM analysis, particle deposition is rather constant ($\pm 10\%$). Accordingly, the variation in particle deposition efficiency across the

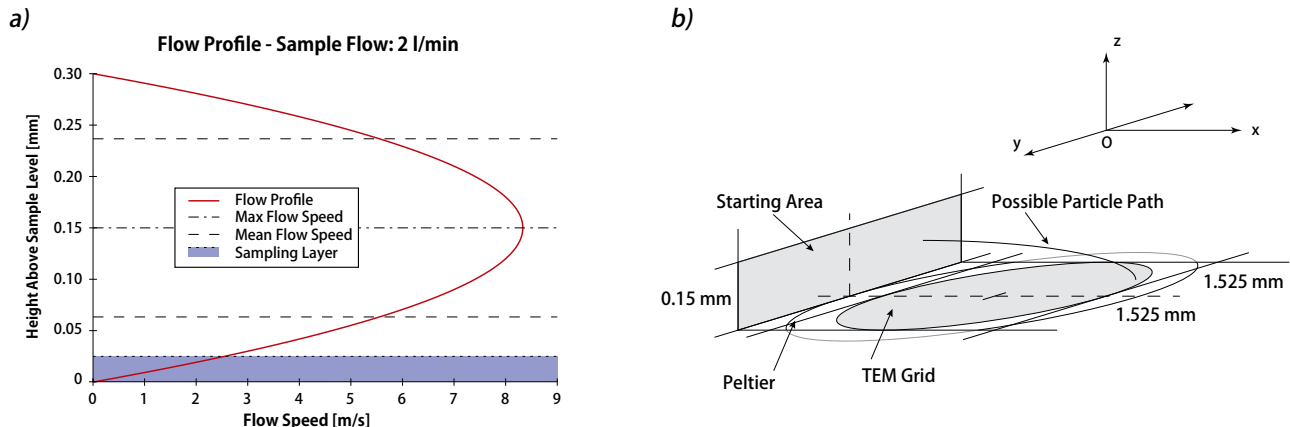


Fig. 3.5: Key elements of the numerical model. a: Parabolic flow profile inside the sampling channel. At flow speeds of 2 l min^{-1} and a temperature gradient of $4 \cdot 10^5 \text{ K m}^{-1}$ only particles from the grey area are sampled. b: Principle parameters of the model. Starting coordinates of the particles are randomly generated in the “starting area”.

central section gives an error margin for the results gained from the samples. Concerning diffusion losses up to the grid, for particle diameters >15 nm losses are <1% and are well covered by said error margin of ±10%.

According to the model, the following sampling times are required in order to get a sample suitable for TEM analysis

(0.5% coverage of the grid at 2 l min⁻¹ and 4·10⁵ K m⁻¹): 10 minutes at a heavily polluted working environment (5·10⁵ particles per cm³), 90 minutes at an urban background site (5·10⁴ ppcm³), and 1 day at a clean background site (3·10³ ppcm³). Therefore, the time resolution of the precipitator depends on the particle concentrations.

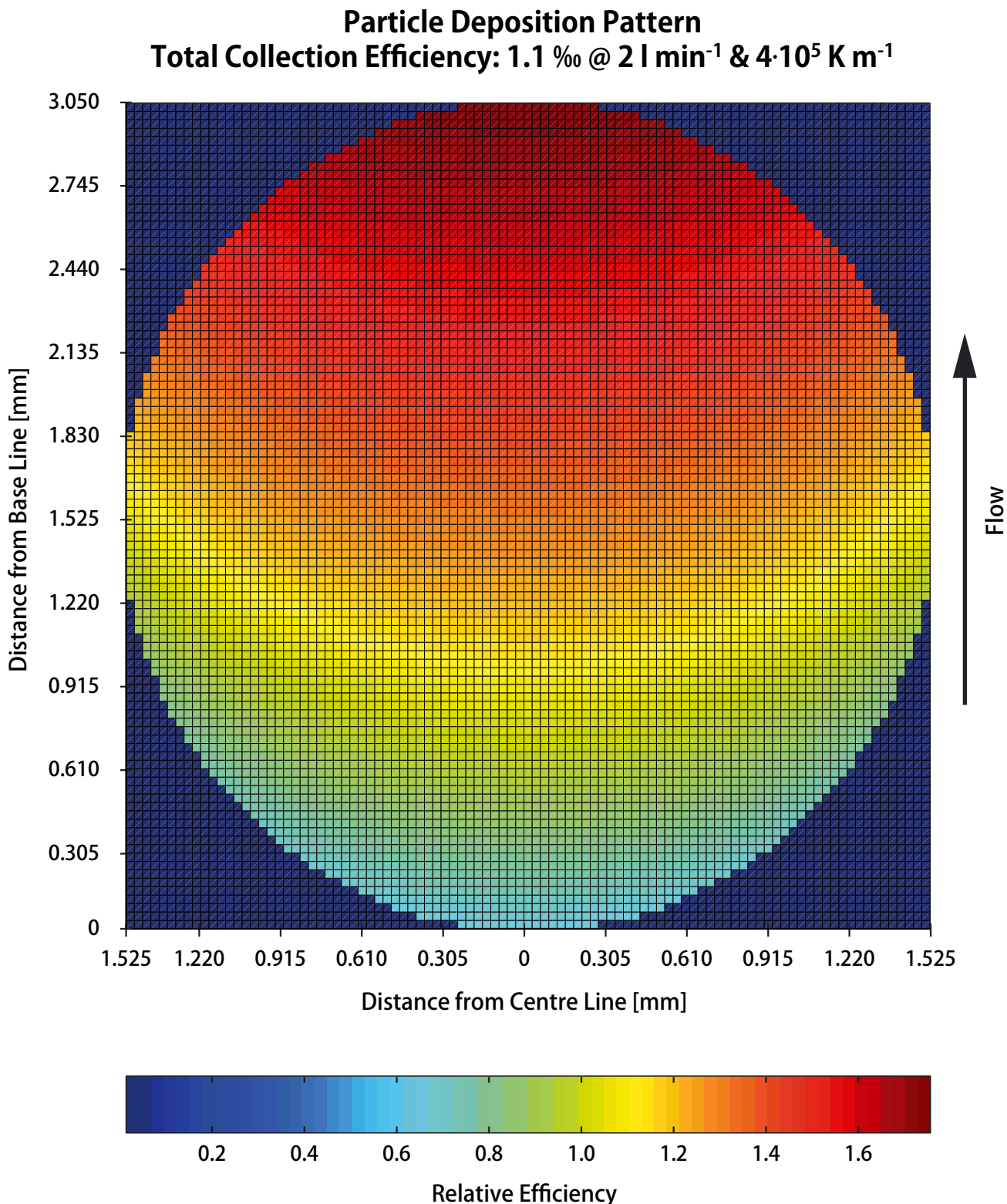


Figure 3.6: Deposition pattern as calculated by the MatLab model based on particle trajectories. Colours indicate the local deposition efficiency of a respective matrix cell relative to the average of the grid. The curved shape of areas with similar deposition efficiency is due to the circular geometry of the cold and hot plate. The deposition gradient is a consequence of the parabolic velocity profile.

4. Experiments and results

To derive quantitative particle number concentrations and particle size distributions from the measurements of particles deposited on a TEM grid, the particle deposition on the grid must be homogeneous and independent of particle size, shape, or composition. If that is not the case, calibration need to account for the inhomogeneous deposition patterns.

According to the theory, thermophoretic migration velocities are independent of particle composition and shape. This is strictly applicable for particles in the free molecular regime and, as an approximation, up to a few 100 nm (Brock 1962).

A series of experiments with polydisperse and monodisperse Ag aerosols were conducted to test the theoretical predictions, and to experimentally determine the sampling characteristics of the thermophoretic sampling device. The experimental systems are described in Figure 3.7 (a more detailed description of an essentially identical setup is given (e.g.) by Ku and Maynard (2006)).

Particles were analysed with an SEM (Scanning-Electron Microscope, FEI, XL30 FEG) and with a TEM (Philips, CM30, source LaB₆). Size distributions and number concentrations were derived from images using image analysis (image analysis) tools (Adobe Photoshop CS).

4.1 Polydisperse Ag aerosols

In a first series of experiments, Ag aerosols with modes at 45 nm and 90 nm, respectively, were generated (Fig. 3.7a) and sampled on carbon coated TEM grids. The size distribution of the particles was recorded online with an SMPS system (TSI 3080 Platform with 3081 differential mobility analyser and 3025 condensation particle counter). A series of 81 TEM images were taken from the centre section of each of the grids, and a particle size distribu-

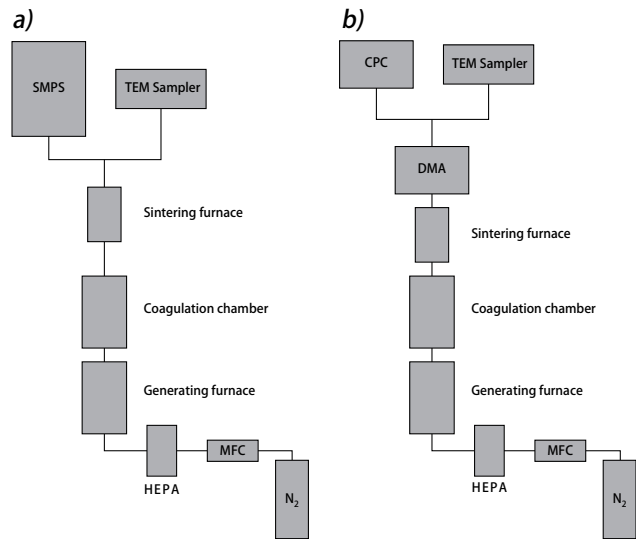


Fig. 3.7: Schematic representation of the facility for generating Ag aerosols. a: Setup for polydisperse aerosols. SMPS: scanning mobility particle sizer; MFC: mass flow controller. b: Setup for monodisperse aerosols. DMA: dynamic mobility analyser; CPC: condensation particle counter.

tion was derived from these images using image analysis. To derive the absolute particle number concentrations in the sampled air, the particle numbers obtained from image analysis were corrected with the modelled (size independent) deposition efficiency. In Figure 3.8 these size distributions are compared with the ones measured with the SMPS for the modes at 45 nm and 90 nm.

The black lines represent the particle size distribution of the Ag aerosol determined with the SMPS and the grey lines represent the results of the corrected TEM image analysis. The black circles depict the Gaussian fit of the TEM image analysis results. The comparison of the size distributions determined by SMPS and TEM image analysis

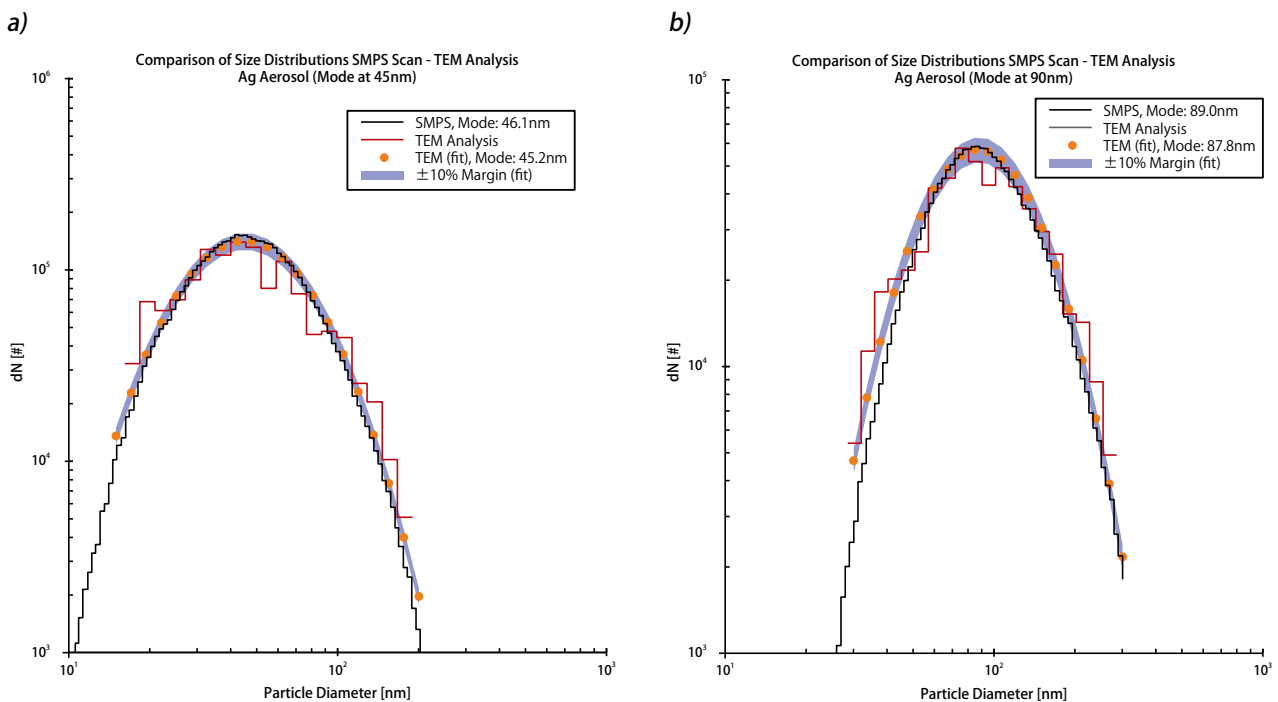


Fig. 3.8: Quantitative comparison of particle size distributions measured by the SMPS and calculated from TEM / IA using the described model. The black lines represent the SMPS scans, the red lines the TEM analysis and the yellow circles represent the Gaussian fit of the TEM / IA data. The particle number concentration of the aerosol determined by TEM IA in combination with the model lies within 10% of the SMPS results.

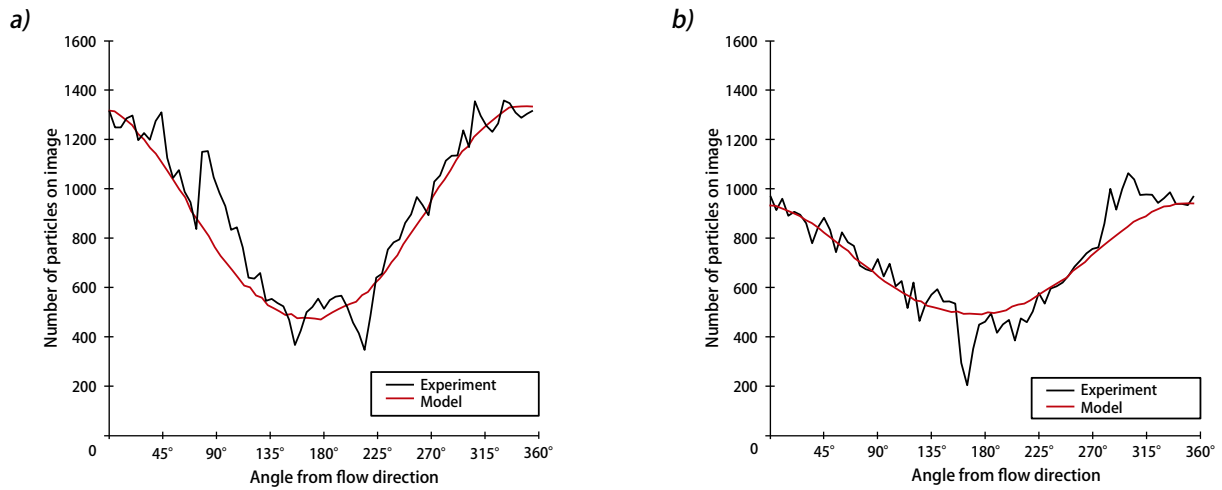


Fig. 3.9: Comparison of the calculated and measured particle deposition pattern using polydisperse Ag aerosols. The sample for figure a) was taken with a temperature gradient of $4 \cdot 10^5 \text{ K m}^{-1}$ and the sample for figure b) with a temperature gradient of $3.3 \cdot 10^5 \text{ K m}^{-1}$.

are in excellent agreement concerning modes as well as absolute particle numbers. For the Ag aerosol with mode at 46.1 nm (SMPS, $4.9 \cdot 10^6$ particles per cm^3) the TEM image analysis results in a mode at 45.2 nm ($5.3 \cdot 10^6$ ppcm 3) while for the Ag aerosol with mode at 89.0 nm (SMPS, $1.8 \cdot 10^6$ ppcm 3) the TEM image analysis results in a mode at 87.8 nm ($1.9 \cdot 10^6$ ppcm 3).

To further validate the model, two additional experiments (Ag, 45 nm) were conducted using different temperature gradients ($4 \cdot 10^5 \text{ K m}^{-1}$ and $3.3 \cdot 10^5 \text{ K m}^{-1}$). A series of 71 SEM micrographs around a circle of approximately 1.6 mm in diameter were recorded on each of these two TEM grids. The SEM was chosen as it is equipped with a fully automated stage which allows to precisely locate the position of the micrographs on the TEM grid. The numbers of particles on the micrographs were then determined by image analysis. A lower size limit of 25 nm was chosen for the Ag-particles because smaller particles cannot be detected reliably using our analytical setup. Although the mode of the size distribution is at 45 nm a significant number of particles are smaller than 25 nm. Thus, the particle number detected by image analysis is too low. However, because all images were treated exactly the same way, it affects only the absolute number of particles, the distribution pattern remains the same.

Figure 3.9 shows the comparison between results of the SEM image analysis (black lines) and the model calculations (grey lines). Figure 3.9a represents the sample taken at a gradient of $4 \cdot 10^5 \text{ K m}^{-1}$ and Fig. 3.9b of $3.3 \cdot 10^5 \text{ K m}^{-1}$ respectively. Again, the comparisons of the modelled and experimental data are in very good agreement.

4.2 Monodisperse Ag aerosols

In a second series of experiments, monodisperse Ag aerosols with sizes of 40 nm and 80 nm respectively, were generated (Fig. 3.7b) and sampled (separately) on carbon coated TEM grids. Thirty micrographs along a rim to rim transect through the centre of the TEM grid of each sample were taken with an SEM. The number of deposited particles was determined using image analysis. In contrast to the experiment shown in Figure 3.9, determination of absolute particle numbers was possible due to the monodisperse aerosols with particle sizes larger than the previously determined threshold for SEM image analysis of 25 nm. Based on particle number concentrations measured by the CPC (TSI Model 3025), the model was used to calculate the number of particles deposited on the TEM grid. The results can then be compared directly with the results from the SEM image analysis.

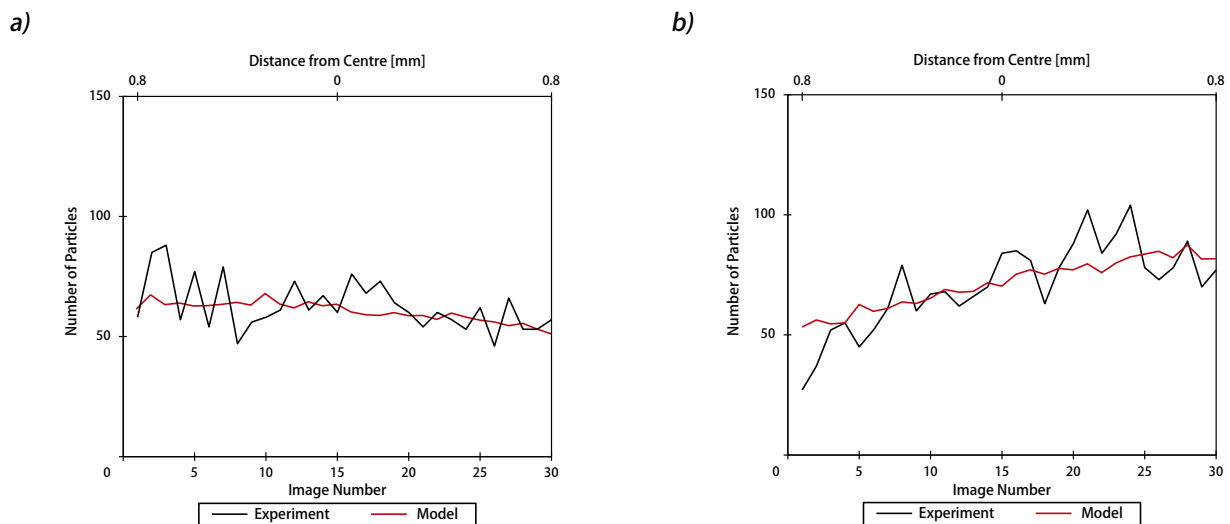


Fig. 3.10: Quantitative comparison of calculated and measured particle numbers from monodisperse Ag aerosols (particle diameters a: 80 nm; b: 40 nm). The micrographs for particle counting were taken along a transect.

Figure 3.10 compares the calculated (grey line) with the measured (black line) particle numbers in an experiment with 80 nm Ag particles (Fig. 3.10a) and one with 40 nm Ag particles (Fig. 3.10b). The close correspondence of experimental and modelled results shows that our model can reproduce the observed deposition pattern as well as the absolute particle number concentration.

5. Discussion and conclusions

The experiments reported in this paper have shown that the sampling efficiency of the thermophoretic sampling device described in this study is independent of particle size between 15 nm and 300 nm, in good agreement with the theory and with the results obtained by Messerer *et al.* (2003) who studied the thermophoretic deposition of soot particles. Furthermore, thermophoresis is independent of particle shape and composition (in the size range given) and, thus, enables representative sampling of atmospheric ultrafine particles.

Particle deposition in the central area of the TEM grids (concentric area of approx. 1 mm in diameter) is homogeneous within $\pm 10\%$. However, on larger scales, larger variations in particle deposition efficiency occur. This is due to the parabolic flow profile resulting in a higher particle flux in the centre of the channel than near the walls (Fig. 3.5a), and the circular temperature field. The numerical model developed for the precipitator takes these effects into account, and is capable of calculating the particle deposition pattern on the entire area of the grids (Fig. 3.6).

Using our model, quantitative particle number concentrations can be estimated from measurements made anywhere on the TEM grids, as long as the area of interest can be localized relative to the sample flow in the thermophoretic

sampling device. This can easily be achieved by using oriented TEM grids. Calibration experiments showed that particle size distributions and particle number concentrations derived from image analysis combined with deposition coefficients extracted from our model agree very well with SMPS measurements.

This thermophoretic precipitator thus makes it possible to quantify the number concentration of particles in the size range of 15 nm – 300 nm. The tools used for the counting procedure, e.g., SEM and TEM, make it possible to analyse the morphology, crystallography and chemical composition of each particle, e.g., it is possible, in the nanosize range, to determine variations of the latter physico-chemical parameters as a function of size. In addition, our model serves as a useful tool for calculation of the sampling time needed to get suitable TEM samples under given circumstances and, therefore, allows optimising sampling parameters.

Although only TEM and SEM were used for the analyses in this study, the device is not limited to the use of TEM grids as substrata. While built for thin (<0.1 mm) and magnetic substrata, minor modifications to the mounting system enable the use of other materials, such as gold foil, Si wafer, mica, or Si_3N_4 windows, for sampling. Thus, particles can also be investigated using analytical techniques such as atomic force microscopy (AFM) or scanning transmission x-ray microscopy (STXM).

Acknowledgments

This project was supported by SILAG Zurich and the Foundation for Pneumoconiosis-Research. We thank Martin Fierz of the University for Applied Sciences of Northwestern Switzerland for providing us with the facilities for producing the Ag aerosols necessary for calibrating the sampling device.

References

- Bang, J. J., Trillo, E. A. and Murr, L. E. (2003). Utilization of selected area electron diffraction patterns for characterization of air submicron particulate matter collected by a thermophoretic precipitator. *J. Air Waste Manage. Assoc.* 53:227-236.
- Berube, K. A., Jones, T. P., Williamson, B. J., Winters, C., Morgan, A. J. and Richards, R. J. (1999). Physicochemical characterisation of diesel exhaust particles: Factors for assessing biological activity. *Atmos. Environ.* 33:1599-1614.
- Brock, J. R. (1962). Theory Of Thermal Forces Acting On Aerosol Particles. *Journal Of Colloid Science* 17:768-780.
- Chen, Y. Z., Shah, N., Huggins, F. E. and Huffman, G. P. (2005). Transmission electron microscopy investigation of ultrafine coal fly ash particles. *Environ. Sci. Technol.* 39:1144-1151.
- Dixkens, J. a. F., H. (1999). Development of an electrostatic precipitator for off-line particle analysis. *Aerosol Science and Technology* 30:438-453.
- Gonzalez, D., Nasibulin, A. G., Baklanov, A. M., Shandakov, S. D., Brown, D. P., Queipo, P. and Kauppinen, E. I. (2005). A new thermophoretic precipitator for collection of nanometer-sized aerosol particles. *Aerosol Science and Technology* 39:1064-1071.
- Green, H. L. and Watson, H. H. (1935). *Medical Research Council Special Report Series* 199.
- Harrison, R. M. and Yin, J. X. (2000). Particulate matter in the atmosphere: which particle properties are important for its effects on health? *Sci. Total Environ.* 249:85-101.
- Kasper, G. (1982). Hot-Wire Thermal Precipitator With Low Inlet Losses And Low Size Selectivity. *Rev. Sci. Instrum.* 53:79-82.
- Ku, B. K. and Maynard, A. D. (2005). Comparing aerosol surface-area measurements of monodisperse ultrafine silver agglomerates by mobility analysis, transmission electron microscopy and diffusion charging. *J. Aerosol. Sci.* 36:1108-1124.
- Ku, B. K. and Maynard, A. D. (2006). Generation and investigation of airborne silver nanoparticles with specific size and morphology by homogeneous nucleation, coagulation and sintering. *J. Aerosol. Sci.* 37:452-470.
- Li, N., Sioutas, C., Cho, A., Schmitz, D., Misra, C., Sempf, J., Wang, M. Y., Oberley, T., Froines, J. and Nel, A. (2003). Ultrafine particulate pollutants induce oxidative stress and mitochondrial damage. *Environ. Health Perspect.* 111:455-460.
- Mathis, U., Kaegi, R., Mohr, M. and Zenobi, R. (2004). TEM analysis of volatile nanoparticles from particle trap equipped diesel and direct-injection spark-ignition vehicles. *Atmos. Environ.* 38:4347-4355.
- Maynard, A. D. (1995). The Development of a New Thermophoretic Precipitator for Scanning-Transmission Electron-Microscope Analysis of Ultrafine Aerosol-Particles. *Aerosol Science and Technology* 23:521-533.
- Maynard, A. D., Ito, Y., Arslan, I., Zimmer, A. T., Browning, N., Nicholls, A. and Nicholls, A. (2004). Examining elemental surface enrichment in ultrafine aerosol particles using analytical scanning transmission electron microscopy. *Aerosol Science and Technology* 38:365-381.
- Mercer, T. T. (1973). *Aerosol Technology in Hazard Evaluation*. Academic Press Inc., New York.

- Messerer, A., Niessner, R. and Poschl, U. (2003). Thermophoretic deposition of soot aerosol particles under experimental conditions relevant for modern diesel engine exhaust gas systems. *J. Aerosol. Sci.* 34:1009-1021.
- Oberdorster, G., Sharp, Z., Atudorei, V., Elder, A., Gelein, R., Kreyling, W. and Cox, C. (2004). Translocation of inhaled ultrafine particles to the brain. *Inhal. Toxicol.* 16:437-445.
- Panton, R. L. (2005). *Incompressible Flow*. John Wiley & Sons, Inc.
- Rowe, D. M., ed. (2006). *Thermoelectrics Handbook: Macro to Nano*. Taylor & Francis Group, Boca Raton.
- Seaton, A. and Donaldson, K. (2005). Nanoscience, nanotoxicology, and the need to think small. *Lancet* 365:923-924.
- Talbot, L., Cheng, R.K., Scheffer, R.W. and Willis, D.R. (1980). Thermophoresis of particles in a heated boundary layer. *J. Fluid Mech.* 101:737-758.
- Tsai, C. J. and Lu, H. C. (1995). Design And Evaluation Of A Plate-To-Plate Thermophoretic Precipitator. *Aerosol Science and Technology* 22:172-180.
- Waldmann, L. (1959). Über die Kraft eines inhomogenen Gases auf kleine suspendierte Kugeln. *Zeitschrift für Naturforschung Part A-Astrophysik Physik und Physikalische Chemie* 14:589-599.

3.3 Technical details

3.3.1 Development

The precipitator itself (as shown in Fig. 3.3) was designed by Prof. Heinz Burtscher of the University for Applied Sciences of Northwestern Switzerland and built by Leo Scherrer, now retired technician of the ETH Zurich, Department for Solid State Physics. Prior to the construction of the final sampling setup the parameters for standard operation had to be evaluated. Since the device is meant to be used for the collection of environmental aerosols at ambient conditions it had to be as flexible as possible.

The temperature field of the precipitator has a direct influence on the quality of the samples. Figure 3.11 shows dewpoint curves for four different temperatures of the cold plate (yellow: -5°C , blue: 5°C , red: 15°C and green: 25°C). Combinations of ambient temperature and relative humidity which lie above the curve will lead to condensation on the cold plate for that respective temperature setting. A temperature setting of 15°C for the cold plate was chosen for it is on the safe side for most applications. Only sampling under hot and/or wet conditions is problematic. While a large temperature gradient ensures a high deposition efficiency, the temperature required for the hot plate would pose a threat to particles with low thermal stability. In Table 3.1 the maximum temperatures encountered by particles settling on the cold plate are listed for two temperature gradients and different flow speeds. To keep the device as versatile as possible, a standard gradient of $4 \cdot 10^5 \text{ K m}^{-1}$ was chosen. At these temperature settings ($15^{\circ}\text{C} / 135^{\circ}\text{C}$) it is unlikely that particles get damaged, even at the lowest flow rate listed in Table 3.1.

Diffusion losses are always an issue when dealing with nano-sized particles. While low flow rates are necessary for a high deposition efficiency they also cause large diffusion losses in the sampling lines and especially the sampling channel. By allowing separate adjustment of the flow rates for the sampling lines and the sampling channel, diffusion losses prior to the channel can be eliminated without limiting the operation of the precipitator. For most sampling conditions diffusion losses have to be kept as low as possible. The required high flow rates, however, strongly reduce the collection efficiency of the precipitator. As a compromise, a flow rate of 2 l min^{-1} for both sampling lines and channel are chosen as standard parameters, reducing the flow rate in the sampling channel for low particle concentrations to 0.5 l min^{-1} (improving collection efficiency by a factor of nine). In Table 3.1 fractions of particles evading diffusion loss and reaching the sampling stretch for different sizes and flow rates are given. At 2 l min^{-1} the impact of size dependent diffusion losses on the particle size distri-

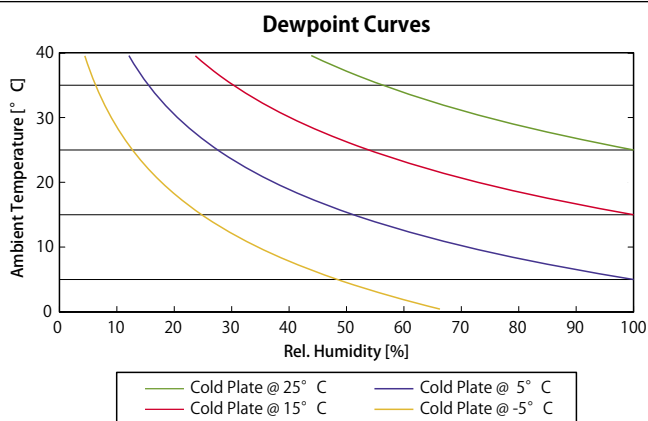


Figure 3.11: Dewpoint curves for standard pressure and four different temperatures of the cold plate (green, red, blue and yellow line). All combinations of ambient temperature and relative humidity above a coloured line, water will condensate on the cold plate.

bution is negligible (see Fig. 3.8a) but at 0.5 l min^{-1} particle size distributions need to be corrected.

Construction

A frame made of aluminium profiles (Phoenix Mecano) served as mounting base for the components of the prototype (Fig. 3.12). Aside the precipitator the prototype consists of a single vacuum pump (Rietschle Thomas model 8005V/22) which takes care of the flow through the precipitator, two mass flow controllers (MKS Type 259B 0-5 l min^{-1}) which regulate the flow rates through the bypass and the sampling channel (see Fig. 2.4b) and two USB data acquisition and control boards (DAQ, Meilhaus Electronics Redlab U12) combined with custom built electronics (by Leo Scherrer) which serve as interface to the computer for real-time status control of the flow rates and temperatures.

Since no hard wired control units are incorporated into the prototype's design, changes to hardware and operation parameters can be done on-the-fly.

LabView controls

The operation of the sampling device is entirely controlled by LabView. The program consists of four levels: configuration, warm-up, sampling run and reset (including recording of log files, see Appendix A.3.2). While the standard parameters for flow rates and temperatures are preset (but remain adjustable), the length of the sampling run has to be defined each time the program is being executed.

For the adjustment of temperatures and flow rates a commercial PID (Proportional-Integral-Derivative) algorithm (National Instruments) is applied. Sensor data for

Table 3.1

Comparison of operation parameters of the TPS at different flow speeds and temperature gradients. The dimensions of the sampling channel (width/height/length: 20/0.3/83 mm) and the temperature of the cold plate (15°C) were kept constant for all calculations.

flow [l min^{-1}]/[m s^{-1}]	fraction penetrating [%] ^a			z_{max} [mm] ^b dT = $4 \cdot 10^5 \text{ K m}^{-1}$	T [$^{\circ}\text{C}$] ^c	z_{max} [mm] ^b dT = $1 \cdot 10^6 \text{ K m}^{-1}$	T [$^{\circ}\text{C}$] ^c
	dp = 10 nm	dp = 15 nm	dp = 20 nm				
2.0 / 5.6	92.1	95.1	96.5	0.036	30	0.059	74
0.5 / 1.4	80.3	88.3	91.9	0.076	45	0.13	145
0.2 / 0.6	64.2	78.7	85.2	0.13	67	(>0.3)	(315)

^a Calculated for the flow path from the deceleration chamber to the leading edge of the Peltier element (@ 20°C and 1013 mbar).

^b Maximum height above the cold plate (centre line) at which a particle can enter the temperature field and still settle on the substrate.

^c Temperature at z_{max} above the centre of the grid.

the four variable parameters are read every 0.5 s which proved to be sufficient to sustain the set values within 3%. In order to be able to react quickly to changing conditions during long runs, the parameters for the four PID algorithms needed can be adjusted separately during the sampling run.

During warm-up the temperature gradient is being established as well as the flow rate in the sampling lines. The sampling channel remains closed. After the warm-up phase the flow through the sampling channel is gradually increased until the set value is reached. Meanwhile the flow through the bypass is reduced to keep the flow rate in the sampling lines at a steady state.

Deposition model

To get an idea of the deposition characteristics and collection efficiency of the precipitator, a numerical model was developed in MatLab. The temperature field produced by the circular cold and hot plate of the precipitator is assumed to be cylindrical in shape. This is - of course - a simplification. Since air is not a particularly good isolator the temperature field will rather be barrel-shaped and elongated in flow direction. However, due to the fact that the horizontal extension of the temperature field (≤ 4 mm) is up to 13 times larger than the vertical (0.3 mm), the deviation from a perfect cylinder and, thus, the error introduced is negligible.

The starting area for the model-particles lies in a plane perpendicular to the sample flow and tangential to the cold plate (Fig. 3.5). To improve the performance of the model, the starting height is limited to z_{max} . However, z_{max} is calculated for particles flying along the centre line of the cold plate. Therefore, the ratio of particle trajectories ending in a touch-down on the substrate to the ones that do not can easily be scaled to reflect collection efficiency of the device.

The coordinates of particles settling on the substrate are converted to matrix indices and the scaling factor of the particle is added to the respective matrix cell. In early versions of the model artefacts due to rounding mistakes were observed. Since these structures only occurred along the direction of the flow, variable time steps for the calculation of the trajectories were introduced. In the present version of the model (see Appendix A.3.1: TPS_incl.m) the length of the time step is generated by a random function once for each particle and varies between 2.5 μ s and 10 μ s.

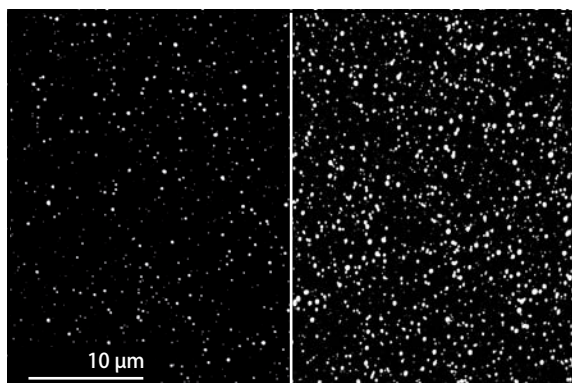


Figure 3.13: Two examples of BSE images taken at opposite sides of the same grid from the calibration experiment with polydisperse Ag Aerosol (mode at 45 nm).

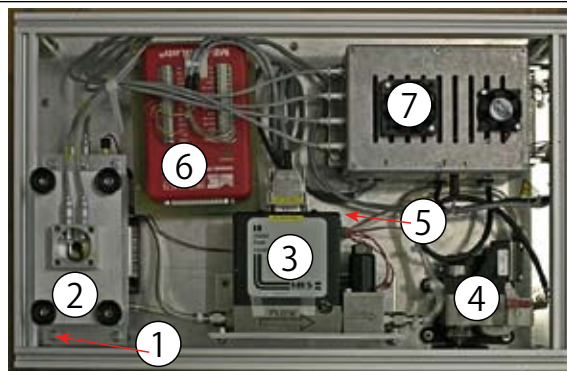


Figure 3.12: Top view of the prototype of the thermophoretic sampling device. (1) inlet (not visible), (2) precipitator, (3) mass flow controllers, (4) vacuum pump, (5) exhaust filter (not visible), (6) DAQ boards, (7) amplifier and power supply.

Figure 3.6 shows the deposition efficiency of the precipitator as calculated by the model (flow direction: bottom to top). The area shown corresponds to a TEM grid. The colours indicate the local deposition efficiency (for a single matrix cell, area approximately 30 μ m by 30 μ m) relative to the average of all cells of the grid. The warmer the colour, the more particles get deposited.

The influence of the circular plates is clearly reproduced by the curved isodensity lines. Equally obvious is the correlation of deposition efficiency and travelling distance through the temperature field. This is a direct consequence of the parabolic flow profile.

3.3.2 Experiments

Calibration

The analysis and counting of the particles for the calibration of the sampling device has been done with the help of SEM images. The computer controlled stage of the microscope and the automated particle analysis software allowed to recognize, precisely locate and analyse particles on large areas of the TEM grids in a reasonable amount of time. In Figure 3.13 two SEM micrographs from the calibration experiment with polydisperse Ag aerosol (mode at 45 nm) are shown. Both examples are from a series of pictures taken along a circle close to the edge of the usable

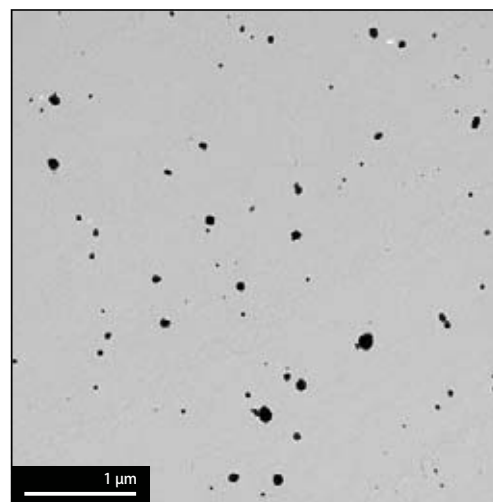


Figure 3.14: TEM bright field images taken from the same sample as the SEM images in Fig. 3.13 but from the centre of the grid. The particle density in this area of the grid is ideal for single particle analysis.

area of the TEM grid (see Fig. 3.9a for details). While both images were taken on the centre line of the grid (along the flow direction), the image on the left of Fig. 3.13 was made at about 0.9 mm from the leading edge of the grid and the image on the right at about 2.1 mm (see also Fig. 3.6).

Figure 3.14 shows an assembly of nine TEM images of the same sample, close to the centre of the grid. The TEM images can not be located exactly because the TEM grids used were not indexed. However, since the 81 images used for calibration were taken from a square area from the centre of the grid, the error due to the variation of the deposition efficiency is rather small (see also Fig. 3.8a and Fig. 3.6).

An important advantage of the thermophoretic precipitator is the gradient in deposition efficiency present across the grid. Due to this, the margin of appropriate collection times for given sampling conditions is rather large. For high particle loads, particle count and analysis is made close to the leading edge, whereas for low loads, the area near the trailing edge will be favoured.

Jungfraujoch

Weaknesses and flaws of a system are discovered easiest during operation in extreme conditions. The high alpine research station at the Jungfraujoch offers an ideal platform for benchmarking aerosol samplers. At an altitude of 3580 m above sea level the atmospheric pressure is reduced to 650 mbar and temperatures are below zero most of the year. Performance tests with the TPS were done at the beginning of 2005 and 2006.

Due to the (comparably) thin air and high temperatures inside the research station (up to 30°C) keeping the Peltier at a constant temperature required adjustments to the parameters of the PID algorithm. Once this has been done long term stability (sampling runs lasted up to seven days) of the parameters was ensured to $\pm 3\%$ of the initial settings.

During periods of bad weather, water accumulated on the TEM grids. This was due to melting ice crystals rather than due to humidity condensing on the cold plate. At outside temperatures between -20°C and -10°C this can hardly be avoided but is not a problem except during snow storms or clouds gathering around the research station. Samples taken during periods of clear skies showed no excess water gathering on top of the substrates. However, TEM images

of such samples (as seen in Fig. 3.15) reveal that almost all particles were originally frozen liquid drops with solid condensation cores.

The performance of the prototype of the TPS during the “stress tests” at the Jungfraujoch attests reliability and versatility. The standard parameters as determined during the evaluation period proved to suit the precipitator well - in its present configuration.

3.3.3 Outlook

In order to improve the performance of the thermophoretic sampling device certain design changes have to be made. The dimension of the sampling channel is crucial for the sampling performance. Reducing the length of the sampling channel to 40 mm (cutting the distance from the beginning of the channel to the leading edge of the grid in half) reduces diffusion losses by 50%. This would be a big advantage for sampling conditions with low particle number concentrations. Flow speeds could be reduced to 1.4 m s^{-1} (0.125 l min^{-1}) and size dependent diffusion losses would still be acceptable while improving the collection efficiency to 3.6% (compared to 0.1% with the current setup).

By reducing the width of the channel to 5 mm, the flow rate can be reduced to 0.5 l min^{-1} . Although this has no influence on the deposition characteristics - the flow speed remains at 5.6 m s^{-1} - the efficiency is improved by a factor of four. This does not change sampling times needed, it does change the perception of the TPS though (PR is getting important...).

Changing the geometry of the temperature field is an even better way to improve the collection efficiency than lowering the flow speed. The deposition rate could be increased by placing the TEM grid in a circular pit at the far end of a long, narrow rectangular heating plate instead of the circular one used in the present setup (Fig 3.16), opposed by a cold plate with identical dimensions. The length of the rectangle should be chosen such that particles flying at half the height of the channel, where the highest particle flux is located (see Fig. 3.5a), settle on the grid. Theoretically, a collection efficiency around 10% should be possible without reducing flow speeds or increasing the temperature gradient. However, tweaking the geometry of the precipitator would still need some additional modelling.

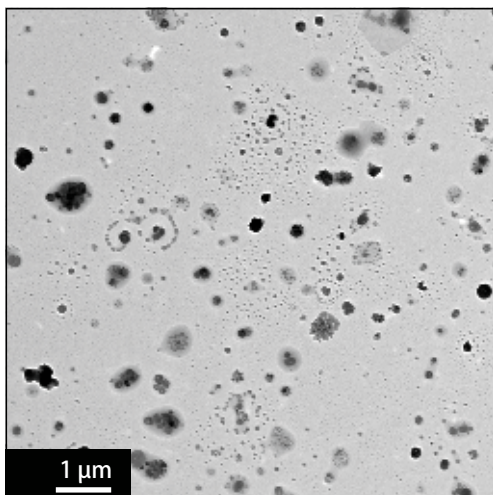


Figure 3.15: TEM image of samples taken during the benchmarking experiments at the Jungfraujoch.

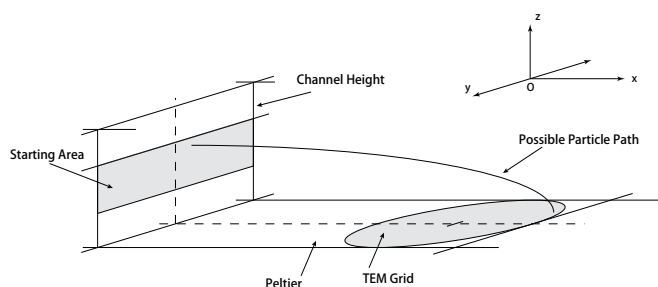


Figure 3.16: Proposed geometry for the cold and hot plate for improved deposition efficiency and characteristics.

Welding Fumes

- Introduction
- Publication
- Technical Details

«It's a miracle these people ever got out of the 21st century.»

McCoy, Star Trek IV

4 Welding Fumes

4.1 Introduction

4.1.1 Occupational health

Traditionally, occupational aerosol exposure is assessed by means of aerosol mass and bulk chemical analysis with the only exception being fibrous aerosols (such as asbestos). However, these criteria are certainly not ideal for characterising nano-sized materials. Although the scientific community agrees on this point, no consensus on which particle properties are primarily responsible for their effect on health has been found yet.

While it is necessary for regulatory purposes to define one particle property as decisive, a combination of factors is more likely to be the cause of adverse health effects. Accordingly, it is inevitable to measure as many parameters as possible to provide a comprehensive data set to the toxicologists for their investigations.

So far, commercial (engineered) nanoparticles (such as TiO₂, SiO₂ or carbon nanotubes) have preferably been used for toxicological studies, because they are well characterised and readily available. However, engineered particles are produced in well confined premises and once they're packaged its highly unlikely that they are set free as individual particles once more, let alone in concentrations as applied in toxicological studies. Thus, even though almost exclusively engineered nanoparticles are used for these studies, very few have so far addressed the potential adverse health impact of these particles at concentrations frequently found in working environments (Maynard and Kuempel 2005).

Nevertheless, since nanotechnology is increasingly gaining speed guidelines for safe handling of engineered nano-sized particles are needed. A first approach has been published by the National Institute for Occupational Safety and Health (NIOSH 2006) as a basis for discussion.

However, this guideline is only remotely applicable to working environments where nano-sized particles are produced involuntarily, such as in welding shops. Fact is that methods for characterising and quantifying nanoparticles in occupational environments are largely underdeveloped (Wiesner 2006). Studies such as the one by Brouwer *et al.* (2004) and the one described in chapter 4.2 remain the exception.

4.1.2 Analytical methods

With two calibrated and tested sampling devices for ultrafine particles at hand, the course of action was obvious. While the principal analysis was to be done on a TEM, online instruments were to be used to gather as much information as possible *in situ* to clarify the context.

Online measurements

For a complete assessment of a working environment the particle sources need to be characterised as well as the typical surroundings in which the employees spend most of their working day. This requires at least three measurement sites: Directly at the source to get an idea of the emission profile, at an employee's typical distance to the source and at a background site.

Measurements at the source represent a worst case scenario, of course. But more importantly this data serves as a reference point for the exposure situation at the other

sampling sites. Based on the differences between the measurement points information on the efficiency of the air exchange within the premises can be gathered. Further, clues on the persistence of different particle classes can be gained.

The sampling site in the vicinity of the workers contains valuable information on the employees' exposure to ultrafine particulates. Delivering data on relevant exposure levels in terms of particle number concentration and size distribution that should serve as guidelines for toxicological investigations.

The data collected at background measurement sites are a benchmark for the quality of the ventilation system of the premises. Steadily increasing particle number concentrations during the day are an indicator of poor air exchange rates. Influences from events from the outside of the premises, e.g., rush hour traffic, can easily be excluded due to (possibly) different particle size distributions and the time stamps of the events.

In terms of instrumentation, it is always advisable to use more than one system to ensure redundancy of the data or at least to enable cross-checks to expose measurement artefacts (a description of the functional principles of the instruments is given in chapter 1.2).

The scanning mobility particle sizer (SMPS) is a widely accepted standard for recording particle size distributions. However, even the fastest ones available need one minute for a scan (from 10 nm to 500 nm), which can be a handicap (see chapter 4.3.1). The fast mobility particle sizer (FMPS) has a resolution of 1 second with a comparable size range (5.6 nm - 560 nm) at the cost of reduced size resolution (32 size bins instead of the SMPS' 54). While the FMPS delivers important information on the evolution of particle size distributions (e.g., short lived nucleation events) the reference instrument is still the SMPS.

Concerning plain particle number concentrations, much simpler and smaller instruments are available and should be considered for measurement campaigns as well. Instruments like the electronic diffusion battery (EDB, Fierz *et al.* 2002) or the diffusion size classifier (DiSC, Fierz and Burtscher 2002) deliver limited information on size distributions as well but their primary value lies in the accurate measurement of particle number concentrations with high time resolution (1 s).

While the DiSC recommends itself as a stand alone monitoring device (small, battery operated and capable of wireless data transmission), the EDB should be considered as a cross reference for the number concentrations measured by FMPS and/or SMPS.

Offline measurements

The collection of particle samples for subsequent offline analysis usually concentrates on the sites representative to the employees' exposure situation for most part of the day. Because these particles need to be considered in toxicological studies concerned with occupational hazards related to suspended respirable particles.

To verify whether particle characteristics change within the premises, additional samples should be collected directly at the source. These samples have the added advantage of being comparably free of particles not directly related to the source.

Bulk chemical analysis of filter samples deliver valuable information on trace elements and substances regulated by federal agencies. However, these analyses are dominated by PM10 and the PM0.1 fraction has hardly any influence on the results.

While this may not be a drawback if the samples are collected directly at the particle source, it still lacks the information on the whereabouts of the elements. For solid, insoluble particles (e.g., welding fumes) only the surface composition is decisive for its effect on an organism.

To get access to this information electron microscopy is the method of choice (see, e.g., Grekula *et al.* 1985, Utsunomiya and Ewing 2003, Maynard *et al.* 2004). To be able to relate the results of the microscopic single particle analysis quantitatively to the particle exposure at the measuring site, calibrated sampling devices are necessary which collect the particles directly onto the appropriate substrates for the analysis.

References

- Brouwer, D. H., Gijssbers, J. H. J. and Lurvink, M. W. M. (2004). Personal exposure to ultrafine particles in the workplace: Exploring sampling techniques and strategies. *Ann. Occup. Hyg.* 48:439-453.
- Fierz, M., Scherrer, L. and Burtscher, H. (2002). Real-time measurement of aerosol size distributions with an electrical diffusion battery. *J. Aerosol. Sci.* 33:1049-1060.
- Fierz, M. and Burtscher, H. (2005). A portable diffusion size classifier, in *European Aerosol Conference*, W. Maenhaut, ed., Gent, Belgium, 423.
- Grekula, A., Ristolainen, E., Tanninen, V. P., Hyvarinen, H. K. and Kalliomaki, P. L. (1986). Surface and Bulk Chemical-Analysis on Metal Aerosols Generated by Manual Metal Arc-Welding of Stainless-Steel. *J. Aerosol. Sci.* 17:1-9.
- Lorenzo, R., Kaegi, R., Gehrig, R. and Grob ty, B. (2006). Particle emissions of a railway line determined by detailed single particle analysis. *Atmos. Environ.* 40:7831-7841.
- Maynard, A. D., Ito, Y., Arslan, I., Zimmer, A. T., Browning, N., Nicholls, A. and Nicholls, A. (2004). Examining elemental surface enrichment in ultrafine aerosol particles using analytical scanning transmission electron microscopy. *Aerosol Science And Technology* 38:365-381.
- Maynard, A. D. and Kuempel, E. D. (2005). Airborne nanostructured particles and occupational health. *J. Nanopart. Res.* 7:587-614.
- National Institute for Occupational Safety and Health, (NIOSH) (2006). Approaches to Safe Nanotechnology: An Information Exchange with NIOSH. Approaches to Safe Nanotechnology: An Information Exchange with NIOSH *online resource* : <http://www.cdc.gov/niosh/topics/nanotech/safenano/>.
- Utsunomiya, S. and Ewing, R. C. (2003). Application of high-angle annular dark field scanning transmission electron microscopy, scanning transmission electron microscopy-energy dispersive X-ray spectrometry, and energy-filtered transmission electron microscopy to the characterization of nanoparticles in the environment. *Environ. Sci. Technol.* 37:786-791.
- Wiesner, M. R., Lowry, G. V., Alvarez, P., Dionysiou, D. and Biswas, P. (2006). Assessing the risks of manufactured nanomaterials. *Environ. Sci. Technol.* 40:4336-4345.

Extending the assessment procedures for exposure situations at working environments to ultrafine particles

R. Lorenzo^{a,c}, P. Steinle^b, B. Grobéty^{c,d}, R. Kaegi^e

^aEmpa, Materials Science & Technology, Laboratory for Air Pollution & Environmental Technology, Überlandstrasse 129, CH-8600 Dübendorf, Switzerland

^bSUVA, Swiss National Accident Insurance Fund, P.O. Box 4358, 6002 Lucerne, Switzerland

^cUniversity of Fribourg, Institute for Mineralogy and Petrography, Ch. du Musée 6, CH-1700 Fribourg, Switzerland

^dFRIMAT, Fribourg Center for Nanomaterials, Perolles, 1700 Fribourg, Switzerland

^eEawag, Swiss Federal Institute for Aquatic Science and Technology, Urban Water Management, Überlandstrasse 133, CH-8600 Dübendorf, Switzerland

Submitted 27 July 2007

Abstract

A combination of online instruments and sampling devices for the subsequent offline analysis of fine (<600 nm) and ultrafine (<100 nm) aerosols for a complete assessment of a working environment is proposed and tested at a welding shop. Online measurements show highly variable particle production rates during welding and a considerable increase in background number concentrations of fine particles during the day. The comparison of two work places within the same facility reveals comparable particle number concentrations but significantly differing size distributions. Through single particle analysis on a transmission electron microscope three different types of primary particles are defined. While they can be distinguished by their morphology, energy dispersive X-ray analysis and crystallographic methods indicate that the different types of primary particles all consist of the same base material.

© 2007

1. Introduction

Ultrafine (diameter <100 nm) and nano-structured particles have long been neglected in the context of occupational health. In their perspective on “airborne nano-structured particles and occupational health” Maynard and Kuempel (2005) leave no doubt on the necessity of detailed assessments of work place exposures to nano-sized particles. While the possibility of adverse health effects of nano-sized airborne particulates in general (Seaton and Donaldson 2005) and of metal industry related particles (Antonini 2003) specifically is beyond discussion, the underlying physical properties of the particles and the mechanisms responsible for their effect still remain unclear (Harrison and Yin 2000; Maynard and Kuempel 2005; Vincent 2005). Nevertheless, based on the data available first guidelines to safe handling of nanomaterials have recently been established (NIOSH online resource 2006).

The particles (involuntarily) produced by the metal industry are well characterised. Particulate emissions from nickel refineries (Hoflich *et al.* 2000), from production sites for manganese alloys (Gunst *et al.* 2000) as well as from aluminium smelter potrooms (Hoflich *et al.* 2005) have been analysed by electron microscopy. Size distributions (Jenkins *et al.* 2005) and chemical composition (Grekula *et al.* 1986) of welding fumes have been investigated as a function of operating parameters (Zimmer *et al.* 2002) and bulk metallurgy (Zimmer 2002). However, the quantification of the emission and consequently the exposure of the employees to ultrafine welding aerosols has not been attempted, yet.

In most countries welding fume exposure is evaluated and regulated by the total mass of the welding fume independent of particle size distribution and/or by the total mass of specific contaminants (e.g. Ni, Cr, Mn and Fe). However, surface area becomes increasingly important with decreasing particle size and since for solid, insoluble

particles like welding fumes, only the surface layer is decisive for its effect on an organism, it is important to know the composition of the surface layer and whether it differs from the particle core. Accordingly, if specific contaminants accumulate on the particle surface, even if the total mass limits for these substances are not exceeded, welding fumes may be highly toxic.

With regard to occupational safety and hygiene a complete assessment of the exposure to ultrafine particles in a working environment is necessary (Maynard and Kuempel 2005; Wiesner *et al.* 2006) to verify whether safety precautions in effect are sufficient and to uncover possible flaws. The measurement strategy proposed by Brouwer *et al.* (2004) for a first assessment of the exposure requires an extensive instrument park and the measurement program is rather time consuming.

In this study we propose a measurement strategy suitable for the periodic assessment of the exposure to ultrafine particles at a work place and we evaluate online instruments for the continuous monitoring of the exposure

Table 4.1

Principal alloys present in the steel types used for GMAW. The diameter of the welding rod is 1.2 mm for both techniques. Base materials are cleaned and heated to ~110°C prior to welding.

	Base Material	Welding Rod
Material Number	1.4314 ^a	1.4351 ^b
Si	< 0.70%	0.25 - 0.55%
Mn	< 1.50%	0.55 - 0.95%
Cr	12.0 - 14.0%	12.7 - 14.8%
Mo	0.30 - 0.70%	0.35 - 0.75%
Ni	3.50 - 4.50%	3.10 - 4.90%

^a Traces (< 0.1%) of C, P, S and N are tolerated.

^b Traces (< 0.1%) of C, P and S are tolerated.

situation. The proposed combination of online monitoring of the emission and offline chemical and morphological analysis of the emitted ultrafine particles with analytical electron microscopy (AEM) allows a complete characterisation of the specific working area concerning size distribution and chemical and morphological properties of the ultrafine particles. The time resolved particle number concentration measurements as well as the detailed analysis of the chemical composition, the morphology and the surface properties of individual particles results in a comprehensive data set required to design toxicological studies related specifically to occupational health.

2. Experimental

2.1 Sampling site

The engineering business that served as a test platform for our measurement setup applies computer controlled and semi automated welding techniques. The underlying process for both techniques is gas metal arc welding (GMAW) on steel 1.4313 (Table 4.1) using steel welding rods (steel 1.4351; Table 4.1) and shield gas consisting of 97.5% Ar and 2.5% CO₂.

A detailed plan of the premises and sampling positions is given in Figure 4.1. For a complete assessment of the exposure of the welders and process supervisors to welding fumes the sampling positions were chosen to be representative for fresh fumes (pos. 1 in Fig. 4.1b&c), maximum exposure situations during spot tests (pos. 2 in Fig. 4.1b&c), workroom air in the vicinity of the welding robots (pos. 3 in Fig. 4.1b&c) and background concentrations (pos. 4, Fig. 4.1b&c).

The entrance to the premises - a single door - stayed open at all times, which corresponds to standard operating procedures. Of the two welding robots installed in the larger hall only the one used for our measurements was in operation. A CNC lathe installed in the same hall, has not been used that day.

Of the welding cubicles in the smaller hall, only the one used for our measurements has been used all day. One of the neighbouring cubicles has been in use sporadically for manual welding.

2.2 Instrumentation

Online measurements of particle size distributions and number concentrations were performed with a fast mobility particle sizer (FMPS, TSI Model 3091, size range: 5.6 - 560 nm) and a scanning mobility particle sizer (SMPS, TSI Model 3034, size range: 10 - 500 nm). While the time resolution of the FMPS can be as short as 1 s, the SMPS used needs 3 min for one scan. As the variations in the particle number concentrations occurred on smaller time scales, the air used for the SMPS measurements was first homogenized in a sampling bag (110 litres, electro-conductive). It takes 15 minutes to fill the bag (passively). Therefore, SMPS measurements performed with air drawn from the bag represent average values over a time period of 15 minutes. The bag has been calibrated for particle losses. Additionally, particle number concentrations were measured with high time resolution (1 s) with a diffusion size classifier (Fierz and Burtscher 2004) (DiSC, size range: 10 - 300 nm).

Particle samples for single particle analysis by transmission electron microscopy (TEM, Philips CM 30 LaB₆ source,

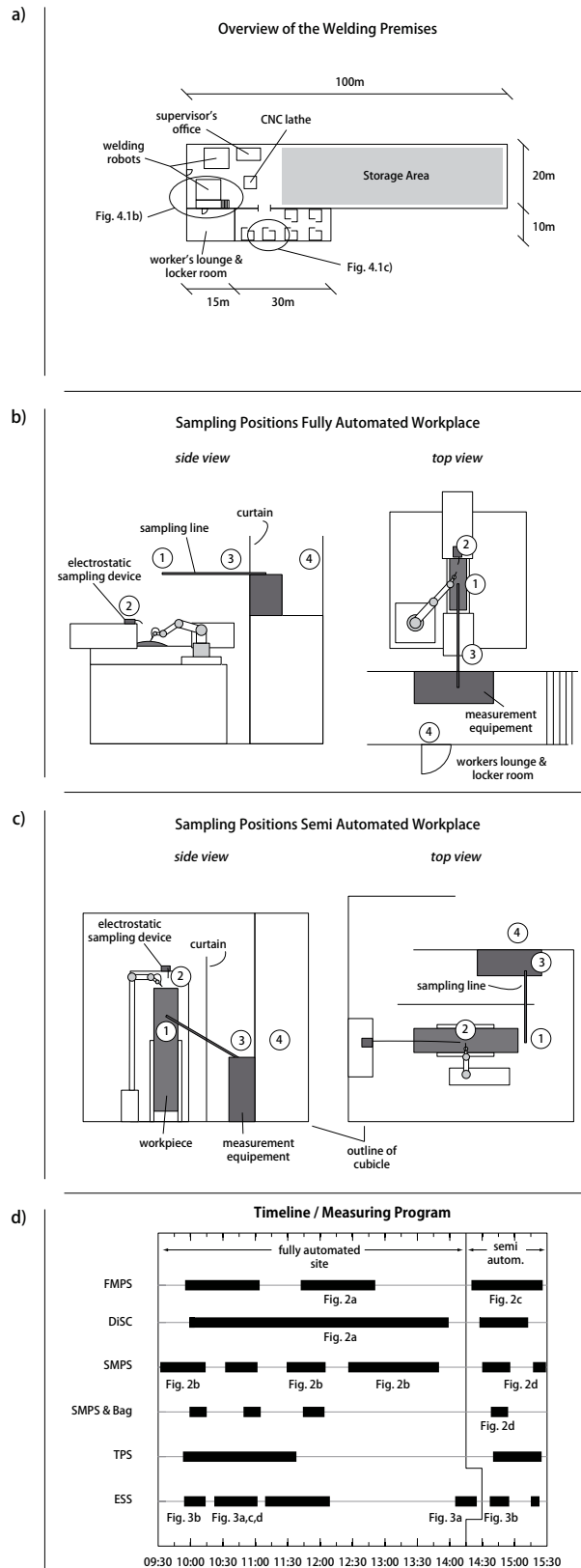


Fig. 4.1: Details of the measuring site and schedule.
a: Overview of the welding premises.
b: Inlet positions at the fully automated workplace. Supervisors normally stay at background positions (4), rarely - during spot testing - near position (2). (1): Fresh fumes at ~1 m distance; (3): average exposure situation at ~2 m distance.
c: Inlet positions at the semi automated workplace. Here, supervisors have to stay in the vicinity of the work piece (3) and spot tests are more frequent (2). (1): Fresh fumes at ~1 m distance; (4): background position.
d: Sampling schedule of the different instruments and references to the figures, in which the corresponding data is being displayed.

equipped with EDAX energy dispersive spectrometer, EDX) were collected directly onto TEM support grids with a thermophoretic (TPS, Lorenzo *et al.* 2007) and an electrostatic (ESS, Fierz *et al.* 2007) sampling device. The efficiency of both devices are calibrated, which allows to extract quantitative emission data from this offline technique. Samples were collected on C coated Ni grids (TPS), C coated Cu grids (ESS) and Cu grids with a lacy C film (ESS). An overview of the sampling schedule is given in Figure 4.1d.

3. Results and discussion

3.1 Online data

A fast and reliable method to get an overview of the particulate exposure at a work place is to measure the number concentration and to determine the mean particle diameter. For this study we compared two instruments a FMPS and a DiSC. The FMPS' primary use is registering particle size distributions with high time resolution (1 s) and delivers valuable information on the evolution of particle number concentrations. Since the FMPS is well established it served as a benchmark for the much simpler and highly portable DiSC, which is basically a small electrical diffusion battery (Fierz *et al.* 2002) with a time resolution as small as 1 s. Being the size of two average lap-top computers stacked on each other, battery operated and capable of wireless data transmission it's a valuable candidate for a mobile low cost on-site monitoring device.

Variations up to two orders of magnitude in the particle number concentration were registered during normal welding operations (Fig. 4.2a, measured at pos. 4.3, Fig. 4.1b). The base concentration, e.g., for the measuring period (11:30 - 12:30) is around $6 \cdot 10^4$ particles cm^{-3} , but concentrations above $5 \cdot 10^5$ ppcm^3 are frequent and short bursts may even top 10^6 ppcm^3 (for comparison: the average particle number concentration 25 m from a heavily frequented Swiss highway is $7 \cdot 10^4$ ppcm^3). The robot stopped 15 minutes after the start of the measurement period for a quarter of an hour and resumed welding afterwards for five minutes. Operations then stopped for a wire change and resumed welding again at min 45 for the remainder of the hour. Figure 4.2a shows good agreement between the two instruments (FMPS data for the size range of 10 - 300 nm has been used to match the size range of the DiSC). While both devices register the high particle events simultaneously, the DiSC underestimates peak particle concentrations. This is due to the fact that we used a prototype of the instrument which was not capable of handling such high number concentrations. In the final version of the instrument the concentration range that can be measured has been considerably increased.

At the fully automated work place supervisors are not always in the vicinity of the welding robots. Since high number events are mostly due to particles smaller 50 nm the question on the supervisors' average exposure arises. Therefore, the evolution of the particle number concentrations need to be amended by particle size distributions measured at a background position. In Figure 4.2b (measured at pos. 4, Fig. 4.1b) average particle size distributions from three series of SMPS scans are shown. All size distributions are bi-modal (40 nm, 150 nm), but only the larger particles are being accumulated. This leads to an increase in background particle number concentration with time from $5.3 \cdot 10^4$ ppcm^3 (09:30 - 10:30) to $7.7 \cdot 10^4$ ppcm^3 in the early afternoon (12:15 - 13:45).

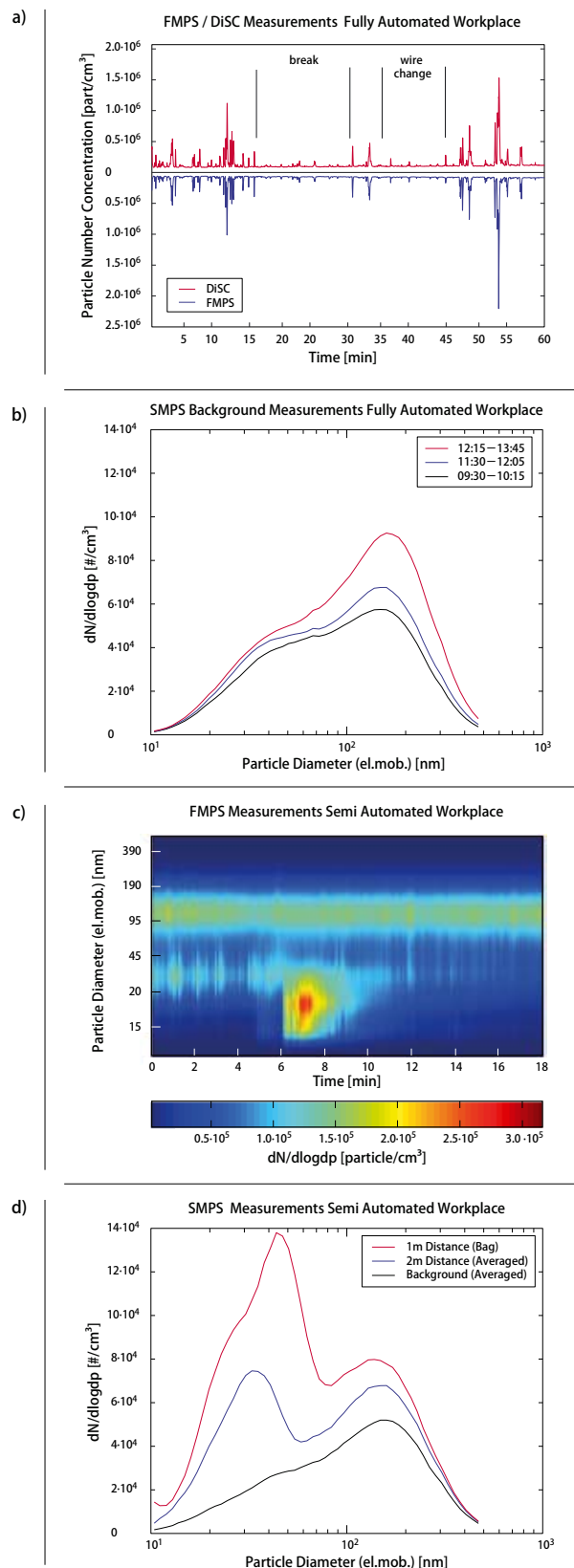


Fig. 4.2: Results of the online measurements.
a: Particle number concentration measured by FMPS and DiSC with inlet position (3) (Fig. 4.1b).
b: Particle size distributions (averaged) at the background position (4), Figure 4.1b, observe the accumulation of the mode at 150 nm ($5.3 \cdot 10^4$ ppcm^3 , $6.0 \cdot 10^4$ ppcm^3 , $7.7 \cdot 10^4$ ppcm^3). Position (4) is right at the door to the worker's lounge, where the employees normally have lunch.
c: FMPS measurements performed at inlet position (1), Fig. 4.1c.
d: Comparison of SMPS measurements of sample taken at different inlet positions. (4) (15:15-15:30; $4 \cdot 10^4$ ppcm^3), (3) (14:30-14:54; $6 \cdot 10^4$ ppcm^3) and (1) (14:38-14:54; $1 \cdot 10^5$) (Fig. 4.1c), going from bottom to top.

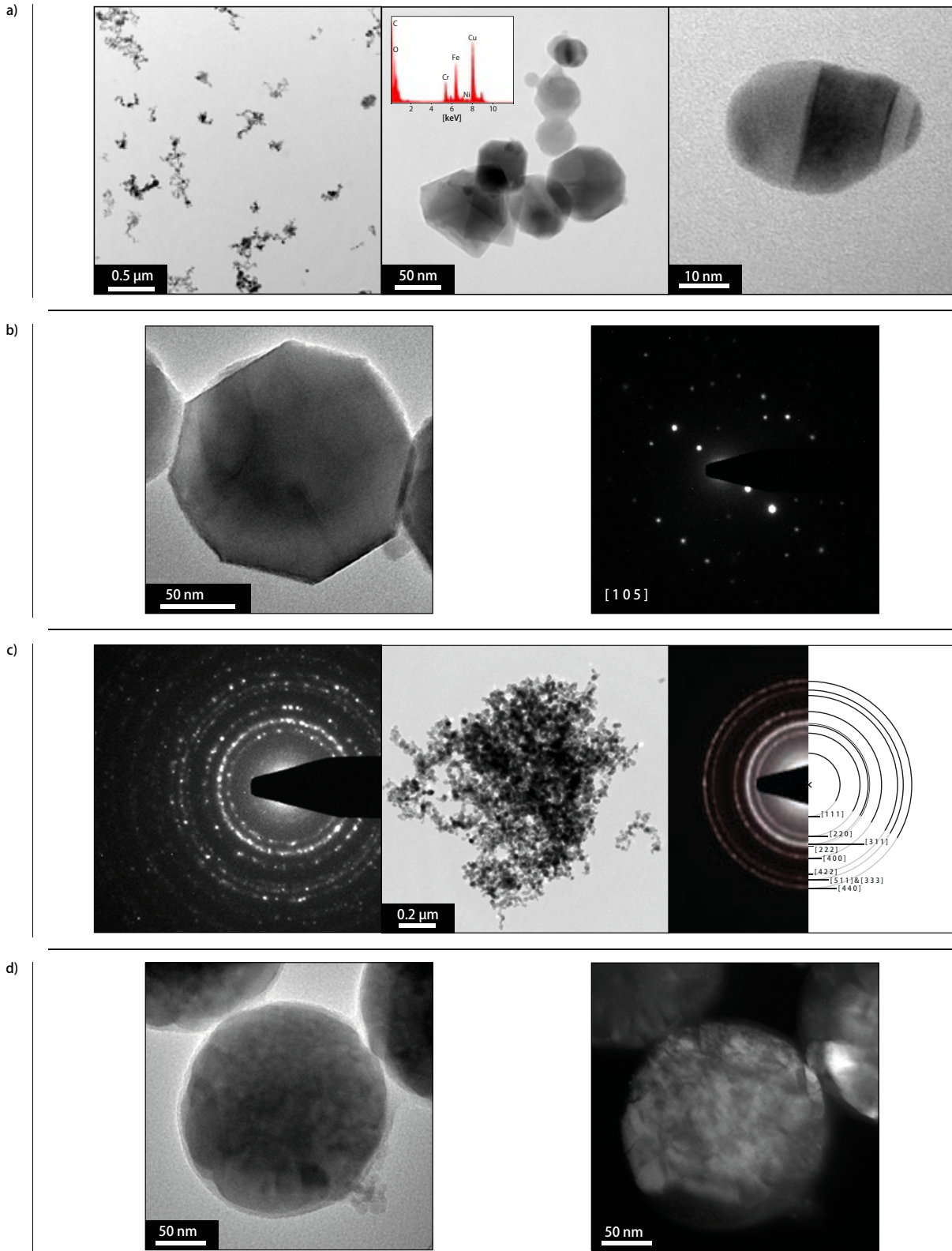


Fig. 4.3: Results of the offline TEM-AEM analyses.

- a: Overview (left). Typical agglomerate of the intermediate size range (mode at 150 nm). The EDX analysis revealed high Fe and O contents, along with some minor Cr and Ni. The Cu and C peaks originate from the TEM grid used (middle). Image of a twinned particle of the 40 nm mode (right).
- b: Image of a primary particle (left) and a corresponding selected area diffraction pattern (SAED, right). The diffraction pattern could also be indexed for the [105] zone of magnetite. (c).
- c: (left) Powder diffraction pattern of a large agglomerate (middle). (right) Powder diffraction pattern of a large cluster of agglomerates and the calculated and indexed powder pattern of Magnetite (Fe_3O_4 , spinel structure Fd-3m, origin centred).
- d: Structural analysis of a large primary magnetite particle. Observe the thin rim around the particle. On the right is a dark-field (DF) image ($g = 511$) of the same particle. The thin rim remains dark and is, therefore, either amorphous or consist of a different phase. The light contrast speaks in favor of an amorphous structure.

At the semi automated work places the supervisor's presence is required at all times during operation. Therefore, measurements in the vicinity of the welding robots are necessary. Figure 4.2c shows a series of FMPS spectra with 1 s time resolution (measured at pos. 1, Fig. 4.1c, 14:40 - 14:58). Similar to the measurements from the fully automated welding robots, particle size distributions are bi-modal. The mode at 150 nm which has been shown to accumulate in the background, is constantly present as is the mode at 40 nm, although the latter with highly variable concentrations. Additionally, a nucleation burst has been registered - starting at minute six and lasting for about 4 min. These events are frequent but vary in magnitude and length. This is also the case for the fully automated work place. In Figure 4.2a the nucleation bursts are indicated by the high concentration peaks.

The premises for semi automated welding (see Fig. 4.1c) are subdivided in cubicles, one for each welding station. To verify whether this arrangement has a positive influence on the workers exposition to welding fumes, measurements at three different positions in- and outside of a cubicle (pos. 1, 3 and 4, see Fig. 4.1c) were performed. In Figure 4.2d the particle size distributions of the three sampling positions are compared. Although the measurements at these sites were done in the afternoon, background concentrations were noticeably lower ($4 \cdot 10^4$ ppcm³) than at the premises for fully automated welding.

In contrast to the fully automated work places, during semi automated welding the employees' presence in the vicinity of the welding robots (≤ 2 m distance) is mandatory. Therefore, concerning number concentrations, the overall exposure at the two work places are comparable (around $6 \cdot 10^4$ ppcm³). However, due to the proximity to the welding robots supervisors at the semi automated work places are exposed to considerably more smaller particles (compare Fig. 4.2b&d).

The measurement of PM10 mass concentrations at both work places (collected at pos. 2, Fig. 4.1b&d) leads to similar results. While the values for the fully automated (0.21 mg m^{-3}) and semi automated work place (0.18 mg m^{-3}) are well below the mass limit of 3 mg m^{-3} , they are still roughly four times the limit for urban areas of 0.05 mg m^{-3} (mass limits for Switzerland only).

3.2 TEM analysis

Detailed information on the nature of the particles the employees are exposed to can be gained by single particle analysis. Figure 4.1d gives an overview on the samples taken. Since both precipitators are calibrated, the frequency of particles on the grid is representative for the averaged particle concentrations met during sampling. However, because sampling times can be quite short (5 min), the accompanying online measurements are required to set the results of the offline analysis in relation to the exposure of the employees over a longer period of time.

A low magnification TEM image (Fig. 4.3a left, collected at pos. 1, see Figure 4.1b) gives an overview of particle morphologies present in fresh welding fumes. While bulky and fractal-like structures were frequent in larger particles ($> 0.5 \mu\text{m}$), the mode at 150 nm was mostly populated with simple chains (Fig. 4.3a middle, collected at pos. 2, see Fig. 4.1b). The mode at 40 nm consisted mostly of isolated particles (Fig. 4.3a right, collected at pos. 1, Fig. 4.1b) and small agglomerates.

The particle shown in Figure 4.3a (middle) contains all types of primary particles that were found in the different samples. The smallest primary particles ($< 15 \text{ nm}$) are spherical and monocrystalline, the intermediate ones ($15 \text{ nm} - 60 \text{ nm}$) are bounded by well developed crystal faces and the larger ones ($> 60 \text{ nm}$) show a preference of spherical shape and crystalline structure. The agglomerates found in the smaller mode (at 40 nm) consisted entirely of the smallest type of primary particles while the larger agglomerates showed no preferences.

Energy dispersive X-ray analysis (EDX) of different individual particles and agglomerates resulted in similar spectra with strong iron and oxygen K α -peaks (Fig. 4.3a, middle, Cu and C peaks result from the grid). The intensities of Ni and Cr peaks varied, Cr was frequently enriched (compared to the base and welding rod materials, Table 4.1) and Ni was often below the detection limit.

Single particle diffraction patterns of selected primary particles (e.g., Fig. 4.3b, collected at pos. 1, Fig. 4.1b) could all be indexed for a spinel structure. The lattice parameters corresponds to magnetite, Fe_3O_4 , which is compatible with the EDX analysis. The solid solutions between magnetite and nickel ferrite, NiFe_2O_4 , resp. chromite, FeCr_2O_4 , are complete, which have both spinel structure. Both Ni and Cr can thus be incorporated into magnetite in various amounts without resulting phase change. The traces of the crystal faces seen in Fig. 4.3a (middle) and 4.3b (left) are compatible with (100) and (111) of a cubo-octahedron, a shape, which is typical for nano-sized magnetite crystals (Faivre *et al.* 2005).

To verify whether the majority of airborne particles produced during welding consist of magnetite as is being suggested by the single particle analysis, and whether there are differences between the two welding processes used, powder diffraction patterns from large agglomerates and heavily laden TEM grids were recorded. In Figure 4.3c two examples are given. The powder diffraction pattern on the left belongs to the agglomerate shown in the middle (collected at pos. 3, Fig. 4.1b) and the powder diffraction pattern on the right has been recorded from a large cluster of agglomerates (collected at pos. 2, Fig. 4.1c). The patterns are virtually identical and are compatible to the calculated magnetite pattern (Fig. 4.3c right, calculated with version 3.04 of the jEMS software, Stadelmann 1987). The positions of the lines are identical to the simulation, the differences in intensity may be explained by the presence of Cr and Ni, which have a strong influence on certain structure factors.

About 1% of the particles appeared to have one or more primary particle covered by a thin layer of a material different from magnetite. All of the completely coated particles that were observed, were of spherical shape and their coating was on average 3 nm in thickness. The EDX analysis of the coated particles showed no significant differences compared to the uncoated particles. Dark field imaging of these particles (e.g., Fig. 4.3d, sample collected at pos. 1, see Fig. 4.1b) suggests that the coatings are amorphous.

The PM10 mass measurements mentioned earlier were analysed for their Ni content resulting in $3 \mu\text{g m}^{-3}$ at both work places, well below the mass limit (for Switzerland) of $50 \mu\text{g m}^{-3}$. However, these limits are set with the assumption of an even distribution of Ni throughout the particles. This is certainly the case for particles consisting entirely of magnetite. Whether this is true for coated particles as well could not be determined with our analytical setup and remains a question needing to be answered.

4. Conclusions

The measurement strategy for ultrafine particles suggested in this study allows to extend the standard evaluation procedures to gain a complete assessment of the exposure conditions met by the employees. The data on number concentrations, particle characteristics and surface composition should be used as guidelines for toxicological studies to gain further insight on the consequences of relevant exposure doses for occupational health.

There is no work interruption necessary to perform an assessment of the exposure situation performed according to the setup suggested in this study, since the in situ measurements are limited to one day and the equipment is not too bulky. The simultaneous use of the three online instruments revealed that the DiSC is the best candidate for a continuous monitoring device, with the only drawback being that it delivers only mean particle diameters and not complete size distributions. It is accurate, fast, highly mobile and capable of wireless communication. While both FMPS and SMPS are large and costly, the latter instrument has the added handicap of low time resolution (in the order of minutes).

References

- Antonini, J. M. (2003). Health effects of welding. *Crit. Rev. Toxicol.* 33:61-103.
- Brouwer, D. H., Gijbers, J. H. J. and Lurvink, M. W. M. (2004). Personal exposure to ultrafine particles in the workplace: Exploring sampling techniques and strategies. *Ann. Occup. Hyg.* 48:439-453.
- Chen, Y. Z., Shah, N., Braun, A., Huggins, F. E. and Huffman, G. P. (2005). Electron microscopy investigation of carbonaceous particulate matter generated by combustion of fossil fuels. *Energy Fuels* 19:1644-1651.
- Faivre, D., et al. (2005). Morphology of nanomagnetite crystals: Implications for formation conditions, *Am. Miner.*, 90, 1793-1800.
- Fierz, M., Scherrer, L. and Burtscher, H. (2002). Real-time measurement of aerosol size distributions with an electrical diffusion battery. *J. Aerosol. Sci.* 33:1049-1060.
- Fierz, M. and Burtscher, H. (2005). A portable diffusion size classifier, in *European Aerosol Conference*, W. Maenhaut, ed., Gent, Belgium, 423.
- Fierz, M., Kaegi, R. and Burtscher, H. (2007). Theoretical and experimental evaluation of a portable electrostatic TEM sampler. *Aerosol Science and Technology* 41:520-528.
- Grékula, A., Ristolainen, E., Tanninen, V. P., Hyvarinen, H. K. and Kalliomaki, P. L. (1986). Surface and Bulk Chemical-Analysis on Metal Aerosols Generated by Manual Metal Arc-Welding of Stainless-Steel. *J. Aerosol. Sci.* 17:1-&.
- Gunst, S., Weinbruch, S., Wentzel, M., Ortner, H. M., Skogstad, A., Hetland, S. and Thomassen, Y. (2000). Chemical composition of individual aerosol particles in workplace air during production of manganese alloys. *J. Environ. Monit.* 2:65-71.
- Harrison, R. M. and Yin, J. X. (2000). Particulate matter in the atmosphere: which particle properties are important for its effects on health? *Sci. Total Environ.* 249:85-101.
- Hoflich, B. L. W., Wentzel, M., Ortner, H. M., Weinbruch, S., Skogstad, A., Hetland, S., Thomassen, Y., Chaschin, V. P. and Nieboer, E. (2000). Chemical composition of individual aerosol particles from working areas in a nickel refinery. *J. Environ. Monit.* 2:213-217.
- Hoflich, B. L. W., Weinbruch, S., Theissmann, R., Gorzawski, H., Ebert, M., Ortner, H. M., Skogstad, A., Ellingsen, D. G., Drablos, P. A. and Thomassen, Y. (2005). Characterization of individual aerosol particles in workroom air of aluminium smelter potrooms. *J. Environ. Monit.* 7:419-424.
- Jenkins, N. T., Pierce, W. M. G. and Eagar, T. W. (2005). Particle size distribution of gas metal and flux cored arc welding fumes. *Weld. J.* 84:156S-163S.
- Kaegi, R. (2004). Chemical and morphological analysis of airborne particles at a tunnel construction site. *J. Aerosol. Sci.* 35:621-632.
- Ku, B. K. and Maynard, A. D. (2005). Comparing aerosol surface-area measurements of monodisperse ultrafine silver agglomerates by mobility analysis, transmission electron microscopy and diffusion charging. *J. Aerosol. Sci.* 36:1108-1124.
- Lorenzo, R., Kaegi, R., Gehrig, R. and Grob ty, B. (2006). Particle emissions of a railway line determined by detailed single particle analysis. *Atmos. Environ.* 40:7831-7841.
- Lorenzo, R., Kaegi, R., Gehrig, R., Scherrer, L. and Grob ty, B. (2007). A thermophoretic precipitator for the representative collection of atmospheric ultrafine particles for microscopic analysis. *Aerosol Science and Technology*: submitted.
- Mathis, U., Kaegi, R., Mohr, M. and Zenobi, R. (2004). TEM analysis of volatile nanoparticles from particle trap equipped diesel and direct-injection spark-ignition vehicles. *Atmos. Environ.* 38:4347-4355.
- Maynard, A. D. (2000). Overview of methods for analysing single ultrafine particles. *Philos. Trans. R. Soc. Lond. Ser. A-Math. Phys. Eng. Sci.* 358:2593-2609.
- Maynard, A. D., Ito, Y., Arslan, I., Zimmer, A. T., Browning, N., Nicholls, A. and Nicholls, A. (2004). Examining elemental surface enrichment in ultrafine aerosol particles using analytical scanning transmission electron microscopy. *Aerosol Science And Technology* 38:365-381.
- Maynard, A. D. and Kuempel, E. D. (2005). Airborne nanostructured particles and occupational health. *J. Nanopart. Res.* 7:587-614.
- National Institute for Occupational Safety and Health, (NIOSH) (2006). Approaches to Safe Nanotechnology: An Information Exchange with NIOSH. Approaches to Safe Nanotechnology: An Information Exchange with NIOSH *online resource*: <http://www.cdc.gov/niosh/topics/nanotech/safenano/>.
- Seaton, A. and Donaldson, K. (2005). Nanoscience, nanotoxicology, and the need to think small. *Lancet* 365:923-924.
- Stadelmann, P. A. (1987). EMS - A Software Package For Electron-Diffraction Analysis And HREM Image Simulation In Materials Science. *Ultramicroscopy* 21:131-145.

- Vincent, J. H. (2005). Health-related aerosol measurement: a review of existing sampling criteria and proposals for new ones. *J. Environ. Monit.* 7:1037-1053.
- Wiesner, M. R., Lowry, G. V., Alvarez, P., Dionysiou, D. and Biswas, P. (2006). Assessing the risks of manufactured nanomaterials. *Environ. Sci. Technol.* 40:4336-4345.
- Zimmer, A. T., Baron, P. A. and Biswas, P. (2002). The influence of operating parameters on number-weighted aerosol size distribution generated from a gas metal arc welding process. *J. Aerosol. Sci.* 33:519-531.
- Zimmer, A. T. (2002). The influence of metallurgy on the formation of welding aerosols. *J. Environ. Monit.* 4:628-632.

4.3 Technical Details

4.3.1 Pilot study

A first sampling campaign in the context of welding fumes took place in March 2005. The company that hosted our measurements produces aluminium railway coaches and applies Al gas metal welding (GMAW) techniques (see Table 4.2 for details on the materials). As in the study documented in the previous chapter (4.2) aerosol measurement specialists from the Swiss National Accident Insurance Fund (SUVA) were part of the team.

Sampling site and instrumentation

Welding robots and work places for manual welding are collocated in the same premises. The manufacturing hall measures approximately 95x60x12 m (length/width/height) and is subdivided in four alleys (Fig. 4.4), of which each one has an individual ventilation system. The alleys are separated by about 2.5 m high welding curtains.

The welding robots build the chassis of the railway coaches which are 20 - 30 m long, depending on the type. Robots are supervised at all times but the operators usually keep a few metres distance to the welding rod.

Manual welding is performed on the coachwork and on details of the chassis, where the robots cannot reach. Since in the premises work is being done on at least seven coaches simultaneously, manual and automated welding are applied in parallel but not on the same coach at once.

The measurement equipment was set up in the middle of and about two metres to the side of a welding robot (see Fig. 4.4). Additionally, one sample for subsequent TEM analysis was taken directly from fresh welding fumes at a manual work place (distance to the arc: <0.5 m).

Particle size distributions were measured online with an SMPS (TSI Model 3034, 3 min time resolution, size range: 10 - 500 nm) and the particle number concentration with an electrical diffusion battery (EDB, 1 s time resolution; Fierz *et al.* 2002). For subsequent offline single particle analysis samples were collected with an electrostatic (ESS, Fierz *et al.* 2007) and a thermophoretic sampling device (TPS, Lorenzo *et al.* 2007). Samples were collected on C coated Ni grids (TPS), C coated Cu grids (ESS) and Cu grids with a lacy C film (ESS). Additionally, particles were collected on Nuclepore® polycarbonate filters (0.4 µm pore size) with a mini Partisol air sampler (Rupprecht & Patashnick, Model 2100) for subsequent analysis on a SEM.

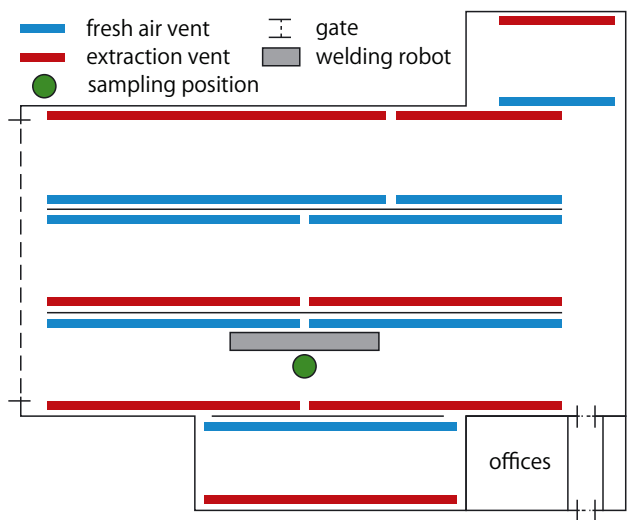


Fig. 4.4: Details of the measuring site for the pilot study.

Online measurements - lessons learned

While the operation of the EDB was not problematic, the low time resolution of the SMPS turned out to be a handicap. Due to the length of the chassis the distance of the welding robot to the inlet position varies strongly. Accordingly, particle number concentrations and size distributions at the inlet position varied on shorter time scales than the SMPS could resolve.

Figure 4.5 illustrates the effect of changing conditions. During the scan for the blue curve the welding robot remained stationary close to the position of the SMPS' inlet resulting in a smooth line with a mode at 25 nm. While the scan for the red curve was in progress, the welding robot was working its way along the length of the chassis and, thus, passing by the inlet of the SMPS. The resulting particle size distribution is a mixture of aerosols with a different history (dilution) and therefore not representative for the source.

Consequently, the sample air for the SMPS needs to be homogenised before measuring in order for the instrument to deliver size distributions that are characteristic for a particle source. Alternatively, a faster instrument, such as an FMPS, may be used. Although it is by no means certain that the advantages of the FMPS compared to the SMPS rectify the larger price tag.

Table 4.2

Principal alloys present in the aluminium types used for GMAW. The shield gas consists of 95% Ar and 5% He. The diameter of the welding rod is 0.8 mm. Surfaces were cleaned.

Material Number	Base Material	Welding Rod
	3.3547 ^a	Al Mg 4.5 Mn ^b
Mg	4.00 - 4.90%	4.30 - 5.20%
Mn	0.40 - 1.00%	0.50 - 1.00%
Cr	0.05 - 0.25%	0.05 - 0.25%
Fe	< 0.40%	< 0.40%
Si	< 0.40%	< 0.20%
Zn	< 0.25%	< 0.25%

^a Traces (< 0.15%) of Cu, Ti and other elements are tolerated.

^b Traces (< 0.15%) of Cu, Ti and other elements are tolerated, Be <0.0008%.

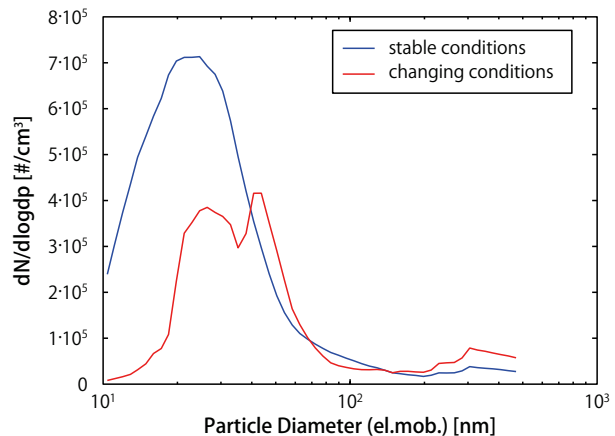


Fig. 4.5: Comparison of SMPS spectra recorded during stable conditions (blue) and shifting conditions during the scan (red).

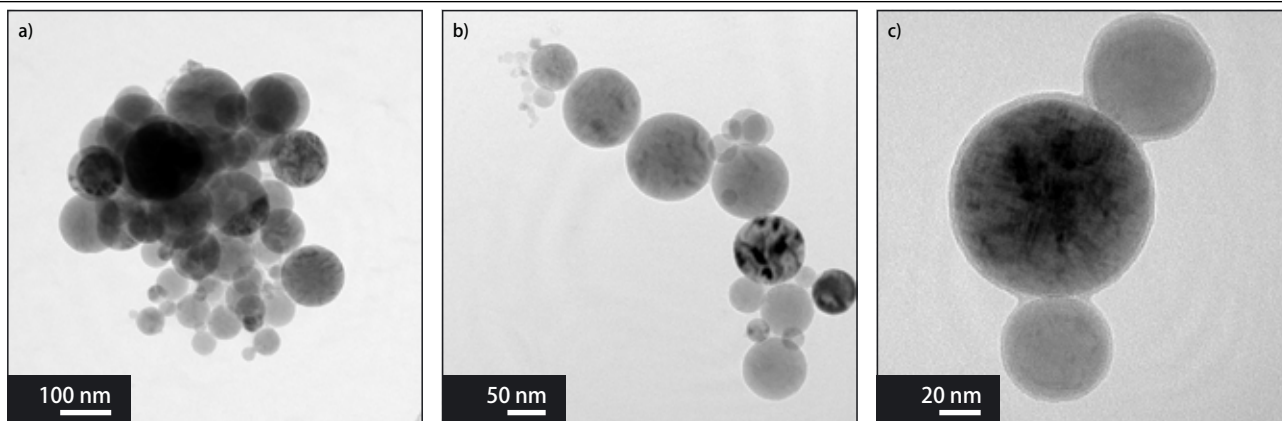


Fig. 4.6: Examples of welding fume particles produced during Al GMAW. The TEM images were taken from samples collected with the thermophoretic precipitator. While large clusters (a) are frequently found among the larger agglomerates, most particles are chain-like structures (b). At a closer look most particles are covered with a thin seamless outer layer up to 5 nm in thickness.

Offline measurements

Analysis of the particle samples with a TEM revealed that all primary particles - with very few exceptions - are spherical in shape. Diameters of the primary particles vary from around 5 nm up to more than 150 nm. Isolated spheres or small aggregates of two to three primary particles were seldom found.

In general, two particle types could be distinguished based on their morphology: clusters and chains. While clusters of primary particles (Fig. 4.6a) were found foremost among the larger particles (projected equivalent diameter >150 nm) chains (Fig. 4.6b&c) were found among all size fractions.

On most particles a thin outer layer could be observed. Up to 5 nm in thickness it appeared less dense than the primary particles it surrounded. Since all of the primary particles seemed to be crystalline the varying contrasts are due to different orientation of their lattices relative to the electron beam. The fact that the outer layer was always brighter than the particle it surrounded is an indicator for an amorphous structure. This assumption is backed by the observation that the outer layer was always seamless, even when covering an agglomerate of primary particles (as in Fig. 4.6c).

The EDX analysis of the agglomerates showed primarily Al and O. Mn and Mg was rarely found. Based on the addi-

tional information from the elemental analysis, it may be suspected that the primary particles consist of pure crystalline Al and the outer layer of amorphous Al_2O_3 . However, further analysis would be required to verify this theory.

4.3.2 Bag sampling device

Based on the experiences of the pilot study it was decided to build a bag sampling system to complement the SMPS. Due to a more favourable volume to surface ratio large volumes are preferred for sub-micron particle measurements. However, large volumes need more time to be filled and, accordingly, particle losses are increasing again. Additionally, while air is being drawn from the bag for the measurements, conditions should stay stable. Thus, the volume needed for the SMPS scans should be small compared to the total bag volume.

As a basis for the assessment of the bag size required, formulas 8-78 and 8-79 from Baron and Willeke (2001) were used. Calculations showed, that a volume of 110 litres would suffice for up to five SMPS scans. In Figure 4.7 size dependent particle losses for up to ten SMPS scans (corresponds to 30 min) are shown (based on MathCAD calculations, see Appendix A.4.1 for details).

The bag material needs to be electroconductive in order to prevent accumulation of electric charges on the surface

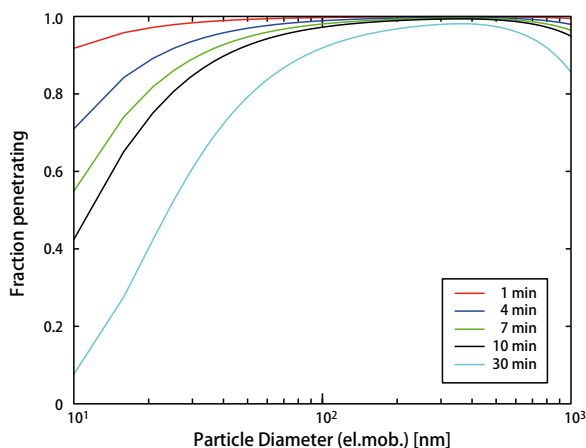


Fig. 4.7: Calibration chart for the particle losses of the bag sampler. These curves need to be tweaked (as ensemble) to specific aerosols and conditions. Accordingly, several scans from each bag filling need to be done to extract the exact parameters.

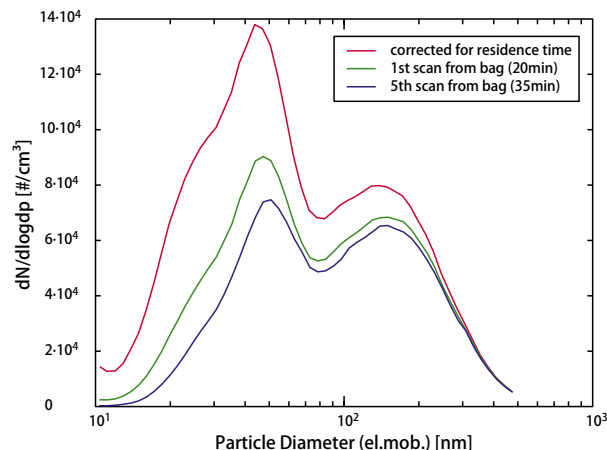


Fig. 4.8: Illustration of particle losses due to diffusion inside the bag sampler. red: particle size distribution corrected for the losses; green: first SMPS scan after the bag has been filled; blue: last (5th) SMPS scan off of the bag.

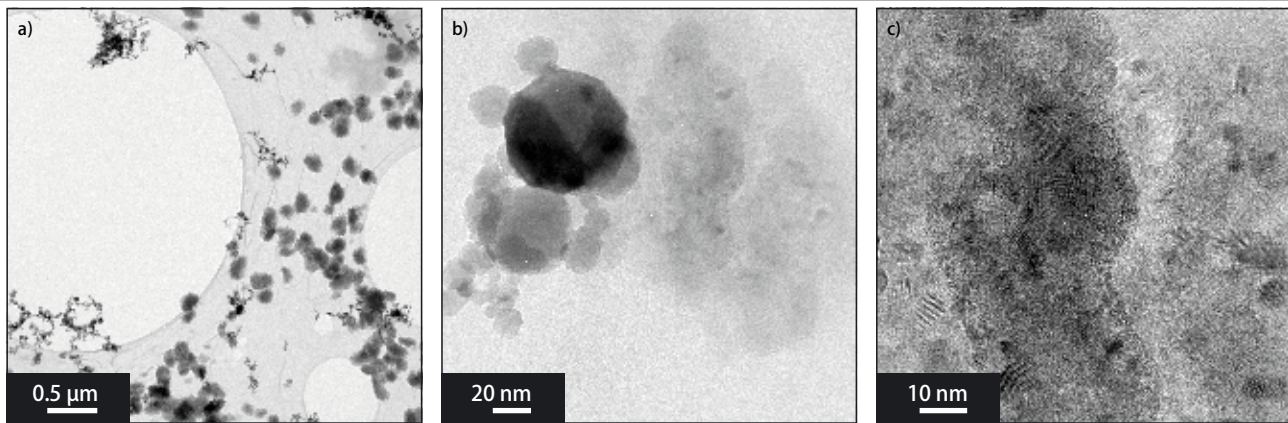


Fig. 4.9: Images of a contaminated grid (artefacts from the manufacturing process at the factory from Plano) used for the welding fumes campaign. a: The dirt particles can not be distinguished from the welding fume particles by means of image analysis. Therefore, no quantification of the results from the single particle analysis was attempted. b: Mixed welding fume - dirt particle. c: Close-up of the dirt from b.

and the subsequent increase of electrophoretic losses. The material used for the bag is called “pink poly” (Sirel plc, ESD Control) and is normally applied for packaging of electronic components.

To fill the bag passively (to prevent contamination by the pump), a casing built from aluminium profiles and sheets and Plexiglass® walls has been designed (components by Phoenix Mecano, for the plans see Appendix A.4.2 and A.4.3). To connect the bag with the casing a stainless steel multi purpose inlet has been designed and built in-house (plans: Appendix A.4.4).

Calibration experiments were performed at a roadside measurement station (NABEL station in Härkingen) with two SMPS in parallel - one measuring directly and the other drawing air from the bag sampling system. The calibration chart shown in Figure 4.7 was confirmed by these experiments.

In Figure 4.8 the particle size distribution previously shown in Figure 4.2d is compared to the raw data from the 1st and 5th SMPS scan off of the same bag filling. The formula used for the calibration chart is valid for standard conditions only and does not consider parameters such as relative humidity. Therefore, based on three to five SMPS scans from air drawn from the bag are used to match the present parameters and tweak the calibration chart accordingly.

4.3.3 Additional information

Contaminated TEM grids

Originally, it was planned to quantify the results of the TEM analysis. However, the grids used turned out to be contaminated by artefacts from the production process (see Fig. 4.9a). Although dirt particles - CaS residua - are clearly distinguishable from welding particles due to the different morphology, the differing characteristics were not distinct enough to be implemented successfully in a image analysis routine.

On the level of individual welding fume agglomerates, residua were often difficult to distinguish when overlapping with welding particles (see Fig. 4.9b). This was partly due to the crystalline nature of the residua (see Fig. 4.9c) acting as a camouflage, frequently requiring EDX analysis to gain certainty about the origin of the particle.

Although residua were present on the entire grids, their frequency varied strongly. Therefore, particle analysis was possible on some portions of the grid limiting the restrictions of the analysis to the quantification of the TEM results.

Crystallographic analysis

On the basis of the ring patterns and the results of numerous EDX analyses the basic material (Magnetite) and, thus, the crystal structure of the particles (Fd-3m,

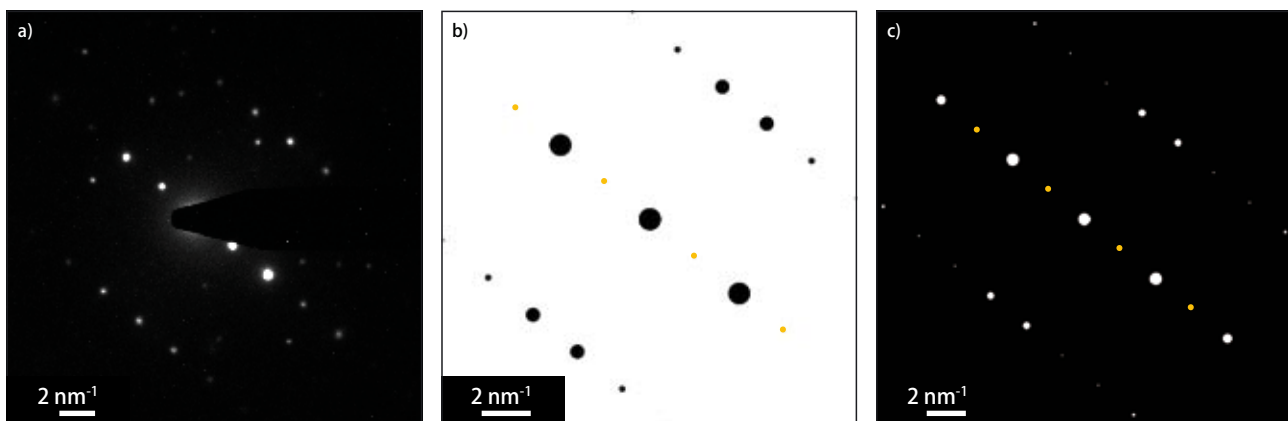


Fig. 4.10: Diffraction pattern from images 4.3c and possible interpretations based on jEMS simulations. a: Original pattern as registered in the TEM. b: Diffraction pattern from Fe_3O_4 (Magnetite, Fd-3m, centred) in [105] orientation. c: Diffraction pattern of $\text{Fe}_{0.99}\text{Fe}_{1.97}\text{Cr}_{0.03}\text{Ni}_{0.01}\text{O}_4$ (Fe-Cr-Ni spinel, Magnetite, Fd-3m, centred) in [105] orientation. The positions of the reflections in b & c are identical and differ only in their intensities. (The yellow dots are reflections due to doubly diffracted beams.)

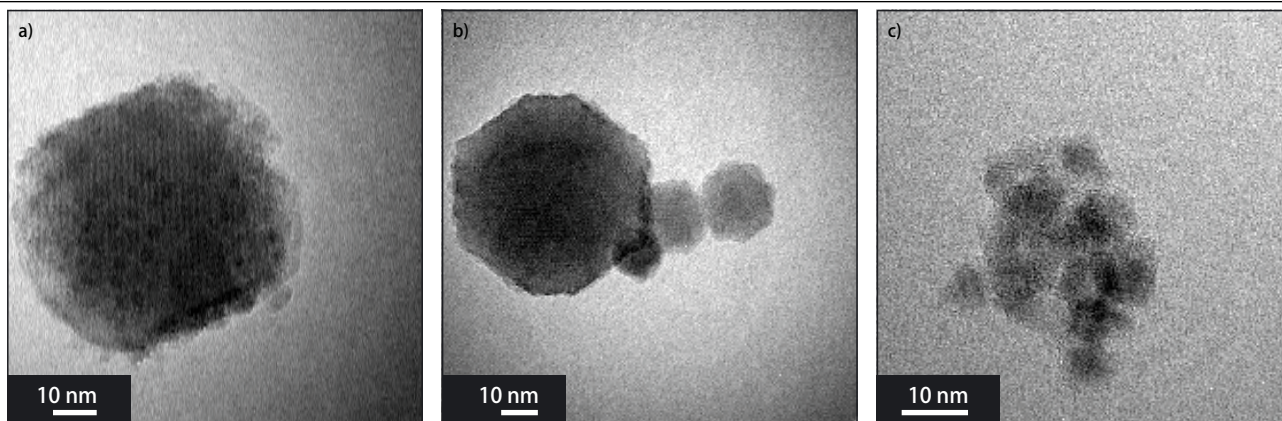


Fig. 4.11: Special particles. a: Welding fume particle with traces of Mn. It's monocrystalline but has a very irregular surface. b) The large (monocrystalline) particle on the left appears to be in transition from an edge to a spherical shape. It is considerably thicker in the middle than on the edges. c: Agglomerate of very small, crystalline primary particles. The smallest ones are <3 nm in diameter.

centred) was identified. However, the Fe_3O_4 spinel contains frequently traces of Cr, Ni or Mn. Since these elements are also present in the welding materials used (see Table 4.1) they were found in particles as well. The effect of these alloys on the crystal structure is not obvious. While the position of the reflections remains unchanged - bound to the spinel structure - their intensity varies with the content of the alloys.

Figure 4.10a shows the single particle diffraction pattern previously seen in Figure 4.3c. Using the jEMS software (Stadelmann 1987) it was attempted to determine the composition of the particle. In Figure 4.10b the simulated diffraction pattern of Fe_3O_4 ([105] orientation) is shown and it matches the diffraction pattern of the single particle quite well. However, adding traces of Cr and Ni to the crystal leads to the diffraction pattern shown in Figure 4.10c (simulated for the [105] orientation) which matches the original pattern equally well.

References

- Baron, P. A. and Willeke, K., eds. (2001). *Aerosol Measurements: Principals, Techniques, and Applications*. John Wiley & Sons, New York.
- Fierz, M., Scherrer, L. and Burtscher, H. (2002). Real-time measurement of aerosol size distributions with an electrical diffusion battery. *J. Aerosol. Sci.* 33:1049-1060.
- Fierz, M., Kaegi, R. and Burtscher, H. (2007). Theoretical and experimental evaluation of a portable electrostatic TEM sampler. *Aerosol Science and Technology* 41:520-528.
- Lorenzo, R., Kaegi, R., Gehrig, R., Scherrer, L. and Grob ty, B. (2007). A thermophoretic precipitator for the representative collection of atmospheric ultrafine particles for microscopic analysis. *Aerosol Science and Technology*: submitted.
- Stadelmann, P. A. (1987). EMS - A Software Package For Electron-Diffraction Analysis And HREM Image Simulation In Materials Science. *Ultramicroscopy* 21:131-145.

Additional observations

A closer look at individual particles emphasises the need for additional detailed single particle analysis. A few "arguments" are shown in Figure 4.11. The particle seen in Figure 4.11a contains traces of Mn. Whether this is the explanation to the black dots or whether the Mn is incorporated into the bulk structure could not be determined. Remarkable, however, that the particle is monocrystalline and the black dots seem to have the same structure.

The large particle on the left shown in Figure 4.11b appears to be in a transition from an angled crystal to a spherical shape. While it is monocrystalline it is considerably thicker in the middle than on the edges.

In Figure 4.11c an agglomerate of representatives from the smallest primary particles found on the TEM samples. All of them are crystalline and are seen in differing orientations. The smallest ones are roughly 3 nm in diameter.



Outlook

«We have no evidence - just a theory that happens to fit the facts.»

Spock, Star Trek VI

5 Outlook

Sincere executed scientific projects usually raise more new questions than they were actually able to answer. But that's the prize one pays, or rather gets awarded for broadening ones horizon.

Following are a few project ideas and questions that surfaced during the investigations described in the previous three chapters (and the ones that were not meant for publication).

Particulate emissions of...

The results of the study on the particulate emissions of a railway line (chapter 2) showed that allegedly small sources may not be as unimportant as originally thought. Meanwhile, the applied method of CCSEM in combination with the custom built PM10 sampling devices proved to live up to the standards set by gravimetric methods. Moreover, CCSEM delivers information on the particle morphology which may serve as additional means for separating sources (Kaegi 2004).

Based on this method it should be possible to (at least) estimate the contributions of different pollutants to the total PM10 burden of (e.g.) a small village. It would be interesting to compare the contributions of (e.g.) a power plant (coal), waste incinerator, railway line and a highway (abrasion of tires, brakes and pavement). Since it is comparably easy for stationary sources to drastically reduce their particulate emissions results of such measurements could possibly put the on-road traffic under additional pressure.

Atmospheric particles

One of the projects which got put on hold due to more "urgent" studies was the investigation on atmospheric particles. While originally thought as a real-life test of the TPS side by side with the ESS, the samples collected at the high alpine research station on the Jungfraujoch revealed interesting particle structures and a wealth of particles of the free molecular regime (see Fig. 3.15 and Appendix A.3.3).

A major challenge posed by such a study is gaining access to and developing expertise on the analytical techniques needed. Due to the sensitivity of the particles conventional TEM is not applicable. Cryo-TEM, EELS or SAM might shed some light on the complicated, layered structure of the particles.

Research on particulate enclosures in ice cores is just beginning. It should be interesting to look into the process on which particles get "washed" out and are conserved in the glacier ice. A comparative study on (pre-snowfall) atmospheric particles, condensation nuclei in snow flakes (sample of fresh snow), firn and ice cores might offer some clues.

Occupational safety and health

The study described in chapter 4 is a solid basis for future investigations on this subject. An ideal follow-up project would involve *in situ in vitro* studies. Welding fumes are well suited since the particles produced have all similar characteristics, high number concentrations are fairly common and nothing unusual for employees to be subject to.

Additional questions concerning the structure of the welding particles are still open. The coating of the particles (see as well section 4.3.1) is still not identified and obviously present on particles produced with different base materials. Since surface chemistry plays an important role in the particle-cell interaction this is certainly a significant question to be answered.

A portable, highly mobile TPS would be an additional asset for studies of working environments. A miniaturised precipitator, stripped of the fan and reduced to minimal dimensions, should be constructed such that it would sit on the shoulder of a worker without obstructing. A regulated pump, the battery pack and the hardware to control the temperature gradient as well as a data logger should be built small enough to fit detached from the precipitator on a belt, maybe on a vest for convenience.

Reference

Kaegi, R. (2004). Chemical and morphological analysis of airborne particles at a tunnel construction site. *J. Aerosol Sci.* 35:621-632.



Appendix

- Definitions
- Chapter 2
- Chapter 3
- Chapter 4

«Hold tight lassy, it get's bumpy from here.»

Scotty, Star Trek IV

A.1 Abbreviations and definitions

<i>Accumulation Mode</i>	Particles with aerodynamic equivalent diameter between 100 nm and 1 μm .	<i>MFC</i>	Mass Flow Controller
<i>Aerosol</i>	An assembly of liquid or solid (or mixed) particles suspended in a gaseous medium long enough to be measured or observed. Usually <100 μm .	<i>NABEL</i>	Nationales Beobachtungsnetz Luftfremdstoffe, national monitoring network for air pollution.
<i>AEM</i>	Analytic Electron Microscope	<i>Nanoparticle (nano-sized particle)</i>	Particle with at least one dimension <100 nm.
<i>AFM</i>	Atomic Force Microscope	<i>NEXAFS</i>	Near Edge X-ray Absorption Fine Structure
<i>Aitken Mode</i>	Particles with aerodynamic equivalent diameter between 10 nm and 100 nm.	<i>Nucleation Mode</i>	Particles with aerodynamic equivalent diameter between 1 nm and 10 nm.
<i>CCSEM</i>	Computer Controlled Scanning Electron Microscope	<i>PID</i>	Proportional Integral Derivative
<i>Coarse Mode</i>	Particles with aerodynamic equivalent diameter between 1 μm and 10 μm .	<i>PM_{xy}</i>	Particulate matter smaller xy μm .
<i>Cunningham Correction Factor C_c</i>	Correction factor needed to describe the physical behaviour of particles from the transition regime (see section 1.1.1).	<i>SAED</i>	Selected Area Electron Diffraction
<i>Continuum Regime</i>	Particles with a Knudsen Number $Kn \gg 1$.	<i>SAM</i>	Scanning Auger Microscopy
<i>CPC</i>	Condensation Particle Counter (see section 1.2.1)	<i>SEM</i>	Scanning Electron Microscope
<i>DiSC</i>	Diffusion Size Classifier (see section 1.2.1)	<i>Slip Flow Regime</i>	Alternative name for the transition regime.
<i>DMA</i>	Differential Mobility Analyser (see section 1.2.1)	<i>SMPS</i>	Scanning Mobility Particle Sizer (see section 1.2.1)
<i>DMPS</i>	Differential Mobility Particle Sizer	<i>STXM</i>	Scanning Transmission X-ray Microscopy
<i>EDB</i>	Electrical Diffusion Battery (see section 1.2.1)	<i>TEM</i>	Transmission Electron Microscope
<i>EDX</i>	Energy Dispersive X-ray spectroscopy	<i>TEOM</i>	Tampered Element Oscillating Microbalance
<i>EDXRF</i>	Energy Dispersive X-Ray Fluorescence	<i>Thermophoresis</i>	Literally: "Carried by temperature". Particles flying through a temperature gradient get gradually pushed towards the cooler side.
<i>Electrophoresis</i>	Literally: "Carried by electricity". Charged particles passing through an electric field are deflected according to their polarity.	<i>TPS</i>	ThermoPhoretic Sampling device
<i>ESEM</i>	Environmental Scanning Electron Microscope	<i>Transition Regime</i>	Particles with a Knudsen Number of the range $\approx 0.25 \leq Kn \leq 20$.
<i>ESS</i>	ElectroStatic Sampling device	<i>Ultrafine particle (UFP)</i>	Particle of the accumulation or Aitken mode (<100 nm).
<i>FMPS</i>	Fast Mobility Particle Sizer (see section 1.2.1)		
<i>Fine Particle (FP)</i>	Particles of the accumulation mode (100 nm - 1 μm).		
<i>Free Molecular Regime</i>	Particles with a Knudsen Number $Kn \ll 1$.		
<i>GMAW</i>	Gas Metal Arc Welding		
<i>IA</i>	Image Analysis		
<i>ICP-MS</i>	Inductively Coupled Plasma Mass Spectroscopy		
<i>Knudsen Number (Kn)</i>	Relates the molecular mean free path to the particle dimension (see section 1.1.1).		

A.2 Additional information on Chapter 2

A.2.1 Matlab sheets

sbb.m

```
%sbb.m
%Works through the EDX Data: filters particles by size and composition and calculates mass contributions

%Parameter definition
mod=0;
binsize=0.3; %width of the size bins
minsize=0.5; %smallest particle diameter allowed (optical eq.)
maxsize=10; %largest particle diameter allowed (optical eq., for size bins)
aero_max=15; %largest particle diameter allowed (aerodynamic eq.)
upscaler=1/(0.96*0.0020); %scaling for m3 and total filter area
pureAl=zeros(1,3);
AlCa =zeros(1,3);
CaS =zeros(1,3);
NaK =zeros(1,3);
noAlk=zeros(1,3);
sec =zeros(1,3);

%filters particles (EDX data) by size and composition
sbb_10_El;
sbb_10E_El;
sbb_10W_El;
sbb_36_El;
sbb_120_El;

%calculates masses
massFe10m=(massFe10+massFe10E+massFe10W)/3;
massFe10mtot=(massFe10tot+massFe10Etot+massFe10Wtot)/3;
massSi10m=(massSi10+massSi10E+massSi10W)/3;
massSi10mtot=(massSi10tot+massSi10Etot+massSi10Wtot)/3;
massAl10m=(massAl10+massAl10E+massAl10W)/3;
massAl10mtot=(massAl10tot+massAl10Etot+massAl10Wtot)/3;
massCa10m=(massCa10+massCa10E+massCa10W)/3;
massCa10mtot=(massCa10tot+massCa10Etot+massCa10Wtot)/3;
massS10m=(massS10+massS10E+massS10W)/3;
massS10mtot=(massS10tot+massS10Etot+massS10Wtot)/3;

%average of the 10m sites
sum_10m=round((sum_10*1.1204+sum_10E*1.0309+sum_10W*1.005)/3);

Si=[sum_10(1)*1.1204 sum_10E(1)*1.0309 sum_10W(1)*1.005];
Al=[sum_10(2)*1.1204 sum_10E(2)*1.0309 sum_10W(2)*1.005];
Fe=[sum_10(3)*1.1204 sum_10E(3)*1.0309 sum_10W(3)*1.005];
Ca=[sum_10(4)*1.1204 sum_10E(4)*1.0309 sum_10W(4)*1.005];
S=[sum_10(5)*1.1204 sum_10E(5)*1.0309 sum_10W(5)*1.005];

%calculates error margins
rel_fehler=[std(Si)/sum(Si) std(Al)/sum(Al)...
std(Fe)/sum(Fe) std(Ca)/sum(Ca) std(S)/sum(S)]*3;

clear Si Al Fe Ca S;

%summarises the data for the "emission profile"
Si=round([sum_10m(1) sum_36(1) sum_120(1)*1.0526]);
Al=round([sum_10m(2) sum_36(2) sum_120(2)*1.0526]);
Fe=round([sum_10m(3) sum_36(3) sum_120(3)*1.0526]);
Ca=round([sum_10m(4) sum_36(4) sum_120(4)*1.0526]);
S= round([sum_10m(5) sum_36(5) sum_120(5)*1.0526]);

clear binsize minsize maxsize upscaler aero_max;
```

sbb_XX_El.m

```

% sbb_XX_El.m
% Reads the EDX data from the txt files, filters by particle size
% and composition and calculates individual masses.

% getting data
% AvgDiam
sbb10(:,1)=dlmread('filename.txt','\t',[13 13 3059 13]);
% Shape
sbb10(:,2)=dlmread('filename.txt','\t',[13 18 3059 18]);
% Si
sbb10(:,3)=dlmread('filename.txt','\t',[13 25 3059 25]);
% Fe
sbb10(:,4)=dlmread('filename.txt','\t',[13 38 3059 38]);
% Ca
sbb10(:,5)=dlmread('filename.txt.txt','\t',[13 32 3059 32]);
% S
sbb10(:,6)=dlmread('filename.txt.txt','\t',[13 28 3059 28]);
% Al
sbb10(:,7)=dlmread('filename.txt ','\t',[13 24 3059 24]);
% Lp
sbb10(:,8)=dlmread('filename.txt ','\t',[13 14 3059 14]);
% Area
sbb10(:,9)=dlmread('filename.txt ','\t',[13 15 3059 15]);
% Frame
sbb10(:,10)=dlmread('filename.txt.txt','\t',[13 1 3059 1]);
% Part.#
sbb10(:,11)=dlmread('filename.txt.txt','\t',[13 2 3059 2]);
% Na
sbb10(:,12)=dlmread('filename.txt.txt','\t',[13 23 3059 23]);

% subtracting background
bgrd=[16 4 7 14 18 16]; % [Si Fe Ca S Al Na]
zeilen=length(sbb10(:,1));
limit(1)=3*(bgrd(1)/15)^0.5+bgrd(1);
limit(2)=3*(bgrd(2)/15)^0.5+bgrd(2);
limit(3)=3*(bgrd(3)/15)^0.5+bgrd(3);
limit(4)=3*(bgrd(4)/15)^0.5+bgrd(4);
limit(5)=3*(bgrd(5)/15)^0.5+bgrd(5);
limit(6)=3*(bgrd(6)/15)^0.5+bgrd(6);
for i=1:zeilen
    Si=sbb10(i,3);
    Fe=sbb10(i,4);
    Ca=sbb10(i,5);
    S =sbb10(i,6);
    Al=sbb10(i,7);
    Na=sbb10(i,12);
    if Si<=limit(1)
        sbb10(i,3)=0;
    else
        sbb10(i,3)=Si-bgrd(1);
    end
    if Al>limit(5)
        sbb10(i,7)=Al-bgrd(5);
    else
        sbb10(i,7)=0;
    end
    if Fe<=limit(2)
        sbb10(i,4)=0;
    else
        sbb10(i,4)=Fe-bgrd(2);
    end
    if Ca<=limit(3)
        sbb10(i,5)=0;
    else
        sbb10(i,5)=Ca-bgrd(3);
    end
    if S<=limit(4)
        sbb10(i,6)=0;
    else
        sbb10(i,6)=S-bgrd(4);
    end
    if Na<=limit(6)
        sbb10(i,12)=0;
    else
        sbb10(i,12)=Na-bgrd(6);
    end
end
end

```

```

%builds element specific matrices [AvgDiam Shape NetInt>0 Vol.Ell.]
j=0; k=0; l=0; m=0; p=0; %Si Fe Ca S Al
toosmall=0; nokat=0;
Si10=0; Fe10=0; Ca10=0; S10=0; Al10=0; nokat10=0;
for i=1:zeilen
    if sbb10(i,1)>=0.5
        work=sbb10(i,3:7);
        winner=max(work);
        loser=0;
        switch winner
            case loser;
                nokat=nokat+1;
                nokat10(nokat,1)=sbb10(i,1);
                nokat10(nokat,2)=sbb10(i,10);
                nokat10(nokat,3)=sbb10(i,11);
            case sbb10(i,3)
                if sbb10(i,7)>mod*bgrd(5)
                    p=p+1;
                    a=sbb10(i,8)/2;
                    Al10(p,2)=sbb10(i,2);
                    Al10(p,3)=sbb10(i,7);
                    Al10(p,4)=(2*sbb10(i,9))^2/(3*a*pi);
                    Al10(p,1)=2*(3*Al10(p,4)/(4*pi))^(1/3);
                    if sbb10(i,5)>0
                        AlCa(1)=AlCa(1)+1;
                    else
                        if sbb10(i,3)>0
                            NaK(1)=NaK(1)+1;
                        else
                            noAlk(1)=noAlk(1)+1;
                        end
                    end
                    %calculates the volume of a prolate ellipsoid
                    %semi major axis=LProj/2 & equiv. proj.area, rotated around
                    %LProj
                else
                    j=j+1;
                    a=sbb10(i,8)/2;
                    Si10(j,2)=sbb10(i,2);
                    Si10(j,3)=sbb10(i,3);
                    Si10(j,4)=(2*sbb10(i,9))^2/(3*a*pi);
                    Si10(j,1)=2*(3*Si10(j,4)/(4*pi))^(1/3);
                end
            case sbb10(i,4)
                k=k+1;
                a=sbb10(i,8)/2;
                Fe10(k,2)=sbb10(i,2);
                Fe10(k,3)=sbb10(i,4);
                Fe10(k,4)=(2*sbb10(i,9))^2/(3*a*pi);
                Fe10(k,5)=sbb10(i,1);
                Fe10(k,1)=2*(3*Fe10(k,4)/(4*pi))^(1/3);
            case sbb10(i,5)
                l=l+1;
                a=sbb10(i,8)/2;
                Ca10(l,2)=sbb10(i,2);
                Ca10(l,3)=sbb10(i,5);
                Ca10(l,4)=(2*sbb10(i,9))^2/(3*a*pi);
                Ca10(l,1)=2*(3*Ca10(l,4)/(4*pi))^(1/3);
                if sbb10(i,8)>0
                    CaS(1)=CaS(1)+1;
                    CaS10(1,1)=sbb10(i,5);
                    CaS10(2,1)=sbb10(i,6);
                end
            case sbb10(i,6)
                if sbb10(i,5)>0
                    l=l+1;
                    a=sbb10(i,8)/2;
                    Ca10(l,2)=sbb10(i,2);
                    Ca10(l,3)=sbb10(i,5);
                    Ca10(l,4)=(2*sbb10(i,9))^2/(3*a*pi);
                    Ca10(l,1)=2*(3*Ca10(l,4)/(4*pi))^(1/3);
                    CaS(1)=CaS(1)+1;
                    CaS10(1,1)=sbb10(i,5);
                    CaS10(2,1)=sbb10(i,6);
                    sec(1)=sec(1)+1;
                end
            end
        end
    end
end

```

```

else
    m=m+1;
    a=sbb10(i,8)/2;
    S10(m,2)=sbb10(i,2);
    S10(m,3)=sbb10(i,6);
    S10(m,4)=(2*sbb10(i,9))^2/(3*a*pi);
    S10(m,1)=2*(3*S10(m,4)/(4*pi))^(1/3);
end
case sbb10(i,7)
    p=p+1;
    a=sbb10(i,8)/2;
    Al10(p,2)=sbb10(i,2);
    Al10(p,3)=sbb10(i,7);
    Al10(p,4)=(2*sbb10(i,9))^2/(3*a*pi);
    Al10(p,1)=2*(3*Al10(p,4)/(4*pi))^(1/3);
    pureAl(1)=pureAl(1)+1;
    if sbb10(i,3)>0
        NaK(1)=NaK(1)+1;
    end
otherwise
    nokat=nokat+1;
    nokat10(nokat,1)=sbb10(i,1);
    nokat10(nokat,2)=sbb10(i,10);
    nokat10(nokat,3)=sbb10(i,11);
end
else
    toosmall=toosmall+1;
end
end

%histograms [bin# vol.ellipsoid vol.sphere]
SizeFe10=sbb_hist_El(Fe10,binsize,minsize);
SizeCa10=sbb_hist_El(Ca10,binsize,minsize);
SizeAl10=sbb_hist_El(Al10,binsize,minsize);
SizeSi10=sbb_hist_El(Si10,binsize,minsize);
SizeS10=sbb_hist_El(S10,binsize,minsize);

%calculates masses
nob=ceil((maxsize-minsize)/binsize);
kor=upscaler*1.104; %corrects the flow to 4l/min
toolarge=0;
massFe10=zeros(2,nob);
massFe10tot=zeros(1,2);
u=ceil((aero_max*(5.5^-0.5)-0.5)/0.3);
for i=1:length(SizeFe10)
    bin=SizeFe10(i,1);
    massFe10(1,bin)=massFe10(1,bin)+SizeFe10(i,2)*5.5;
    massFe10(2,bin)=massFe10(2,bin)+SizeFe10(i,3)*5.5;
    if bin<=u
        massFe10tot(1)=massFe10tot(1)+SizeFe10(i,2)*5.5;
        massFe10tot(2)=massFe10tot(2)+SizeFe10(i,3)*5.5;
    else
        toolarge=toolarge+1;
    end
end
massFe10=massFe10*kor*10^-6;
massFe10tot=massFe10tot*kor*10^-6;

massSi10=zeros(2,nob);
massSi10tot=zeros(1,2);
u=ceil((aero_max*(2.7^-0.5)-0.5)/0.3);
for i=1:length(SizeSi10)
    bin=SizeSi10(i,1);
    massSi10(1,bin)=massSi10(1,bin)+SizeSi10(i,2)*2.7;
    massSi10(2,bin)=massSi10(2,bin)+SizeSi10(i,3)*2.7;
    if bin<=u
        massSi10tot(1)=massSi10tot(1)+SizeSi10(i,2)*2.7;
        massSi10tot(2)=massSi10tot(2)+SizeSi10(i,3)*2.7;
    else
        toolarge=toolarge+1;
    end
end
massSi10=massSi10*kor*10^-6;
massSi10tot=massSi10tot*kor*10^-6;

```

```

massAl10=zeros(2,nob);
massAl10tot=zeros(1,2);
u=ceil((aero_max*(2.6^-0.5)-0.5)/0.3);
for i=1:length(SizeAl10)
    bin=SizeAl10(i,1);
    massAl10(1,bin)=massAl10(1,bin)+SizeAl10(i,2)*2.6;
    massAl10(2,bin)=massAl10(2,bin)+SizeAl10(i,3)*2.6;
    if bin<=u
        massAl10tot(1)=massAl10tot(1)+SizeAl10(i,2)*2.6;
        massAl10tot(2)=massAl10tot(2)+SizeAl10(i,3)*2.6;
    else
        toolarge=toolarge+1;
    end
end
massAl10=massAl10*kor*10^-6;
massAl10tot=massAl10tot*kor*10^-6;

massCa10=zeros(2,nob);
massCa10tot=zeros(1,2);
u=ceil((aero_max*(2.35^-0.5)-0.5)/0.3);
for i=1:length(SizeCa10)
    bin=SizeCa10(i,1);
    massCa10(1,bin)=massCa10(1,bin)+SizeCa10(i,2)*2.35;
    massCa10(2,bin)=massCa10(2,bin)+SizeCa10(i,3)*2.35;
    if bin<=u
        massCa10tot(1)=massCa10tot(1)+SizeCa10(i,2)*2.35;
        massCa10tot(2)=massCa10tot(2)+SizeCa10(i,3)*2.35;
    else
        toolarge=toolarge+1;
    end
end
massCa10=massCa10*kor*10^-6;
massCa10tot=massCa10tot*kor*10^-6;

massS10=zeros(2,nob);
massS10tot=zeros(1,2);
u=ceil((aero_max*(1.3^-0.5)-0.5)/0.3);
for i=1:length(SizeS10)
    bin=SizeS10(i,1);
    massS10(1,bin)=massS10(1,bin)+SizeS10(i,2)*1.3;
    massS10(2,bin)=massS10(2,bin)+SizeS10(i,3)*1.3;
    if bin<=u
        massS10tot(1)=massS10tot(1)+SizeS10(i,2)*1.3;
        massS10tot(2)=massS10tot(2)+SizeS10(i,3)*1.3;
    else
        toolarge=toolarge+1;
    end
end
massS10=massS10*kor*10^-6;
massS10tot=massS10tot*kor*10^-6;

%summary
sum_10=[j p k l m zeilen toosmall toolarge nokat];

%cleaning up
clear bgrd limit a;
clear nob bin i u kor;
clear Fe Si Al Ca S;
clear j p k l m zeilen toosmall toolarge nokat;
clear work winner loser;
clear sbb10;

```

Particle Emissions of a Railway Line Determined by Single Particle Analysis

Ronny Lorenzo^{a,b}, Ralf Kaegi^a, Robert Gehrig^a & Bernard Grobety^b

^aEmpa, Material Science & Technology, Laboratory for Air Pollution and Environmental Technology, Ueberlandstrasse 129, CH-8600 Duebendorf, Switzerland

^bUniversity of Fribourg, Institute for Mineralogy and Petrography, Ch. de Musée 6, CH-1700 Fribourg, Switzerland

Contact: ronny.lorenzo@empa.ch

Introduction

In this study we focus on particulate emissions (PM10) from railroad traffic. Based on a detailed single particle analysis of samples collected perpendicular to railway lines, an emission profile of the railroad was derived. Mass-based emission factors were obtained by modelling the individual particle volumes based on the morphological parameters and multiplying them with the density derived from the chemical composition.

Experimental

Sampling Site

The sampling campaign was conducted at the Juchhof near Zurich (Switzerland) next to a busy railway line. The area consists of several soccer training fields. The closest roads are about 200m to the south and about 250m to the north respectively (fig. 1).

Five PM10 sampling devices were deployed according to the layout given in figure 1. Three sampling devices were positioned at 10m, 36m and 120m from the railway lines. To estimate the accuracy of our measurements two additional ones were placed 10m from the tracks and 50m to either side of the three devices.

All sampling devices were operated simultaneously and controlled by wind direction and speed (fig. 1). The wind parameters were measured at the central 10m position 4m above ground level.

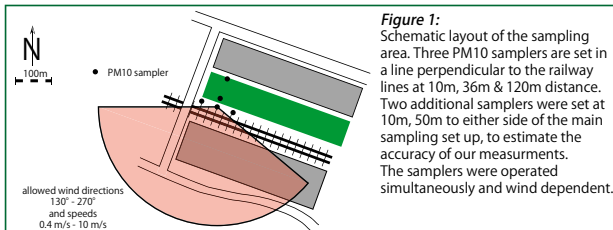


Figure 1: Schematic layout of the sampling area. Three PM10 samplers are set in a line perpendicular to the railway lines at 10m, 36m & 120m distance. Two additional samplers were set at 10m, 50m to either side of the main sampling set up, to estimate the accuracy of our measurements. The samplers were operated simultaneously and wind dependent.

Sampling and Analysis

Particles were collected on Nuclepore filters (0.4µm pore diameter). Five areas on each filter were analyzed. In total an area of 0.4mm² was investigated on every filter. Without any pre-treatment the filters were analyzed with an ESEM (XL 30 FEG, FEI). Elemental analysis was performed with an EDX system (EDAX), attached to the microscope.

Particles were detected based on their backscattered electron signal. Images and analytical data of all particles are stored automatically and can be reviewed manually.

A minimum particle diameter of 0.5µm (projected area equivalent diameter) was set. Smaller particles were not considered for further analysis as the resulting EDX signal was often unsatisfactory. To determine background concentrations of the elements of interest and to verify the spectra of not classified particles, all EDX spectra were manually reviewed. In total approximately 11'000 particles were analyzed and of these more than 90% could be classified using our classification scheme.

Results

Five particle classes were identified: 'iron-rich', 'aluminium bearing', 'high silica', 'calcium bearing' and 'pure sulphur'.

Details on morphology and possible origin for the particles of the 'iron rich', 'aluminium bearing' and 'calcium bearing' class are given in figure 2.

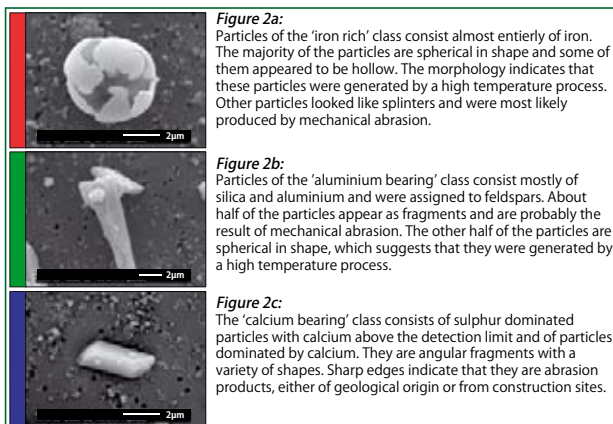


Figure 2a: Particles of the 'iron rich' class consist almost entirely of iron. The majority of the particles are spherical in shape and some of them appeared to be hollow. The morphology indicates that these particles were generated by a high temperature process. Other particles looked like splinters and were most likely produced by mechanical abrasion.

Figure 2b: Particles of the 'aluminium bearing' class consist mostly of silica and aluminium and were assigned to feldspars. About half of the particles appear as fragments and are probably the result of mechanical abrasion. The other half of the particles are spherical in shape, which suggests that they were generated by a high temperature process.

Figure 2c: The 'calcium bearing' class consists of sulphur dominated particles with calcium above the detection limit and of particles dominated by calcium. They are angular fragments with a variety of shapes. Sharp edges indicate that they are abrasion products, either of geological origin or from construction sites.

Most of the particles of the 'pure silica' class (~99%) consist entirely of silica and can therefore be identified as quartz. These particles are predominantly fragments with sharp edges, a typical morphology of fractured quartz.

'Pure sulphur' particles were assigned to vehicular exhausts. The shapes and structures of these particles – chains and fractal-like structures consisting of spheres smaller than 40nm – support this assumption. Most likely they are sulphur coated soot particles.

The change in particle number for each class with increasing distance to the railway lines is given in figure 3. The strongest decrease in particle numbers with increasing distance is observed for the 'iron rich' particles.

The plots for the 'aluminium bearing' and the 'calcium bearing' particles are similar but the decrease in particle number is weaker. The gravel bed of the railway lines contains feldspars as well as calcium bearing minerals. Therefore, it can be assumed that wear of the gravel bed is a source for 'aluminium bearing' and 'calcium bearing' particles.

In contrast, the particle numbers for the 'high silica' particles increase from 10m to 36m before numbers decrease towards 120m. Thus, there has to be a source for quartz particles between 10m and 36m. However, due to the wind controlled sampling, the gravel bed of the railway lines was identified as a source for quartz particles.

The number concentration for 'pure sulphur' particles is fairly constant, indicating that railway traffic is not a source for these particles.

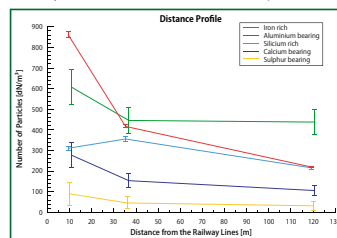


Figure 3: Distance Profile. The error bars (2σ) are calculated from the standard deviation of the three sampling devices at 10m distance from the railway lines. The values at 10m are average values from the three sampling sites at 10m. For better readability of the figure the five plots are shifted horizontally.

For the mass calculations particles were modelled as prolate ellipsoids and densities were assumed according to the chemical composition of the classes. In fig. 4a the particle mass distributions at 10m are plotted for the three most important classes. To estimate the emission factors of the railway lines for these classes, it was assumed that background levels are reached at 120m.

Figure 4b shows the calculated source strength for the 'iron rich', 'aluminium bearing' and 'calcium bearing' particles. All three mass distributions have their maximum between 3µm and 4µm, contributing therefore mainly to the coarse fraction of PM10.

The emissions of the railway lines are dominated by iron particles, adding up to 2.9 µg/m³. The 'aluminium bearing' particles contribute 1.0 µg/m³ and the 'calcium bearing' 0.4 µg/m³. The total contribution of the railway lines to local PM10 sums up to 4.3 µg/m³. Compared to the total PM10 (about 27 µg/m³), the railway related particles contribute 16% of the total mass.

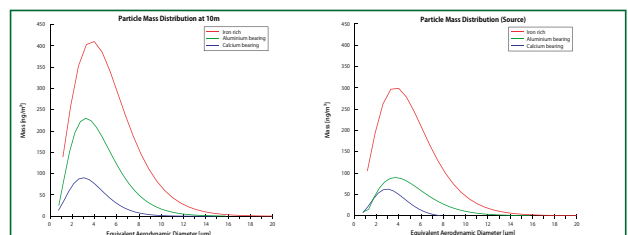


Figure 4a: Particle mass distributions at the 10m site for the three most important particle classes.

Figure 4b: Source contribution to the particle mass distributions for the three most important particle classes. Calculated as the difference of the 120m and the 10m site.

Conclusions

In this study detailed single particle analysis was used to characterize particulate emissions from a railway line. Five particle classes – 'iron rich', 'aluminium bearing', 'pure silica', 'calcium bearing' and 'sulphur bearing' – were distinguished. It has been shown that railway traffic produces large amounts of iron particles (2.9 µg/m³) due to wear of rails, wheels and brakes. Wear of the gravel bed of the railway lines contributes fair amounts of 'aluminium bearing' (1.0 µg/m³) and 'calcium bearing' particles (0.4 µg/m³).

We have demonstrated that detailed single particle analysis not only delivers comprehensive data of individual particles (morphology and chemistry) but can be used for size, mass and chemistry resolved descriptions of aerosols as well.

A.3 Additional information on Chapter 3

A.3.1 Matlab sheet

TPS_inc.m

```

TPS_incl.m

%calculates the deposition coefficients for the thermophoretic sampling device

%definition of variables*****
dV = 2000/60;      %Flow in ccm/s
hc = 0.03;        %height of the sampling channel in cm
wc = 2;          %width of the sampling channel in cm
g = 0.2;         %radius Peltier cm
rg = 0.1525;     %radius grid cm

dT = 120;        %temperatur difference in K

p = 1013;        %ambient pressure in mbar (hPa)
T = 273.15+20;  %gas temperatur in K (0°C + gastemperatur in °C)

ac = 0;          %accomodation coefficient, "stickiness" of the Particles
kg = 0.024;     %thermal conductivity of air
kp = 10;        %thermal conductivity of the Particles (iron:80, Granite:2)

N = 10^7;       %number of trajectories
M = 100;        %resolution of the "touch down mesh"

%parameters*****
%thermophoretic settling speed in cm/s B&W 8-75
vt = kg*dT/(hc*p*5*(1+ac*pi/8))*100;

%flow velocity in the centre of the sampling channel
vc = 1.5*dV/(hc*wc);

%eigenvalue equations for the determination of the maximum height
d = -4*vc/(3*vt*(hc^2)); %x^3
c = 2*vc/(vt*hc);      %x^2
b = 0;                 %x^1
a = -(rg+g);           %x^0

interim=polyeig(a,b,c,d);
for k=1:3
    if (interim(k)>0)
        maxz = interim(k)*1.2;
    end
end

%*****
%initialising
total_part = 0;
l = zeros(M,M); %saves landing coordinates (statistics)
tstep = 1e-5; %time steps, 10µs

%calculation
for i=1:N %number of particle
    z = unifrnd(0,hc/2);
    x = 0;
    scalef = 4*vc*wc*(z^2)*(hc-z)/(dV*hc^2);
    total_part = total_part+scalef;
    if z>maxz %particles that cannot land will not be calculated
        smaller = 0;
    else
        smaller = 1;
        y = unifrnd(-rg,rg);
        limiter = g+(rg^2-y^2)^(0.5);
        step= unifrnd(tstep/4,tstep); %2.5..10µs
    end
end

```

```

while (smaller>0)
    vx = 4*vc*(hc*z-z^2)/hc^2;
    r=((rg-(x-0.0475))^2+y^2)^0.5; %distance to the centre of the grid
    if r<=g
        z = z-step*vt;
    end
    x = x+step*vx;
    if (z<=0) %landed?
        if r<=rg
            u = ceil((x-0.0475)/(2*rg/(M-1)));
            w = round(y/(2*rg/(M-1)))+M/2;
            l(u,w) = l(u,w)+scalef;
            break;
        else
            break;
        end
    end
    smaller = limiter-x;
end
end

%*****
%calculates the deposition efficiency by mesh
fields=0; %number of used meshes
landed=sum(sum(l));
for i=1:M
    for j=1:M
        if l(i,j)>0
            fields=fields+1;
        end
    end
end

%efficiency per mesh
eff_l = l/(total_part*wc/rg);

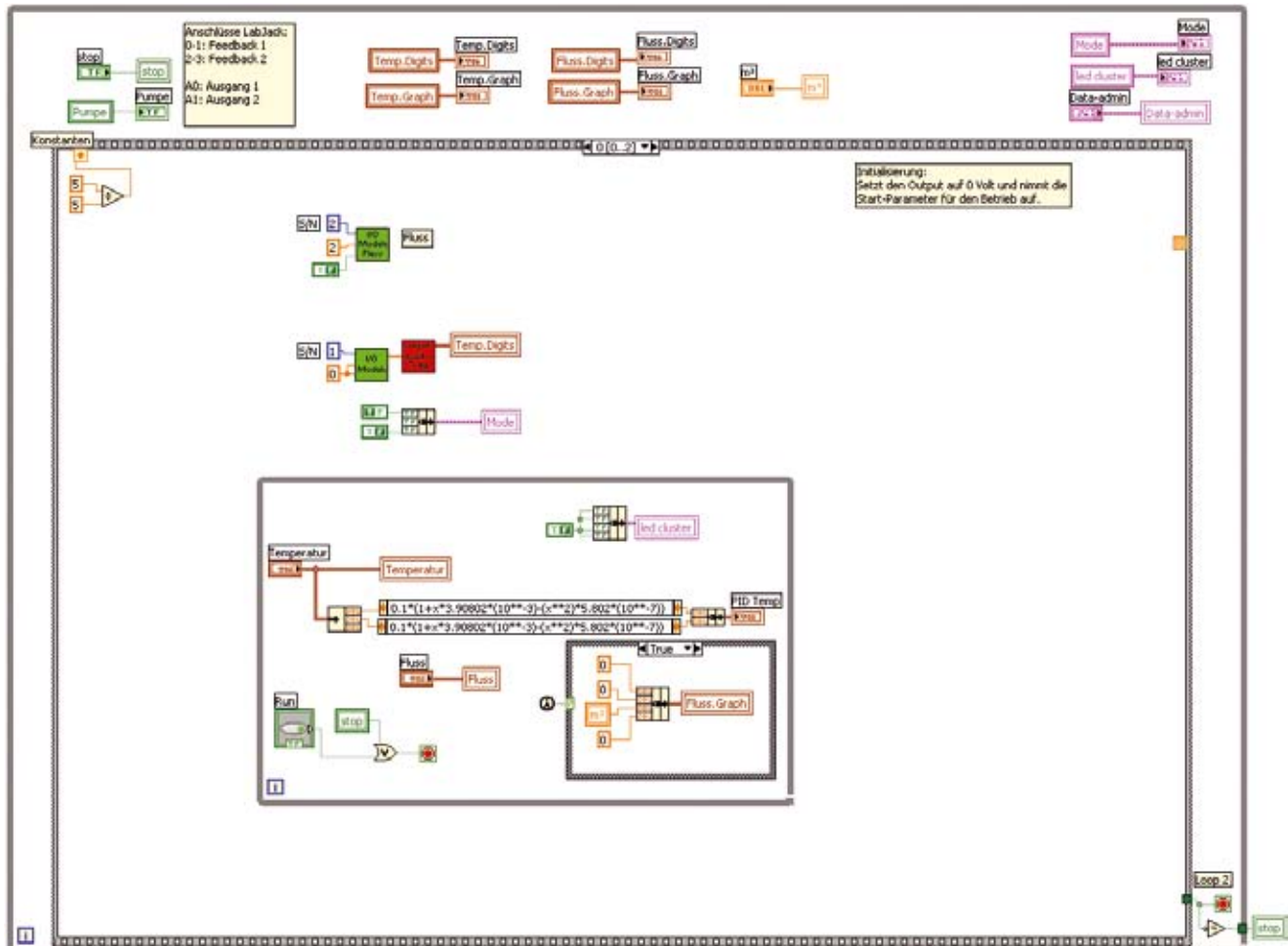
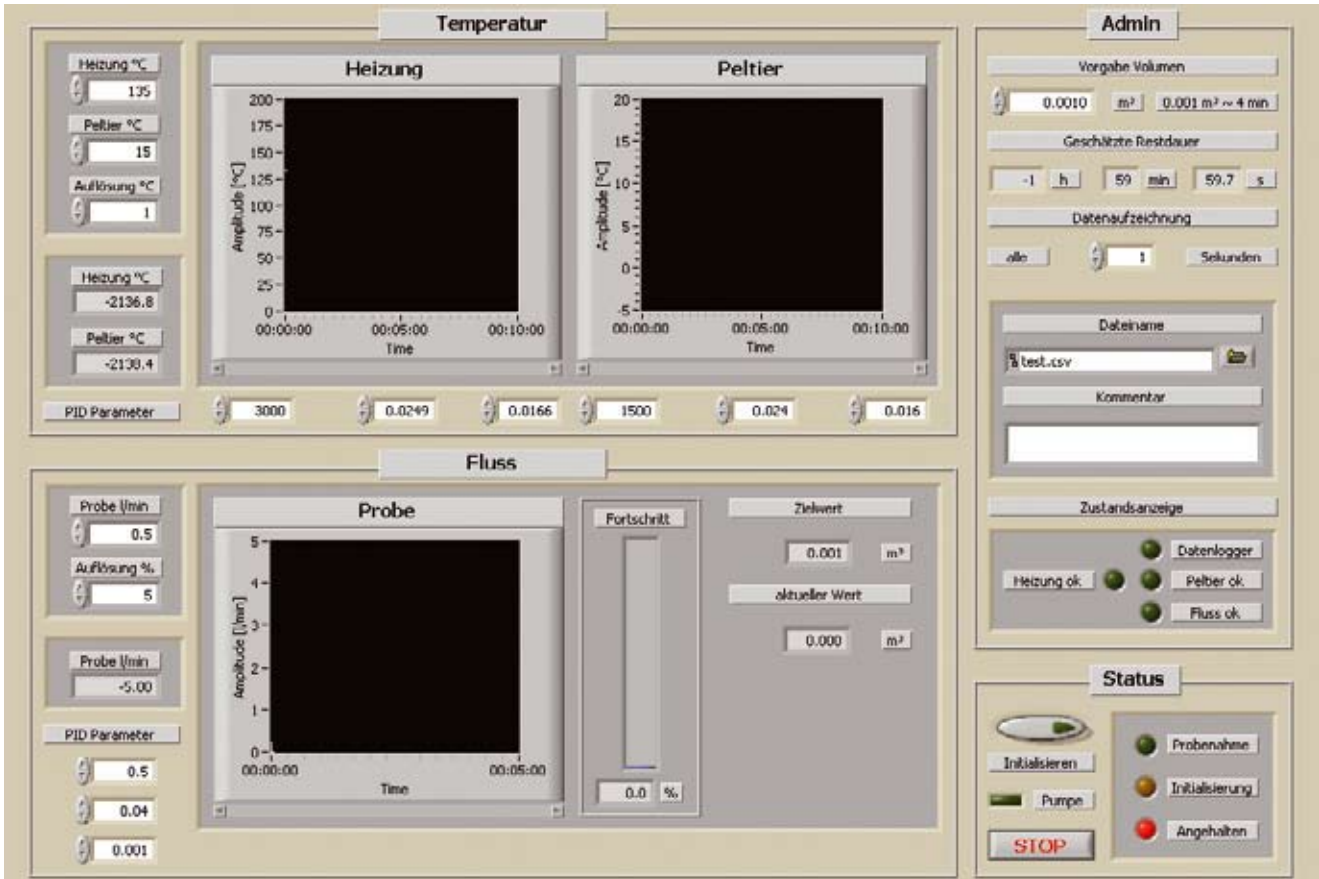
%efficiency of the entire Grid
eff_grid = sum(sum(eff_l));

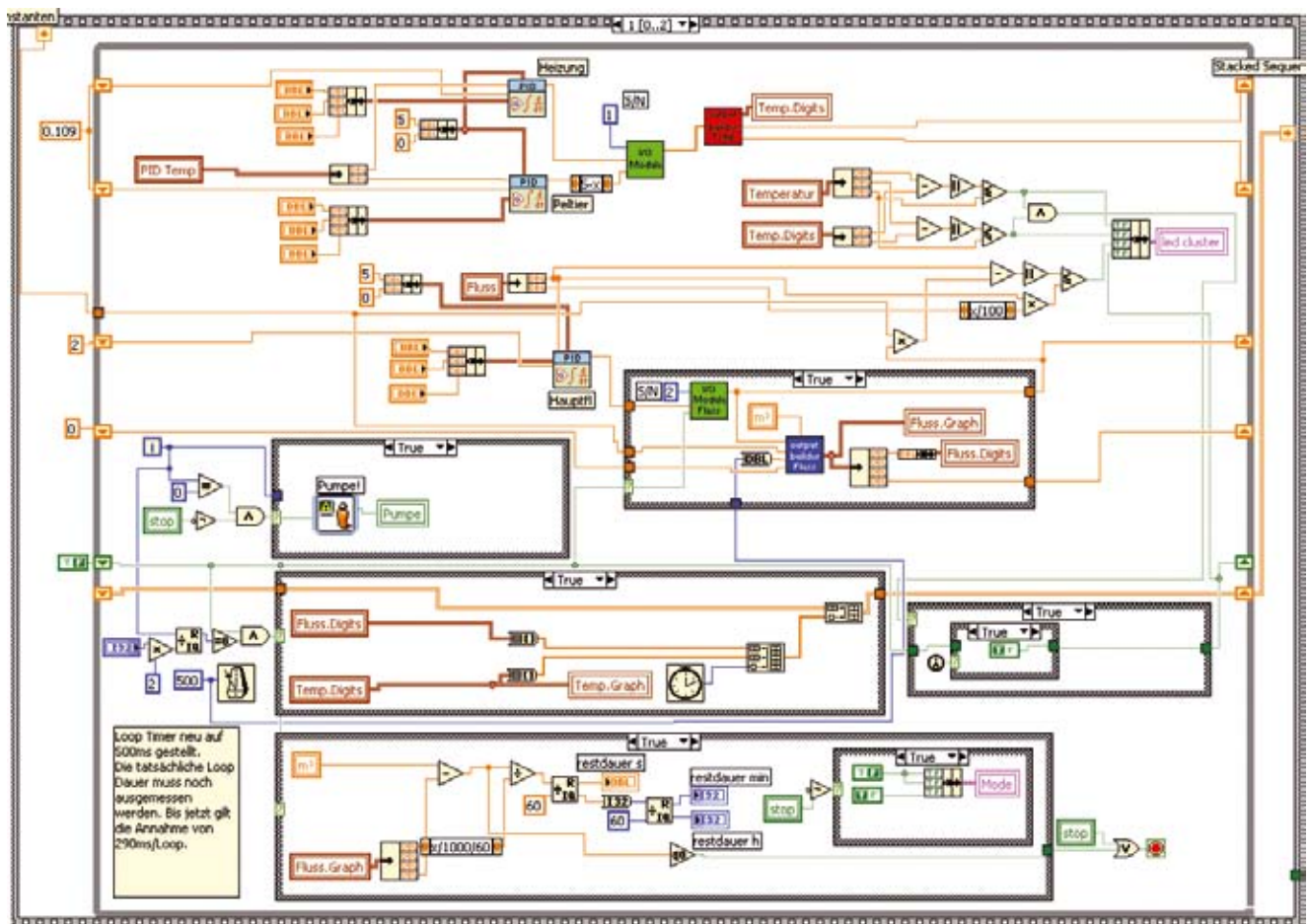
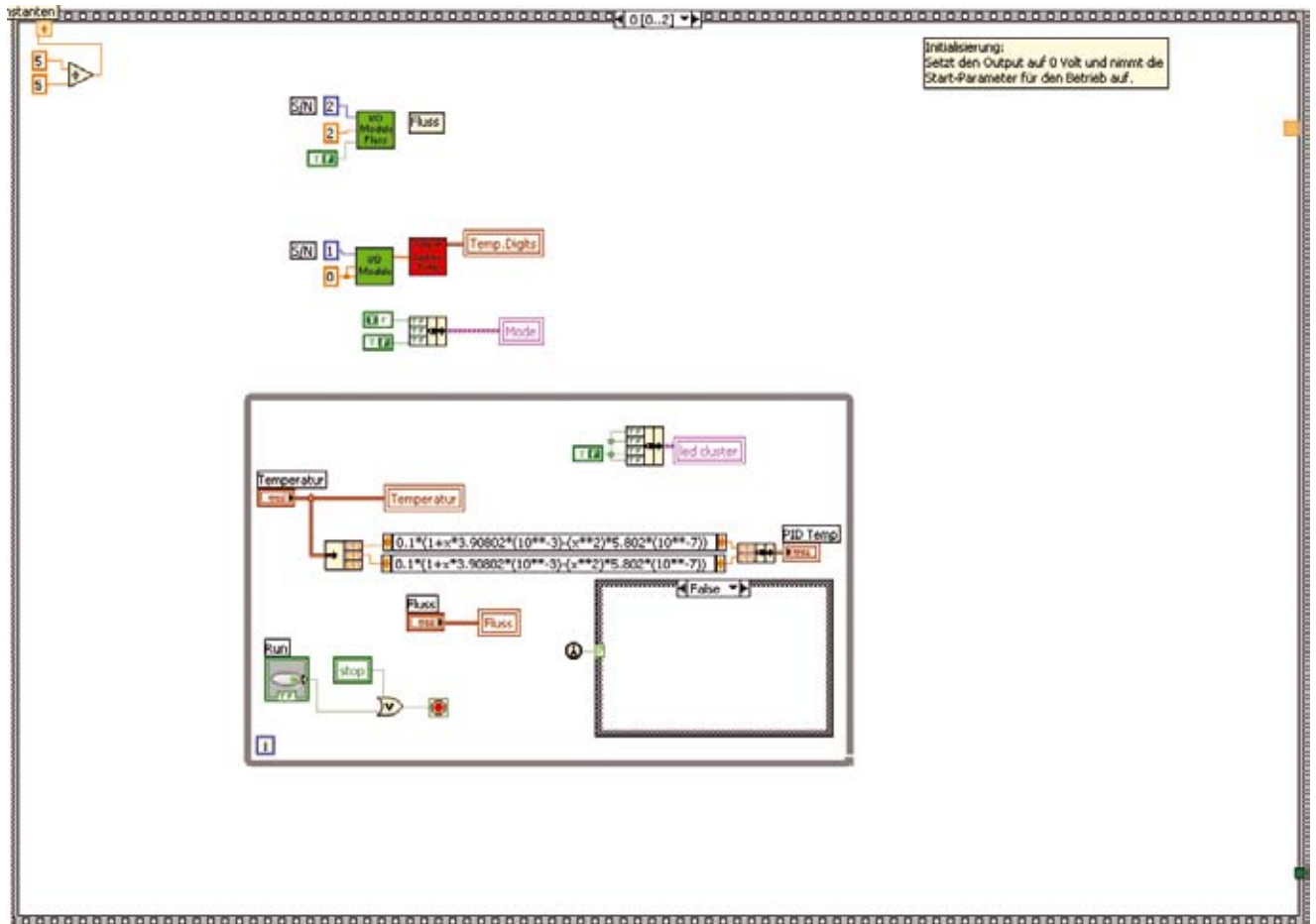
%output
pcolor(eff_l);

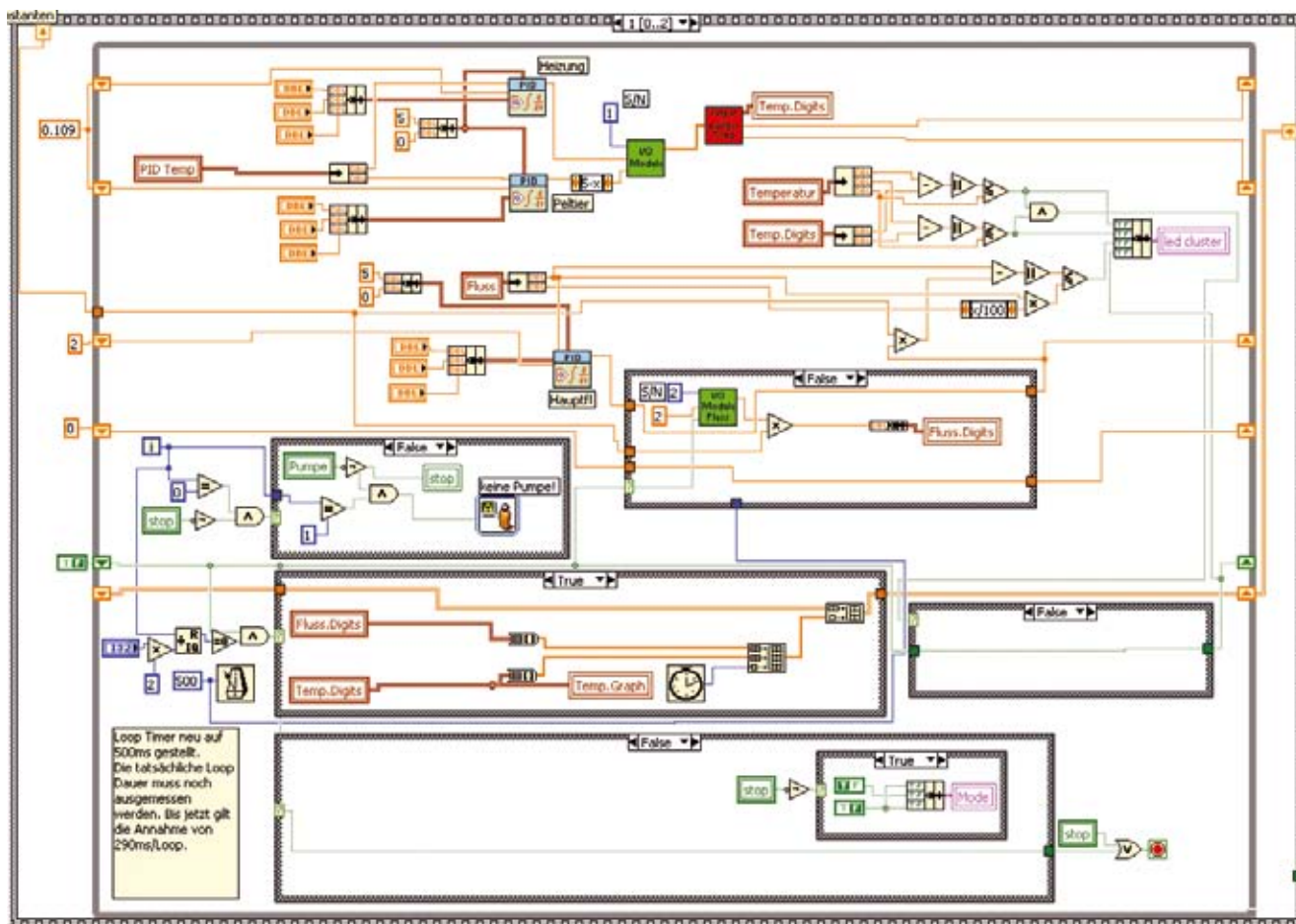
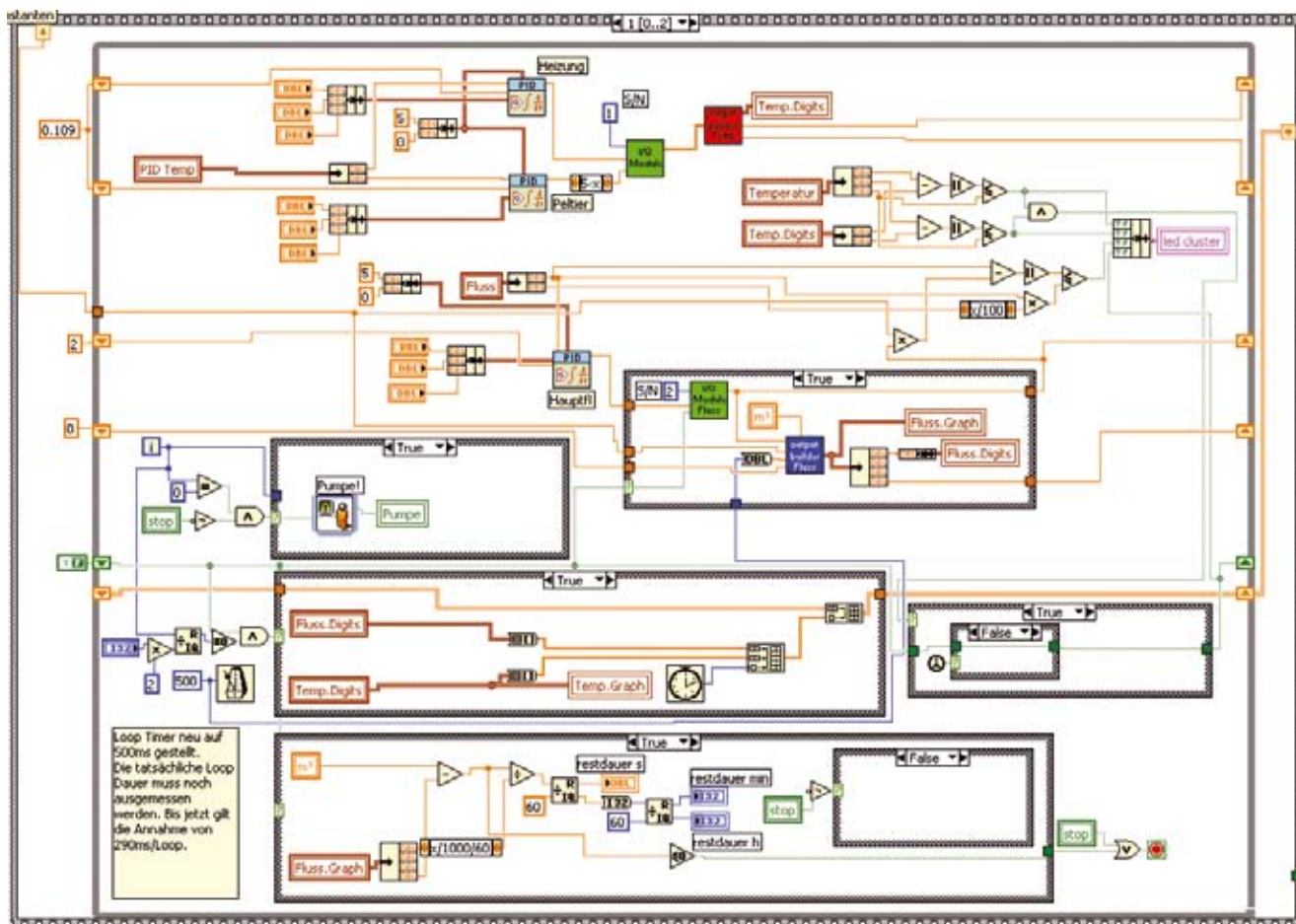
```

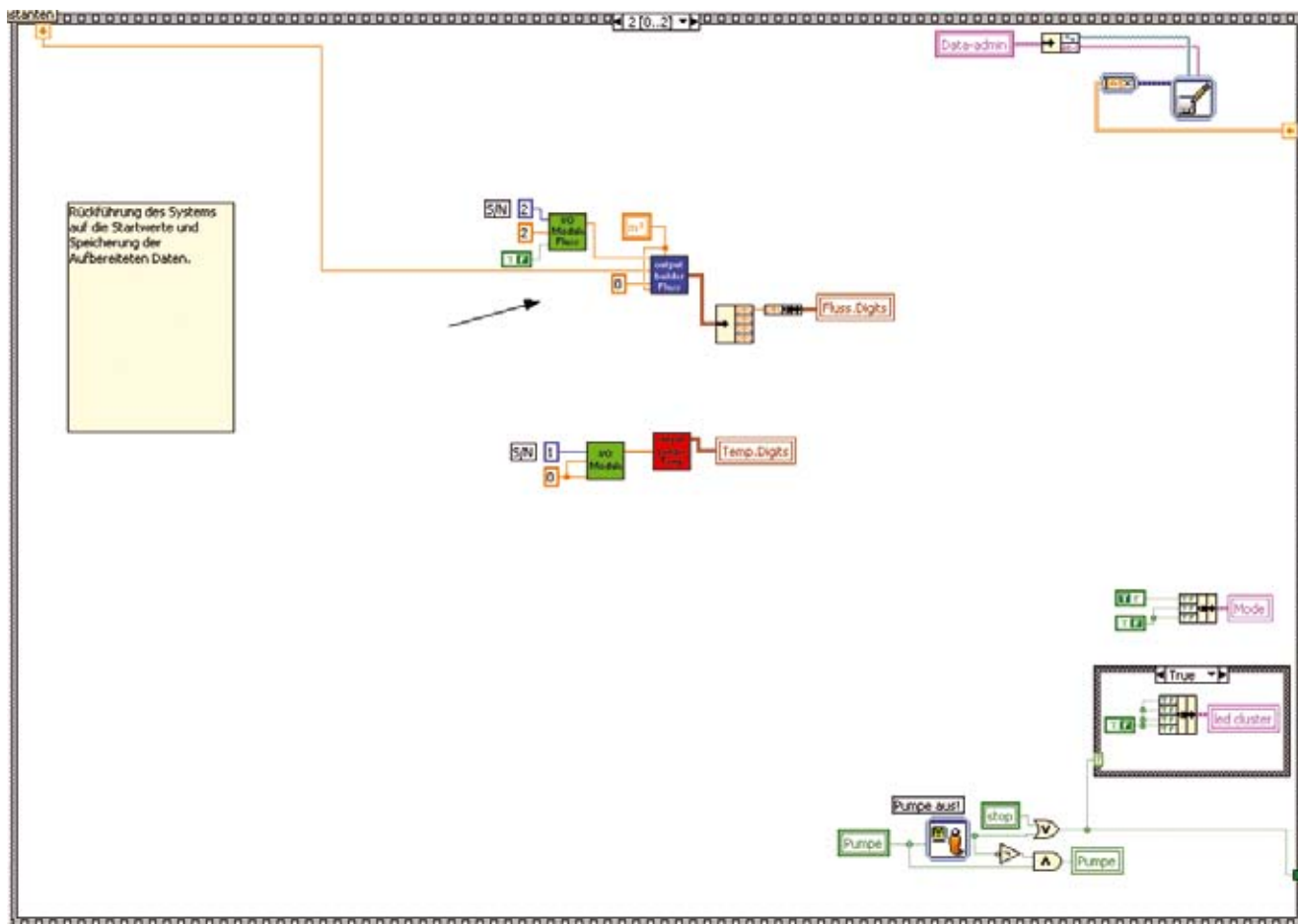
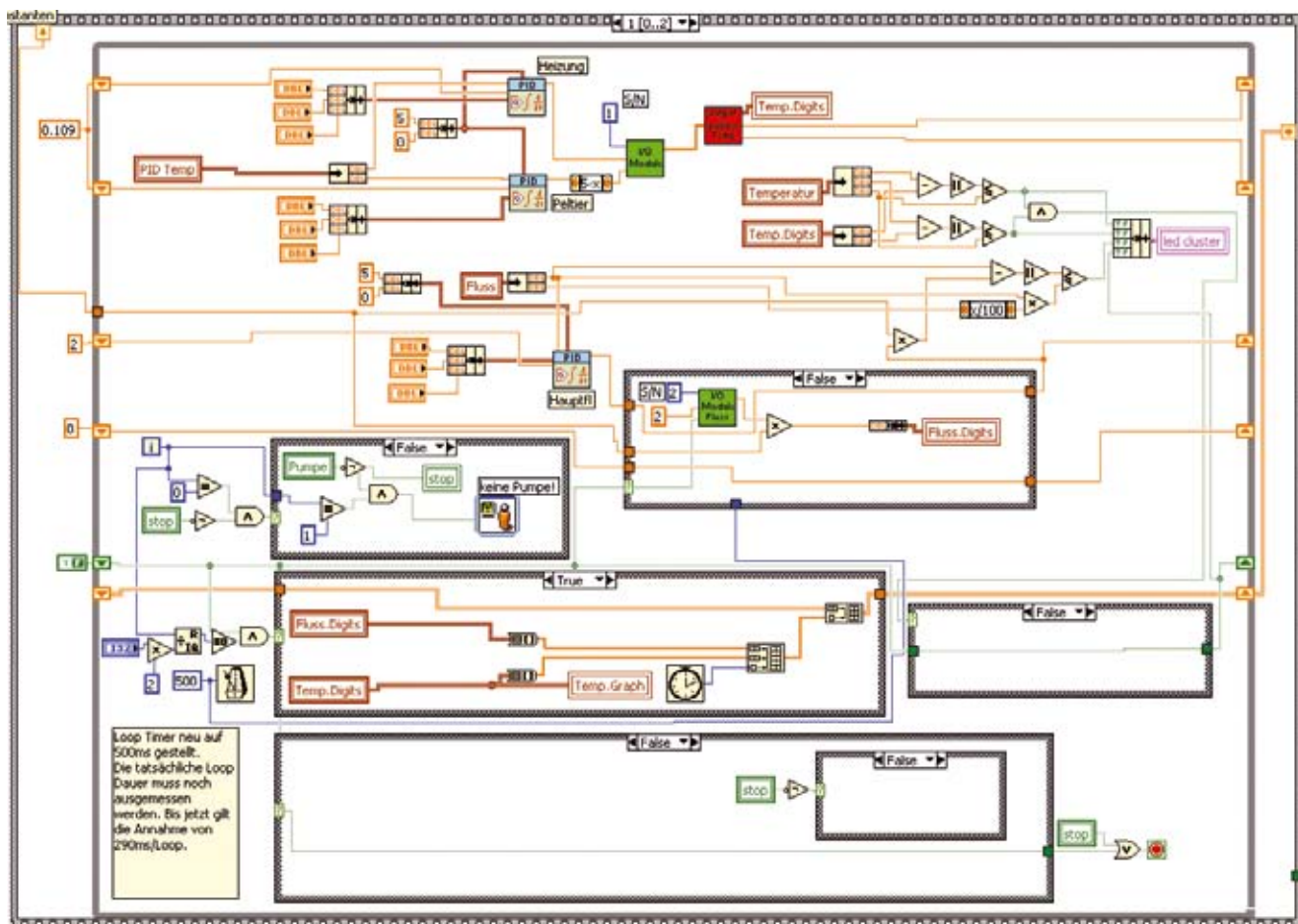
A.3.2 LabView VI

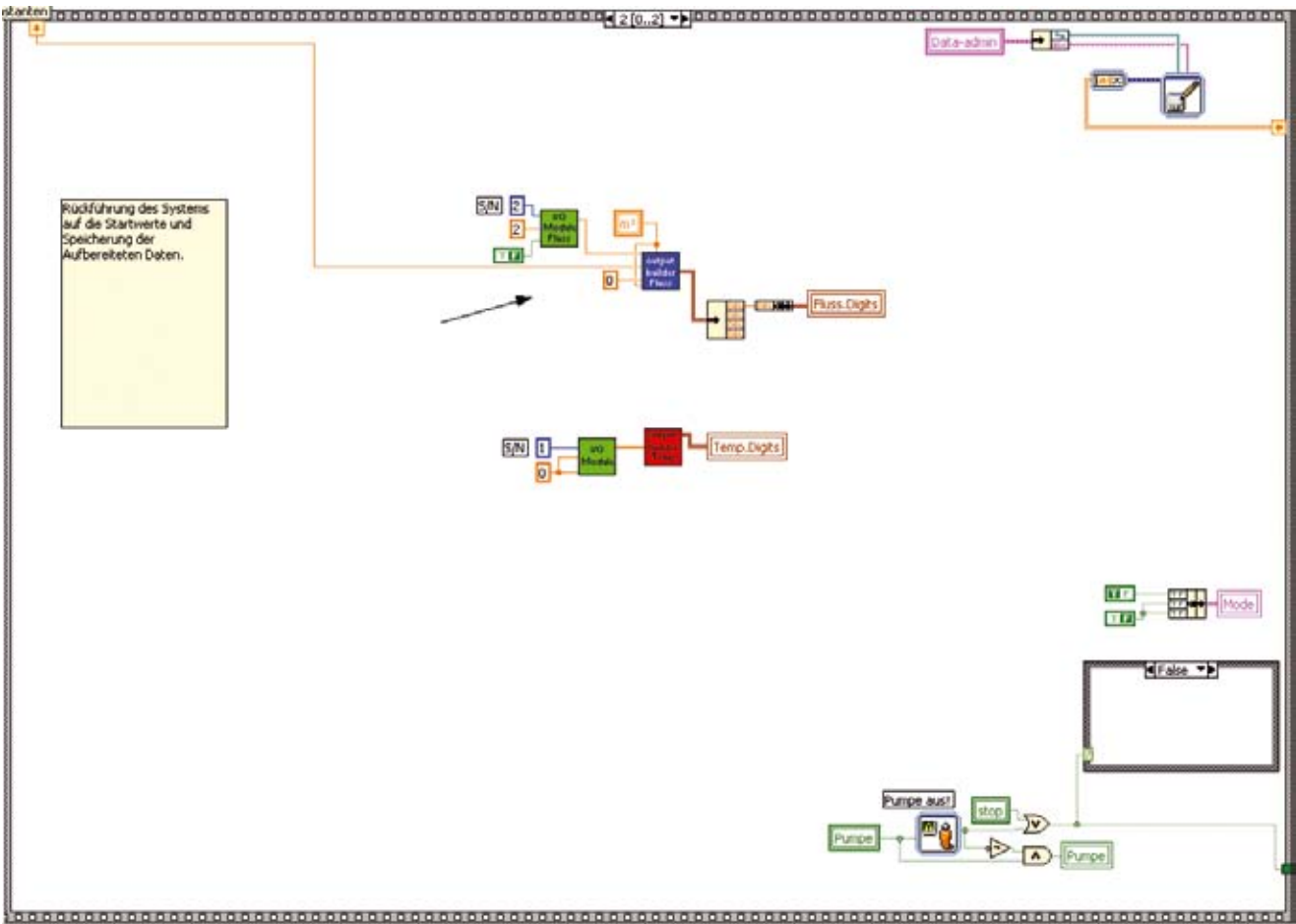
sampler_3-3.vi



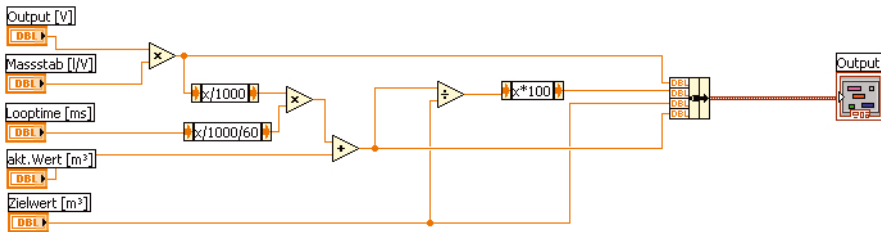




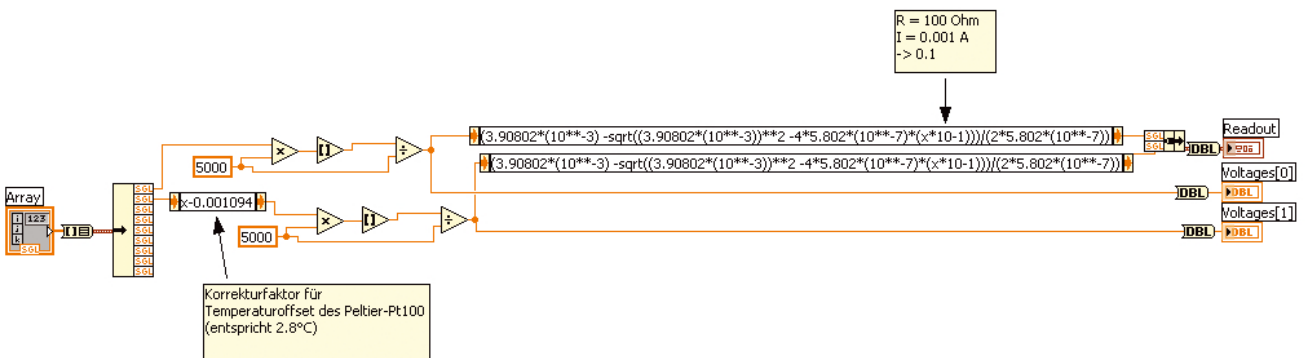




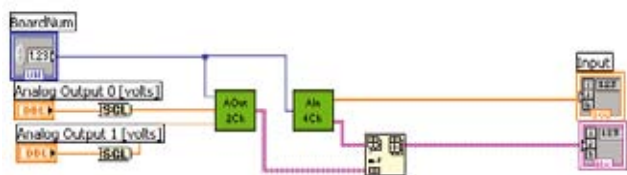
output_builder_Fluss.vi



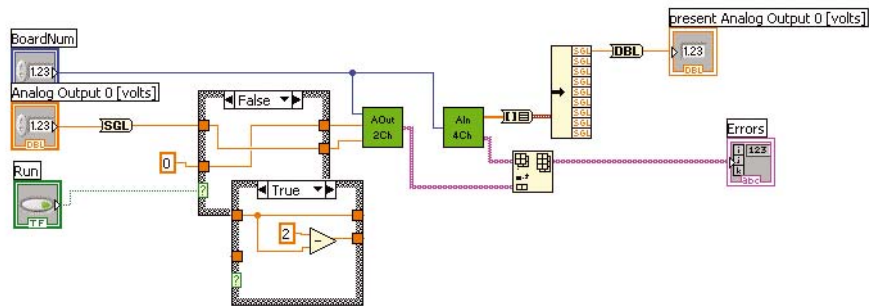
output_builder_Temp.vi



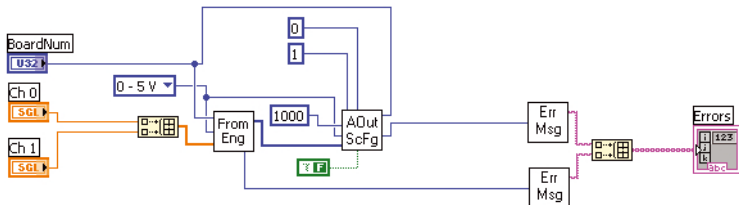
IO_subVI.vi



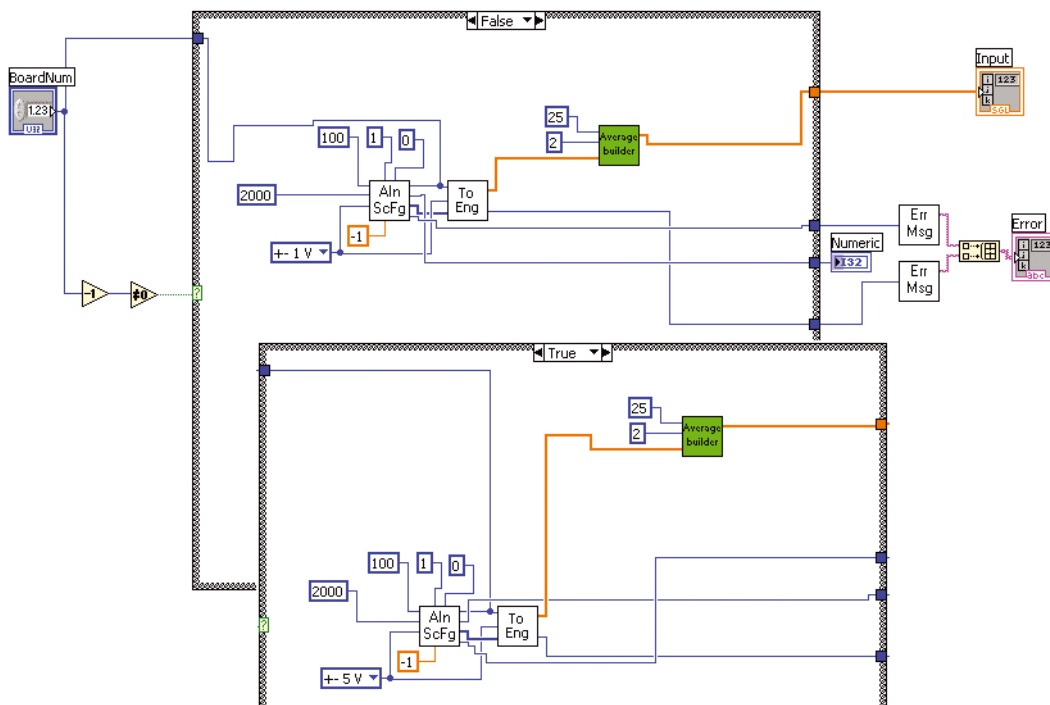
IO_Fluss_subVI.vi



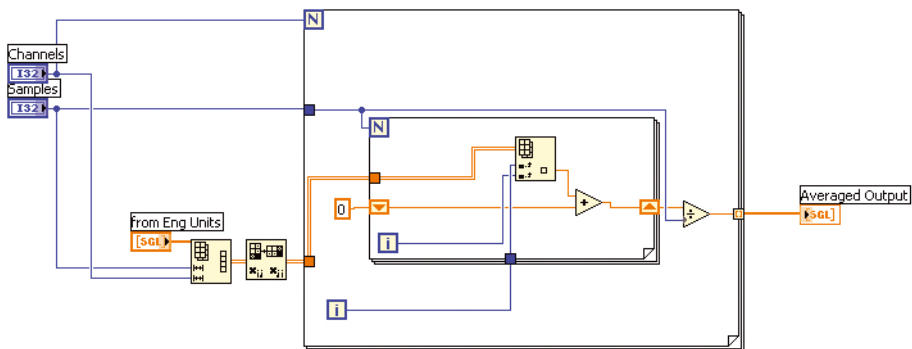
AOut-2Ch.vi



AIn-4Ch.vi



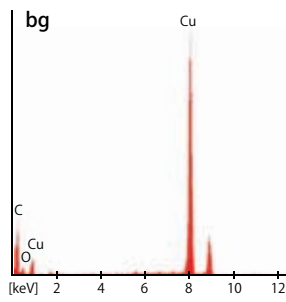
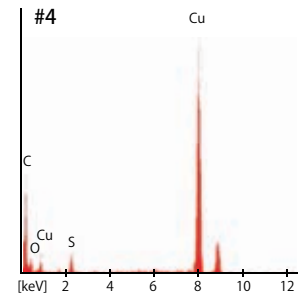
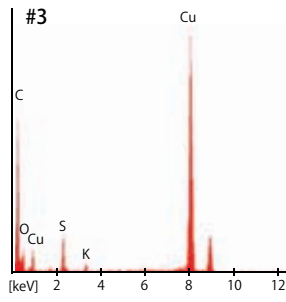
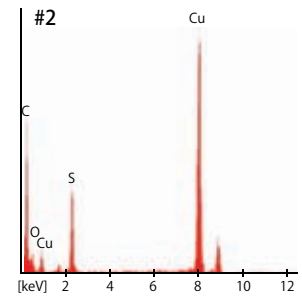
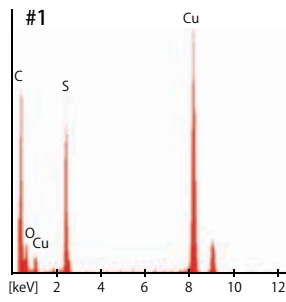
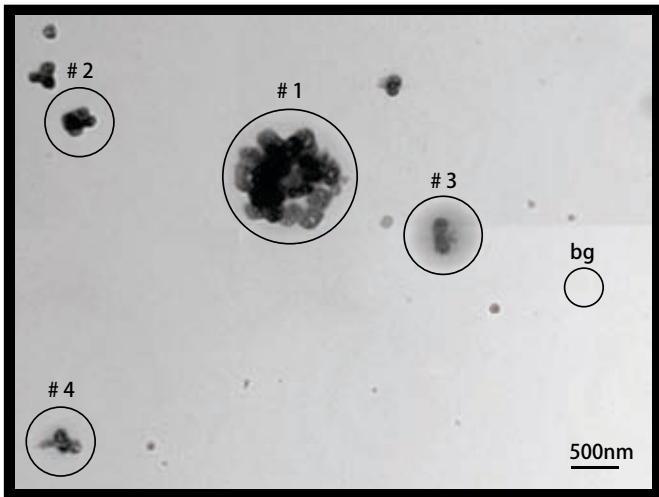
Averager.vi



A.3.3 Preliminary results of the CLACE 4 campaign (Jungfrauoch)

Jungfrauoch, Date, 18h; Montage

TEM Image, 300kV, 6kx



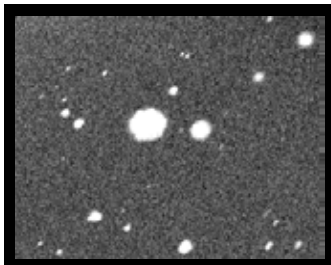
Parameter TEM

HV: 300kV
Aperture: 3
Spot: 5 (5nm)
Camera Length: 140mm
Magnification: 15kx

Parameter EDX

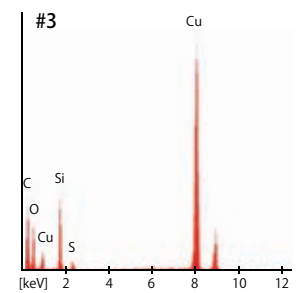
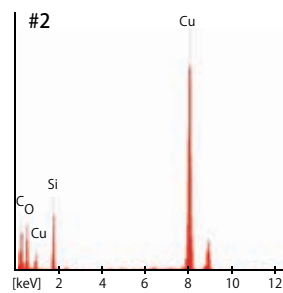
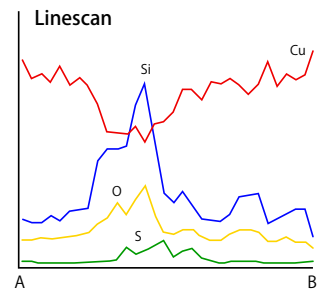
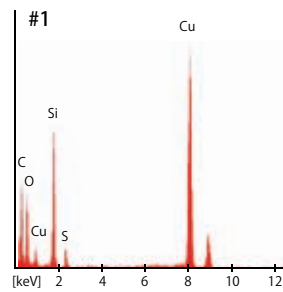
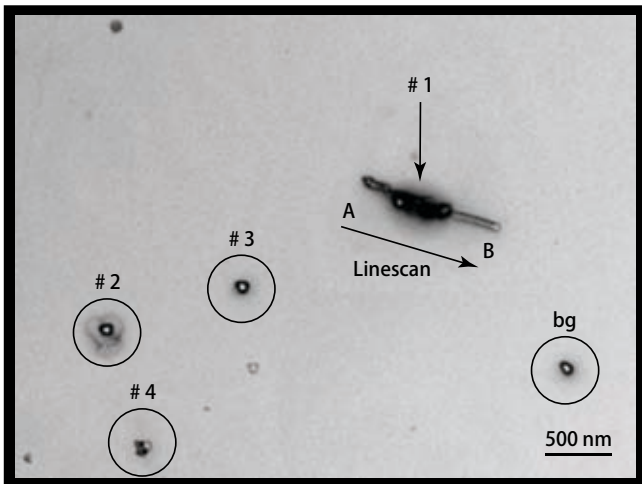
Live Sec.: 50
Deadtime: 50%
Counts/sec.: 250

STEM Image, 300kV, 15kx



Jungfrauoch, Date, 18h; Montage

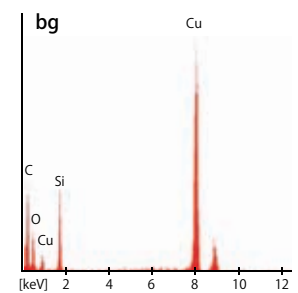
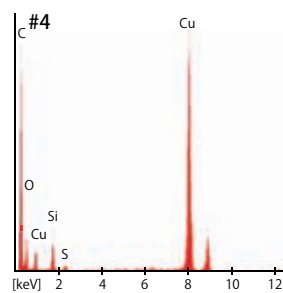
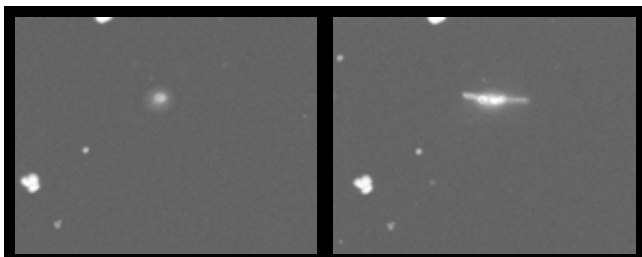
TEM Image, 300kV, 6kx



STEM Image, 300kV, 30kx

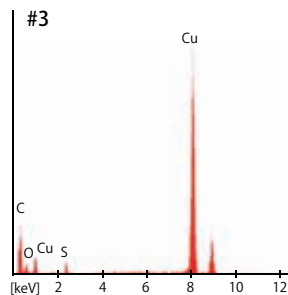
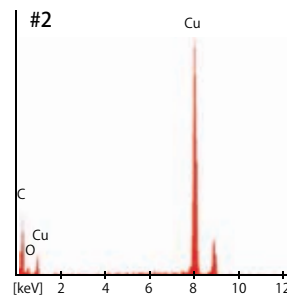
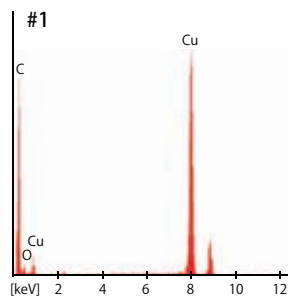
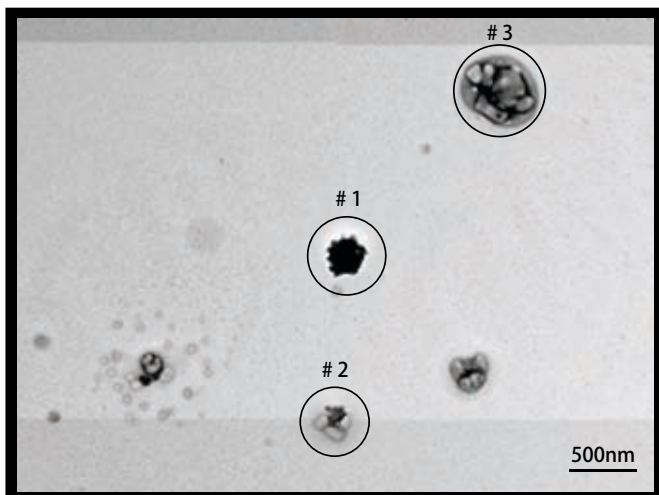
before

after

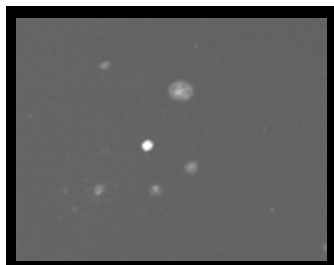


Jungfrauoch, Date, 18h; Montage

TEM Image, 300kV, 6kx



STEM Image, 300kV, 20kx



Parameter TEM

HV: 300kV
Aperture: 3
Spot: 5 (5nm)
Camera Length: 140mm
Magnification: 20kx

Parameter EDX

Live Sec.: 50
Deadtime: 55%
Counts/sec.: 250

A New Thermophoretic Sampling Device for Collection of Ultrafine Particles

Ronny Lorenzo^a, Ralf Kaegi^a, Leo Scherrer^b & Bernard Grobety^c

^aEmpa, Material Science & Technology, CH-8600 Duebendorf, Switzerland
^bSwiss Federal Institute for Technology, CH-8000 Zurich, Switzerland

^cUniversity of Fribourg, Ch. de Musée 6, CH-1700 Fribourg, Switzerland
 Contact: ronny.lorenzo@empa.ch

Introduction

The morphology, structure and composition of ultrafine aerosol particles (diameter smaller than 100nm) is frequently analysed by means of transmission electron microscopy (TEM). For this purpose, particles need to be deposited on TEM grids. To avoid preparation artefacts, it is best to sample ultrafine particles directly from the aerosol onto the support film of the TEM grid.

For ultrafine particles the only viable deposition mechanisms are diffusion, electrophoresis and thermophoresis. Of these three only thermophoresis is virtually independent of particle size for particle diameters smaller ~100nm (and strictly independent for diameters smaller ~60nm).

Design

The design of our prototype follows roughly the description given by Maynard (1995). The most important improvements are the possibility to change sample flows, the control of the temperature gradient by cooling the TEM support grid and simultaneously heating the opposite side of the flow channel (figure 1), and a computer interface for real time adjustments and logging of parameters.

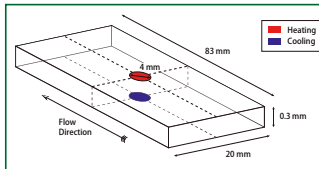


Figure 1: Sketch of the flow channel of the thermophoretic sampling device. Standard sampling flow is 2 l/min, leading to a maximum flow speed of 8,33 m/s. The TEM support grid is kept at 293 K and the opposite side is heated to 428 K, resulting in a temperature gradient of 410³ K/m.

Experiments and Results

We developed a numerical model to estimate the precipitation efficiency (figure 2) and to optimise the design of the sampler. To calibrate the sampling device and to verify the numerical model a series of experiments with well defined aerosols were conducted.

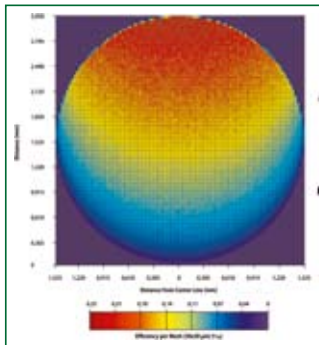


Figure 2: Result of the numerical model showing the precipitation efficiency and characteristics of the sampling device. If operated with a sample flow of 2 l/min and with a temperature gradient of 410³ K/m, 0,9% of the particles entering the device will be precipitated on the TEM support grid. Towards the end of the support grid (looking in the direction of the sample flow) more particles are precipitated than at the beginning. The deposition efficiency of the innermost 20% of the support grid is constant.

In a first series of experiments polydisperse Ag aerosols with modes at 27nm, 45nm and 90nm respectively, were produced. Samples were taken on Ni TEM support grids with a thin carbon film.

The size distributions derived from TEM images were in excellent agreement with the results from SMPS scans (figure 3).

To further investigate the deposition characteristics of the sampling device, two samples taken with different temperature gradients applied were analysed in more detail using a scanning electron microscope (SEM). Images along a concentric circle were investigated for the number of particles deposited. The comparison between the calculated particle numbers is in good agreement with the experimental findings (figures 4 & 5).

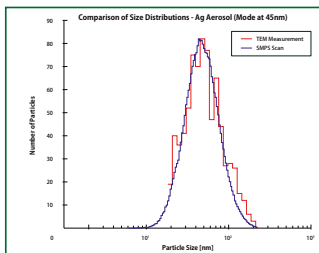


Figure 3: Comparison of the size distribution of the precipitated particles as determined from TEM images (red) with the SMPS scans performed during sampling (blue). Sampling time was 2 min at 2 l/min. Particle number concentration of the sampled polydisperse aerosol was 4,8·10⁶ particles/ccm with a mode at 45nm. The temperature gradient applied was 4·10³ K/m.

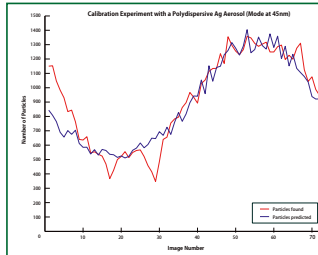


Figure 4: Comparison of calculated (blue) and counted (red) particle number along a concentric circle (radius ~0.8 mm). Particle number concentration of the sampled Ag aerosol was 4,8·10⁶ particles/ccm with the mode at 45nm. Sampling time was 2 min at 2 l/min and a temperature gradient of 410³ K/m. The calculated particle number distribution follows the experimentally determined profile very well.

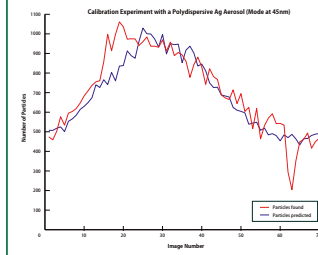


Figure 5: The particle number concentration of the Ag aerosol used for this comparison was 5,2·10⁶ particles/ccm with the mode at 45nm. The sampling time was 2 min at 2 l/min and a temperature gradient of 3,310³ K/m. While the temperature gradient was reduced by one sixth the deposition efficiency decreased about one third.

In a second series of experiments monodisperse Ag aerosols with particle sizes of 20nm, 40nm, 80nm and 160nm respectively, were selected using a DMA. Particle numbers along a centre line of the TEM grids were investigated with a SEM. The different profiles observed (figures 6 & 7) are caused by different orientations of the cross sections relative to the direction of the sample flow.

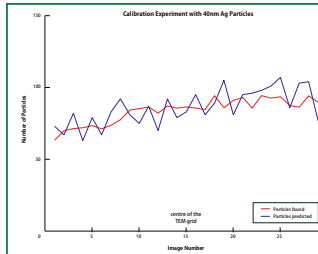


Figure 6: Comparison of an experimentally obtained (red) and a calculated (blue) cross section. The particle concentration of the aerosol was 1,5·10⁴ particles/ccm. The sampling time was 25 minutes at 2 l/min and a temperature gradient of 410³ K/m. The modeled distribution fits the experiment well. The sampling efficiency on the innermost areas of the support grid is as expected, fairly constant.

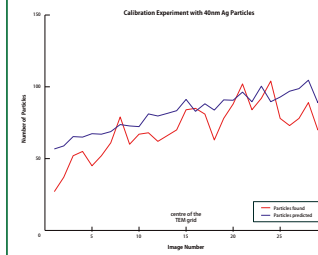


Figure 7: The aerosol of 40nm Ag particles used for this experiment had a number concentration of 1,4·10⁴ particles/ccm. Sampling parameters were the same as described above. The calculated profile follows the experiment well. The images 10 to 20 show an almost constant deposition efficiency and represent an area of 0,07mm². This area is large enough for a thorough TEM analysis.

Conclusions

Our calibration experiments show that the thermophoretic precipitator as described here can be used for representative sampling of ultrafine aerosol particles. The numerical model developed in this study can reproduce the experimental data very well which allows us to estimate the proper sampling time, determine on what area representative sampling has been achieved and to quantify the results obtained from single particle analysis.

Acknowledgment

We thank Martin Fierz of the Fachhochschule Aargau for providing us with his expertise in aerosol sampling and the facilities for producing Ag aerosols necessary for calibrating the sampling device.

Reference

Maynard, A.D., 1995. The Development of a New Thermophoretic Precipitator for Scanning-Transmission Electron-Microscope Analysis of Ultrafine Aerosol-Particles. *Aerosol Science and Technology*, 23(4): 521-533.

A.4 Additional information on Chapter 4

A.4.1 MathCAD sheet

Bagsampler.mcd

$$k := 1.3807 \cdot 10^{-23} \quad p_0 := 101.3 \quad g := 9.81$$

$$\eta_{\text{air}}(\text{Temp}) := 1.708 \cdot 10^{-5} \cdot \left(\frac{\text{Temp}}{273.15} \right)^{1.5} \cdot \frac{393.396}{\text{Temp} + 120.246}$$

$$\text{scf}(D_p, p) := 1 + \frac{1}{p \cdot D_p} \cdot (15.60 + 7.00 \cdot e^{-0.059 \cdot p \cdot D_p}) \quad \text{B\&W 4-9}$$

$$V_{\text{ts}}(\text{Temp}, D_p, \rho_p, p) := g \cdot \frac{\rho_p \cdot (D_p \cdot 10^{-6})^2 \cdot \text{scf}(D_p, p)}{18 \cdot \eta_{\text{air}}(\text{Temp})} \quad \text{B\&W 4-34f}$$

$$k_e(Q) := 1.35 \cdot 10^5 \cdot Q^{1.5} \quad \text{B\&W 8-81}$$

$$D(\text{Temp}, D_p, p) := \frac{k \cdot \text{Temp} \cdot \text{scf}(D_p, p)}{3 \cdot \pi \cdot \eta_{\text{air}}(\text{Temp}) \cdot D_p \cdot 10^{-6}} \quad \text{B\&W 4-13}$$

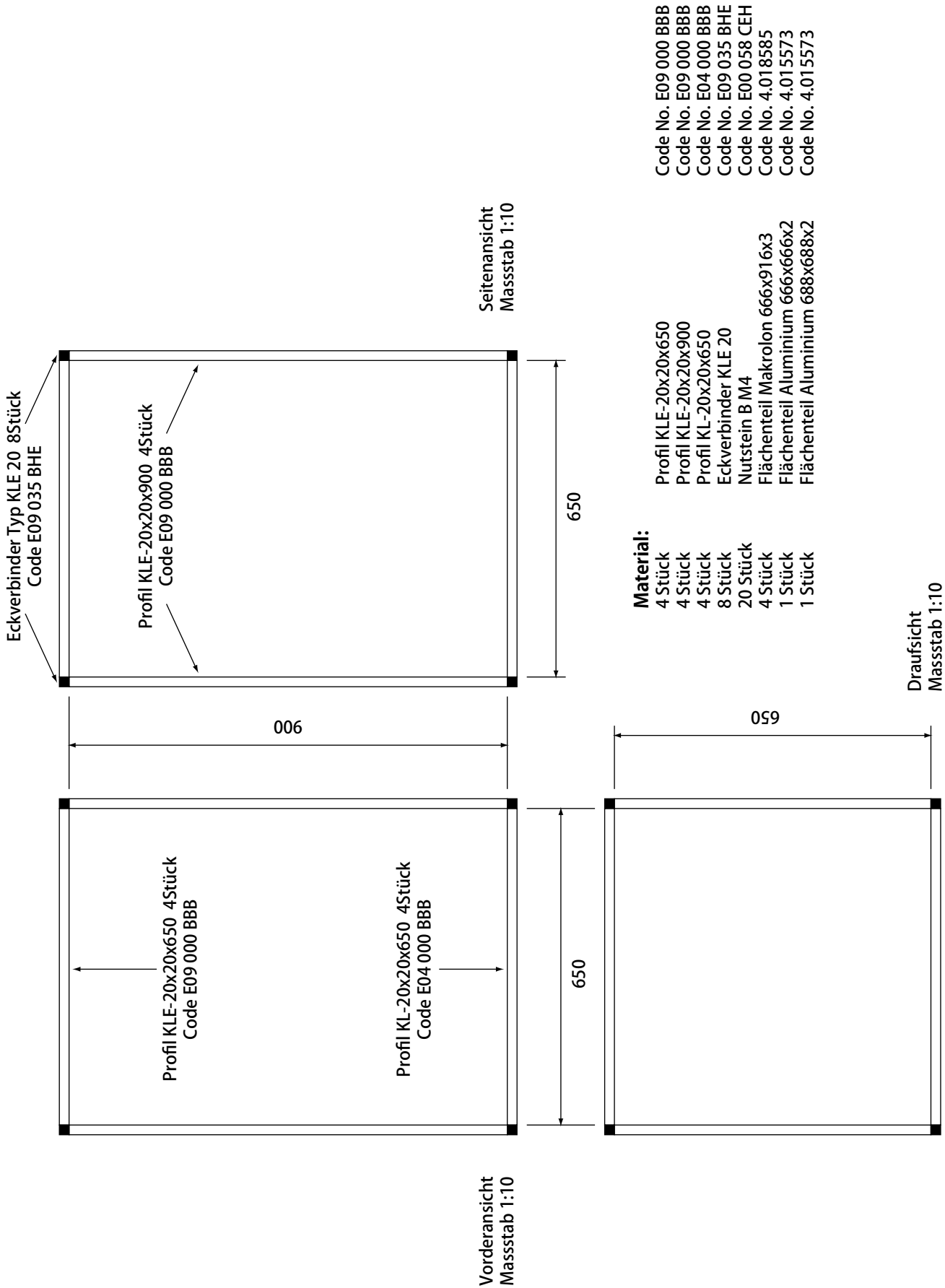
$$\beta(r, D_p, \text{Temp}, \rho_p, Q, p) := \left(\frac{12 \cdot k_e(Q) \cdot D(\text{Temp}, D_p, p)}{\pi^2 \cdot r \cdot V_{\text{ts}}(\text{Temp}, D_p, \rho_p, p)} \right) \int_0^{\infty} \frac{\pi \cdot V_{\text{ts}}(\text{Temp}, D_p, \rho_p, p)}{2 \cdot (k_e(Q) \cdot D(\text{Temp}, D_p, p))^{0.5}} \cdot \frac{x}{e^x - 1} dx + \frac{3 \cdot V_{\text{ts}}(\text{Temp}, D_p, \rho_p, p)}{4 \cdot r} \quad \text{B\&W 8-79}$$

$$\eta(r, D_p, \text{Temp}, \rho_p, Q, p, t) := \exp\left(-\int_0^t \beta(r, D_p, \text{Temp}, \rho_p, Q, p) dw\right) \quad \text{B\&W 8-78}$$

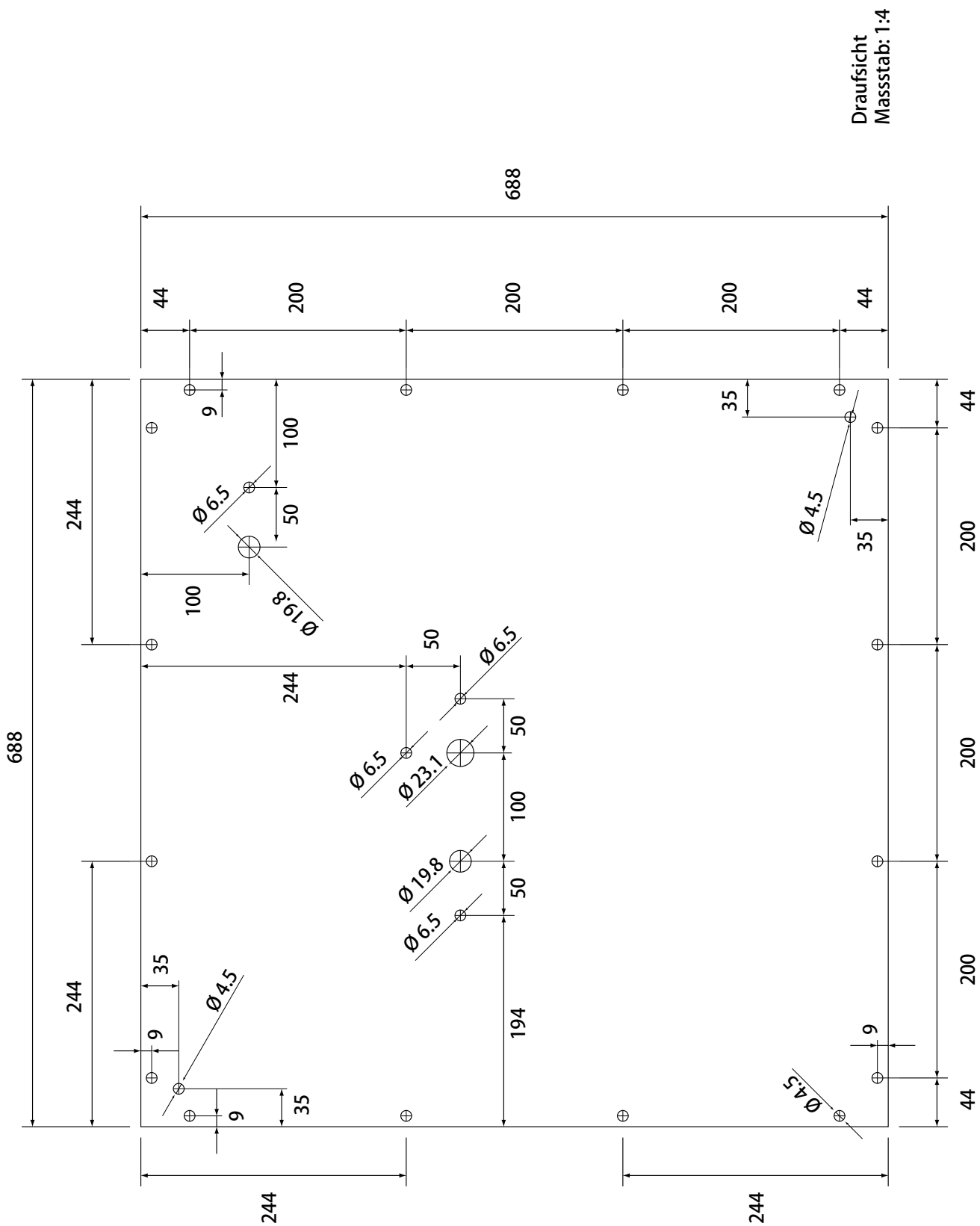
$$\eta(0.3, 0.1, 293, 1000, 1.7 \cdot 10^{-5}, p_0, 0) \cdot 100 \Rightarrow 100$$

$$\text{range} := 0.001, 0.002 \dots 1$$

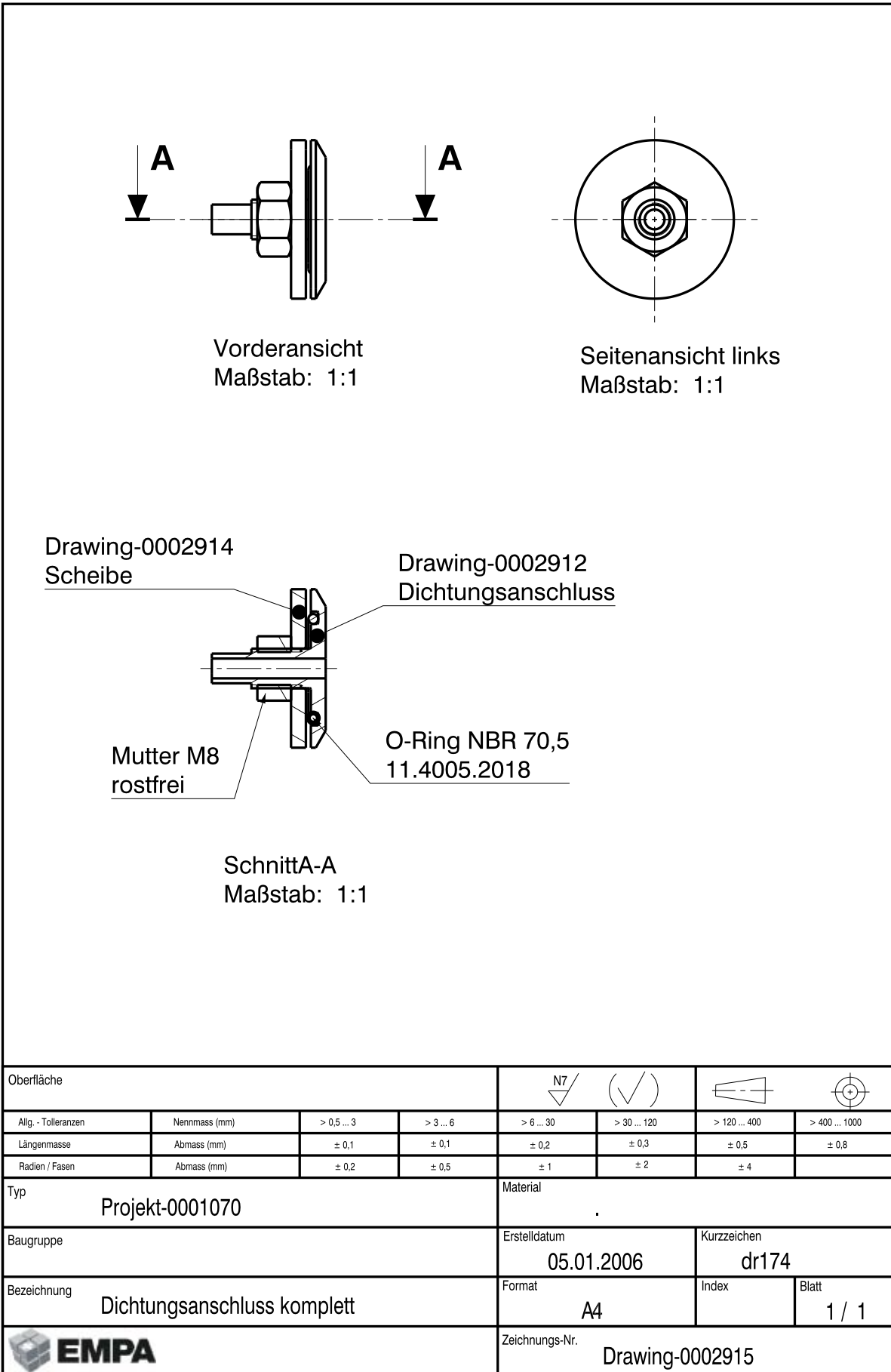
A.4.2 Schematic of the bag sampler's frame



A.4.3 Schematic of the bag sampler's top cover



A.4.4 Schematic of the multi purpose inlet



Single Particle Analysis of Welding Fumes - An Investigation of a Working Environment

Ronny Lorenzo^{a,c}, Patrick Steidle^b, Patrick Thal^b & Bernard Grobéty^c

^aEmpa, Materials Science & Technology, CH-8600 Dübendorf, Switzerland
^bSuva, Department for Preventive Measures, CH-6002 Lucerne, Switzerland

^cUniversity of Fribourg, Ch. de Musée 6, CH-1700 Fribourg, Switzerland
 Contact: ronny.lorenzo@empa.ch

Introduction

Welding produces vast amounts of particulates in the size range of ~10nm up to a few µm and above. With increasing awareness of possible adverse health effects of nanoparticles (diameter < 100nm, PM_{0.1}) more thorough investigations of working environments are conducted. In this study we present a combination of on- and off-line measurements for an integral assessment of the particulate exposure caused by welding activities.

At the engineering business under investigation fully and semi automated micro-casting techniques are applied. The principle process is gas metal arc welding (GMAW) with 97.5% Ar and 2.5% CO₂ on Steel #1.4313 (Table 1) with steel welding rods (material # 1.4351; Table 1).

Material Nr.	Base Material	Welding Rod
	1.4313	1.4351
Si	< 0.70%	0.25% - 0.55%
Mn	< 1.50%	0.55% - 0.95%
Cr	12.0 - 14.0%	12.7% - 14.8%
Mo	0.30% - 0.70%	0.35% - 0.75%
Ni	3.50% - 4.50%	3.10% - 4.90%

Table 1:

Principle alloys present in the steel types used for GMAW. In addition to the elements listed traces (<0.1%) of C, P, S and N (only base material) are tolerated. The diameter of the welding rod is 1.2mm for both techniques. Base materials are cleaned and heated to ~110°C prior to welding.

Instrumentation

On-line measurements of particle size distributions and number concentrations were performed with a fast mobility particle sizer (FMPS) TSI model 3091 and a scanning mobility particle sizer (SMPS) TSI model 3034. The time resolution of the SMPS is 3 minutes. As the variations in the particle number concentrations occurred on a smaller time scale, the air used for the SMPS measurements was drawn from a sampling bag (110 l) which homogenized the air masses. Additionally, particle number concentration was measured with high time resolution (1s) with an electrical diffusion battery (EDB).

Samples for off-line single particle analysis in a transmission electron microscope (TEM; Philips CM30, LaB₆ source) were collected directly onto microscope grids with an electrostatic and a thermophoretic sampling device.

On-line Measurements

Bag buffered SMPS measurements of fresh welding fumes (2m distance to the source) revealed particle modes at 20nm, 40nm and 160nm (Figure 1). FMPS measurements with high time resolution (1s) from the same inlet location showed that the mode at 20nm can only be observed inside a plume (Figure 2). The comparison with particle size distributions

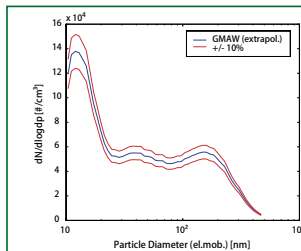


Figure 1:

Particle size distribution corrected for particle losses as calculated from a series of SMPS scans performed on an air sample delivered by a 110 litre bag sampling system. The inlet of the bag system was placed ~2m above the arc of a fully automated work place, directly in the plume of fresh welding fumes. The size distribution shown represents a well mixed body of air sampled over a time period of 20 min.

at background sites (>10m away from source) confirmed this interpretation.

The evolution of the particle number concentration measured at 4m distance to the welding arc (Figure 3) mirrors the passing of a fresh plume with distinct events of higher concentrations.

Even after longer periods without welding activity (2h, premises are well ventilated), the particle number concentration did not drop below 6.5·10⁴ part./cm³ and the modes at 40nm and 160nm were still clearly distinguishable.

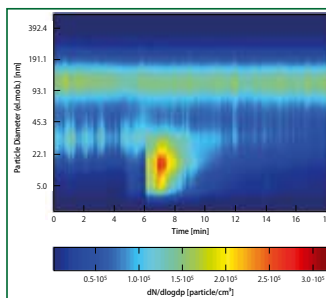


Figure 2:

FMPS scan series with 1s time resolution. The aerosol inlet was placed ~2m away from the arc of a semi-automated work place. Measurements performed with this inlet position represent the normal exposition of the supervising employee to welding fumes produced at this work place. The mode at ~160nm corresponds to the background concentration in the construction hall and consists of larger chains of primary particles. The short burst of particles with diameter ~18nm is due to a plume of newly produced particles passing the inlet.

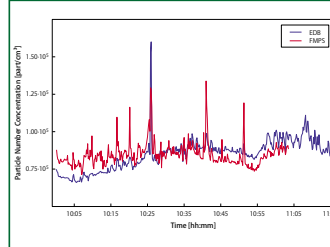


Figure 3:

Particle number concentration measured by an electrical diffusion battery and a fast mobility particle sizer. The inlets of the two measuring devices were placed ~4m from the arc of a fully automated work place. The large variations in particle numbers are due to changing air currents transporting plumes of fresh welding fumes directly to the inlets. The average PM_{0.5} number concentration is 8·10⁴ particles/cm³, which corresponds to a heavily frequented highway.

TEM Analysis

Single particle analysis on the TEM samples allowed a clear distinction of three types of primary particles (Figure 4) on the basis of their physical appearance. Slight variations in the elemental composition of the agglomerates are observed (Figure 5). Whether these

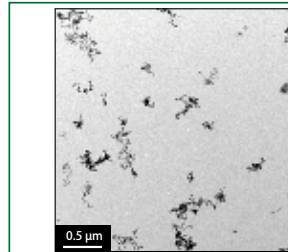


Figure 4:

Low magnification TEM image of a sample taken with the electrostatic sampling device (4m distance to the source) illustrating the different particle shapes observed.

Most of the agglomerates are composed of three types of primary particles:

- <15nm in diameter, spherical in shape & monocrystalline;
- 15nm - 60nm in diameter, angled & monocrystalline;
- >60nm in diameter, spherical in shape & crystalline.

variations can be traced to classes of primary particles or not is still under investigation. Since all of the primary particles appear to be crystalline (Figure 6) additional information on the elemental composition of the particles can be gained by examining their crystalline structure.

While the modes at 40nm and 160nm could be observed on the TEM samples, hardly any particles with diameters below 20nm were found.

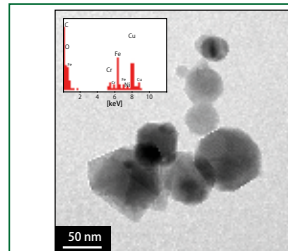


Figure 5:

TEM micrograph of a typical particle of intermediate size (mode at 160nm). The inset shows the result of the energy dispersive x-ray analysis. The C and Cu peaks are produced by the TEM grid and the grid holder and not by the particle. Comparing EDX spectra of various particles, the Fe/Cr peak ratio varies from 2/1 to 4/1 and the Cr/Ni peak ratio stays around 3/1.

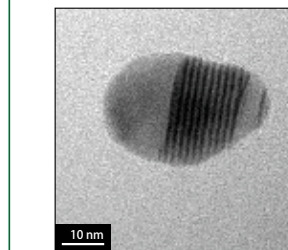


Figure 6:

High magnification image of an individual (twinned) particle. Such particles together with small agglomerates of primary particles with diameter below 15nm contribute most to the mode at 40nm (see Fig. 1 & 2).

Conclusions

With the combination of on-line measurements and off-line analysis methods suggested in this study, a complete data set on exposure to particulate matter for risk assessments of working environments can be compiled.

The additional information gained by electron microscopical single particle analysis renders a more thorough picture of the nature and availability of possibly harmful substances.

Acknowledgment

We thank Oliver Bischof and Jürgen Reith from TSI for joining us on our measurement campaign with a FMPS and giving us the data for further analysis.



Detailed Single Particle Analysis of Ultrafine Welding Fume Particles

Ronny Lorenzo^{a,c}, Patrick Steinkle^b, Patrick Thali^b & Bernard Grobety^c

^aEmpa, Materials Science & Technology, CH-8600 Dübendorf, Switzerland
^bSwiss National Accident Insurance Fund, CH-6002 Lucerne, Switzerland

^cUniversity of Fribourg, Ch. de Musée 6, CH-1700 Fribourg, Switzerland
 Contact: ronny.lorenzo@empa.ch

Introduction

Welding produces vast amounts of particulates in the size range of ~10nm up to a few µm and above. With increasing awareness of possible adverse health effects of nanoparticles (diameter < 100nm, PM0.1) more thorough investigations of working environments are conducted. In this study we present a combination of on- and off-line measurements for an integral assessment of the particulate exposure caused by welding activities.

At the engineering business under investigation fully and semi automated micro-casting techniques are applied. The principle process is gas metal arc welding (GMAW) with 97.5% Ar and 2.5% CO₂ on Steel #1.4313 (Table 1) with steel welding rods (material # 1.4351; Table 1).

Material Nr.	Base Material	Welding Rod
	1.4313	1.4351
<i>Si</i>	< 0.70%	0.25% - 0.55%
<i>Mn</i>	< 1.50%	0.55% - 0.95%
<i>Cr</i>	12.0 - 14.0%	12.7% - 14.8%
<i>Mo</i>	0.30% - 0.70%	0.35% - 0.75%
<i>Ni</i>	3.50% - 4.50%	3.10% - 4.90%

Table 1: Principle alloys present in the steel types used for GMAW. In addition to the elements listed traces (<0.1%) of C, P, S and N (only base material) are tolerated. The diameter of the welding rod is 1.2mm for both techniques. Base materials are cleaned and heated to ~110°C prior to welding.

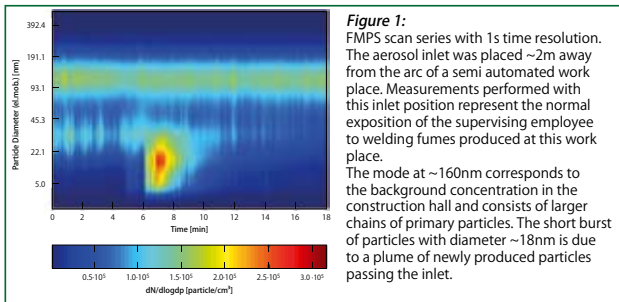
Instrumentation

On-line measurements of particle size distributions and number concentrations were performed with a fast mobility particle sizer (FMPS) TSI model 3091 and a scanning mobility particle sizer (SMPS) TSI model 3034. The time resolution of the SMPS is 3 minutes. As the variations in the particle number concentrations occurred on a smaller time scale, the air used for the SMPS measurements was drawn from a sampling bag (110 l) which homogenized the air masses. Additionally, particle number concentration was measured with high time resolution (1s) with a diffusion size classifier (DiSC; Fierz & Burtscher 2005).

Samples for off-line single particle analysis in a transmission electron microscope (TEM; Philips CM30, LaB₆ source) were collected directly onto microscope grids with an electrostatic and a thermophoretic sampling device.

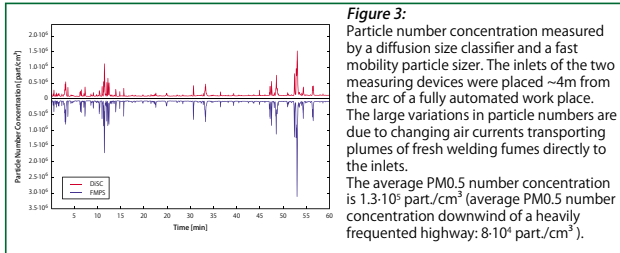
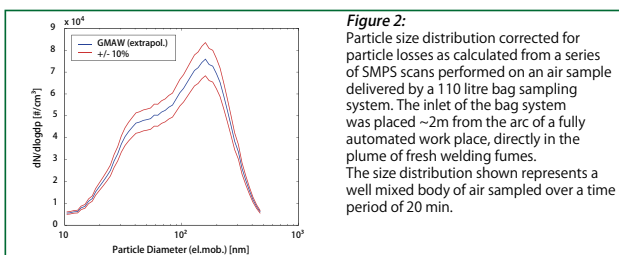
On-line Measurements

FMPS measurements with high time resolution (1s) of fresh welding fumes (2m distance to the source) revealed particle modes at 20nm, 40nm and 160nm (Figure 1). Bag buffered SMPS measurements from a similar inlet location showed that the mode at 20nm can only be observed inside a plume (Figure 2). The comparison with particle size distributions at background sites (>10m away from source) confirmed this interpretation.



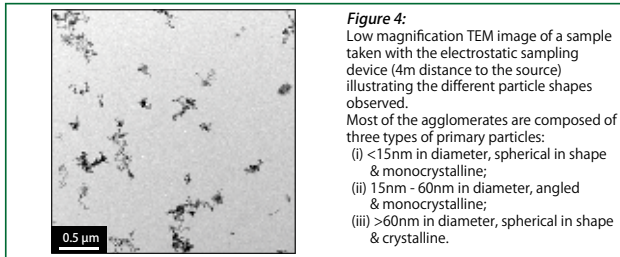
The evolution of the particle number concentration measured at 4m distance to the welding arc (Figure 3) mirrors the passing of a fresh plume with distinct events of higher concentrations.

Even after longer periods without welding activity (2h, premises are well ventilated), the particle number concentration did not drop below 6.5·10⁴ part./cm³ and the modes at 40nm and 160nm were still clearly distinguishable.



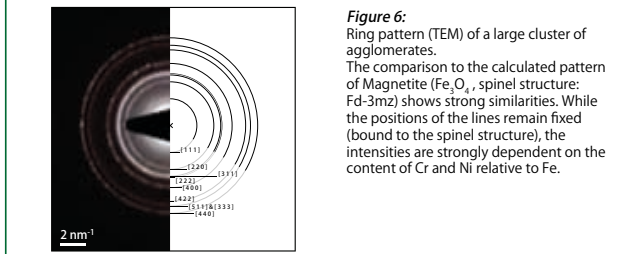
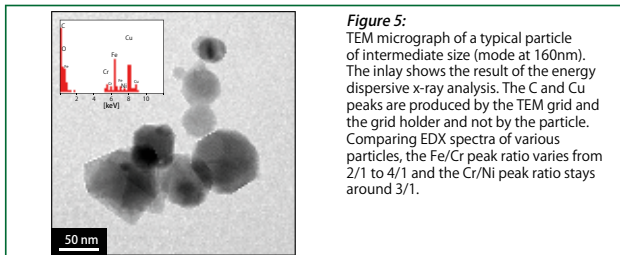
TEM Analysis

Single particle analysis on the TEM samples allowed a clear distinction of three types of primary particles (Figure 4) on the basis of their physical appearance. Slight variations in the elemental composition of the agglomerates are observed (Figure 5). Whether these variations can be traced to classes of primary particles or not is still under investigation.



Since all of the primary particles appear to be crystalline additional information on the elemental composition of the particles can be gained by examining their crystalline structure (Figure 6).

While the modes at 40nm and 160nm could be observed on the TEM samples, hardly any particles with diameters below 20nm were found.



Conclusions

With the combination of on-line measurements and off-line analysis methods suggested in this study, a complete data set on exposure to particulate matter for risk assessments of working environments can be compiled.

The additional information gained by electron microscopical single particle analysis renders a more thorough picture of the nature and availability of possibly harmful substances.

Reference

M. Fierz and H. Burtscher (2005): *A portable diffusion size classifier*. Abstracts of the European Aerosol Conference, Ed. W. Maenhaut, University of Gent, p.423.

Appendix

- Acknowledgments
- Curriculum Vitae
- Publication List

*«Gallopig about the cosmos is a game for the young, doctor»
Admiral James Tiberius Kirk, Star Trek II*

Acknowledgments

First of all, I'd like to express my gratitude to my thesis supervisor Bernard Grobéty and co-supervisor Ralf Kägi for posting this project, guiding me in the beginning and supporting me, whenever necessary, on the rest of the way. Ralf, working with you was always fun and instructive. Somehow our laboratory felt like an exclave of an university rather than an office of a materials testing facility... Bernard, your knowledge on electron microscopy is amazing and I really appreciated your TEM tutorials at the Empa.

My perfect appreciation goes to the board members of the SILAG who believed in this project and went out of their way to fund it.

Heinz Burtscher and Martin Fierz, thank you for helping me out while building and calibrating the TPS. Martin, you're an extraordinary patient person. We broke the ESS about a million times and you just shrugged and fixed that thing once more (or had it fixed...).

I thank Prof. Dr. E. Flückiger for accepting my proposal for a project on the High Alpine Research Station on the Jungfrauoch. Unfortunately, the project never really got much further than the sampling stage, sorry for that.

Most definitively my gratitude goes to Patrick Steinle of the SUVA for opening many doors and inviting me to measurement campaigns; giving me a chance to test our equipment and strategies at working environments.

I thank Brigitte and Robert for furnishing me with a perfectly equipped work place and being genuinely interested in my work. It's a pity the single particle group ceases to exist at the Empa. Robert, thank you for the support you and your group have given me, especially during the SBB project.

A big «thank you» goes to my office mates Martine and Valentin for contributing to the diverting and yet professional atmosphere prevailing in our laboratory. An equally important part in making this three year intermezzo at the Empa a canny one, had the members of the modelling group: Doris, Sandy and Daniel. Thank you for always having enough time for an additional coffee break...

The un-bureaucratic way of Lukas and his group to help out with tools and hardware, and Christoph and group to grant access to their facilities, made life a lot easier. Thank you for that!

And of course, I thank all members of the Laboratory for Air Pollution and Environmental Technique for the relaxed atmosphere and the many chats during coffee breaks and lunches and ...

To my friends: Thank you for not forgetting me although I've been living in exile in «Berne East» and «Lucerne North», respectively, for the last three years...

My sincerest gratitude goes to the Caldwells for welcoming me back as a family member on my stopovers after the conferences in the US, and on every other chance I get to drop by.

Und schliesslich möchte ich meiner Familie gegenüber meine zutiefst empfundene Dankbarkeit zum Ausdruck bringen, dass sie mir ermöglicht haben einen akademischen Weg einzuschlagen.

To conclude, I'd like to thank Adobe for releasing outstanding software in spite of Microsoft's incompetence in building operating systems.

And finally, I express my gratitude to Triumph motorcycles for sticking to the three.

Curriculum Vitae

Ronny Lorenzo

Mobile: +41 (79) 603 06 20
E-Mail: lorenzo@apodemia.ch

Nationality : Swiss, Spaniard
Date of Birth : 15th March 1976



Education

2004 - 2007 University of Fribourg & Empa, Laboratory for Air Pollution

Ph.D. in Natural Sciences

«Sources and Characteristics of Fine and Ultrafine Particles in Ambient Air»

1997 - 2003 Universität Bern, Abteilung für Klima- und Umweltphysik

Master of Science in Physics

Work Experience

2007 - Armasuisse

Scientific Project Leader in the Department for Ballistics and Detonics

2004 - 2007 Empa, Laboratory for Air Pollution

Scientific Collaborator in the 'immissions group'
Specialist for representative sampling for single particle analysis and analysis of fine and ultrafine particles by means of electron microscopy.

2001 - 2003 Physics Institut, University of Berne

Teacher for courses in experimental physics for students of veterinary medicine.

2001 - 2003 Department for Climate- & Environmental Physics, University of Berne

Scientific Collaborator in the group for groundwater research
Collaboration on field campaigns to the Nubian Desert (Egypt) and the Bohemian Forests (Czech Republic).

Leadership

2000 Swiss Army Officers School

Present Rank : First Lieutenant of the Infantry

Present Function : Specialist (batallion staff) for atomic, biological and chemical warfare.

Language Skills

Swiss German (native language)
German (fluent)
English (fluent)
French (basic knowledge)

Computer Skills

Microsoft: Windows XP, MS Office XP
Adobe: Illustrator CS 2, Acrobat 7.0 Professional, Photoshop CS 2, InDesign CS 2
Others: Matlab, EndNote, Digital Micrograph, jEMS
advanced knowledge in html- & php- programming

List of Publications**Articles**

- Lorenzo, R., *et al.* (2006). Particle emissions of a railway line determined by detailed single particle analysis. *Atmos. Environ.* 40:7831-7841.
- Lorenzo, R., *et al.* (2007). A thermophoretic precipitator for the representative collection of atmospheric ultrafine particles for microscopic analysis. *Aeosol Science and Technology*. accepted.
- Lorenzo, R., *et al.* (2007). *Extending the assessment procedures for exposure situations at working environments to ultrafine particles*. *J. Occ. Env. Hygiene*. submitted.
- Sturchio, N. C., *et al.* (2004). One million year old groundwater in the Sahara revealed by krypton-81 and chlorine-36. *Geophys. Res. Lett.* 31.
- Du, X., *et al.* (2003). A new method of measuring Kr-81 and Kr-85 abundances in environmental samples. *Geophys. Res. Lett.* 30.
- Sturchio, N. C., *et al.* (2002). Residence time of Nubian aquifer water, Western Desert, Egypt. *Geochim. Cosmochim. Acta.* 66:A748-A748.

Presentations

- Lorenzo, R. (2006). Measurement and characterisation of nanoparticles at working environments. Invited speaker at a meeting of occupational safety and health specialists of the Swiss Federal Accident Insurance Fund (SUVA), Lausanne, CH.
- Lorenzo, R. (2007). Detailed single particle analysis of ultrafine particles. Invited speaker at a conference on the environmental impact of waste incineration plants, Bozen, I.

Posters

- Lorenzo, R., *et al.* (2006). Detailed single particle analysis of ultrafine welding fume particles. Poster presented at the *International Aerosol Conference*, St. Paul MN, USA.
- Lorenzo, R., *et al.* (2006). Single particle analysis of welding fumes - an investigation of a working environment. Poster presented at the *ETH conference on combustion generated particles*, Zurich, CH.
- Lorenzo, R., *et al.* (2005). A new thermophoretic sampling device for collection of ultrafine particles. Poster presented at the *AAAR 2005 Annual Conference*, Austin TX, USA.
- Lorenzo, R., *et al.* (2005). Particulate emissions of a railway line determined by detailed single particle analysis. Poster presented at the *European Aerosol Conference*, Gent, B.

«Aye. And if my grandmother had wheels she'd be a wagon...»

Scotty, Star Trek III